DE GRUYTER STEM

*Karen K. Gleason, Meysam Heydari Gharahcheshmeh*

# CONJUGATED POLYMERS AT NANOSCALE

## ENGINEERING ORIENTATION, NANOSTRUCTURE, AND PROPERTIES

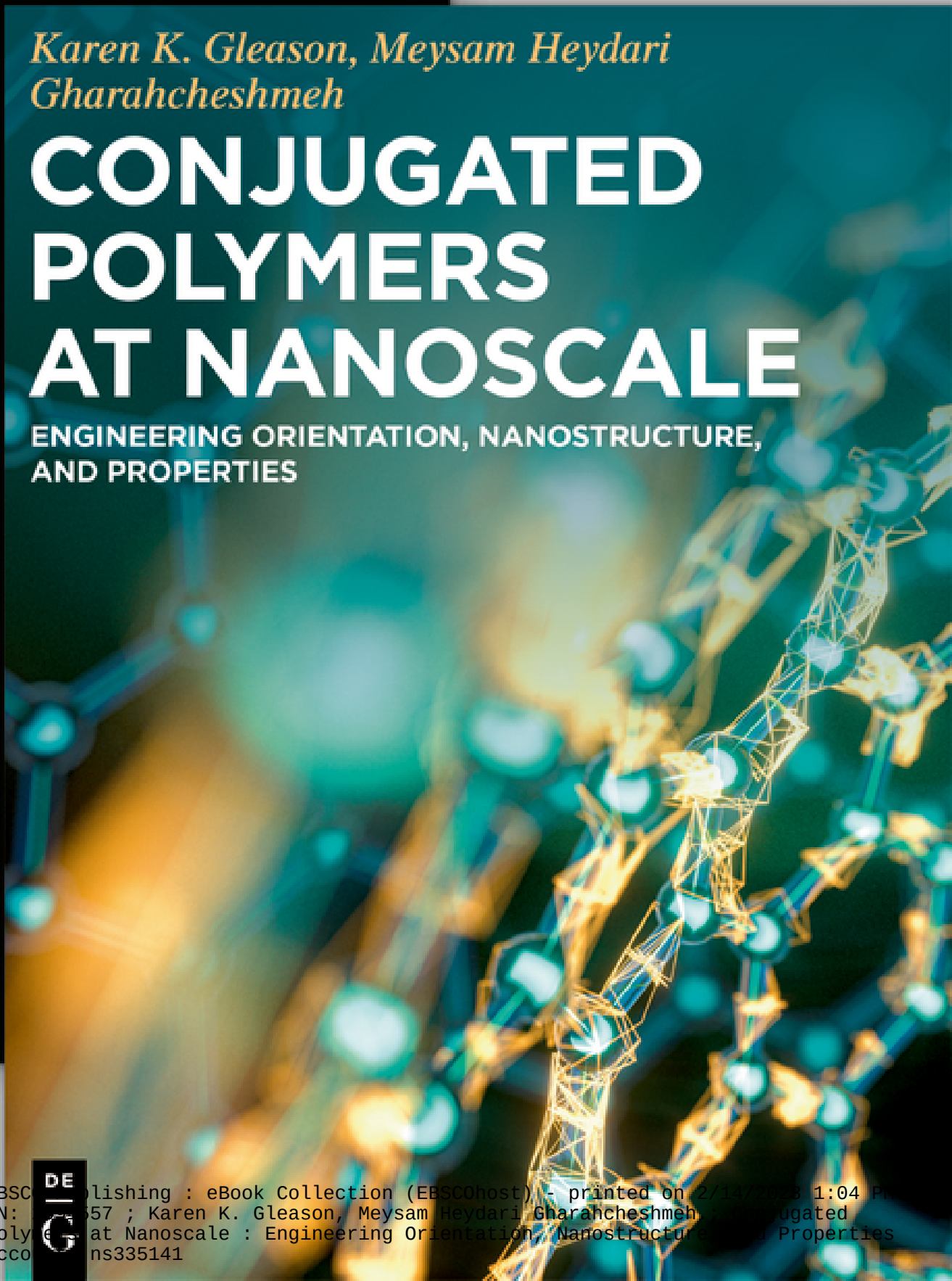

Karen K. Gleason, Meysam Heydari Gharahcheshmeh

**Conjugated Polymers at Nanoscale**

## Also of Interest

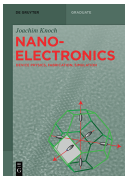


*Nanoelectronics*.
*Device Physics, Fabrication, Simulation*
Joachim Knoch, 2021
ISBN 978-3-11-057421-0, e-ISBN 978-3-11-057550-7

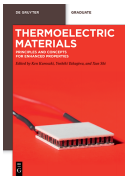


*Thermoelectric Materials*.
*Principles and Concepts for Enhanced Properties*
Ken Kurosaki, Yoshiki Takagiwa and Xun Shi (Eds.), 2020
ISBN 978-3-11-059648-9, e-ISBN 978-3-11-059652-6

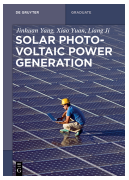


*Solar Photovoltaic Power Generation*
Jinhuan Yang, Xiao Yuan and Liang Ji, 2020
Together with: Publishing House of Electronics Industry
ISBN 978-3-11-053138-1, e-ISBN 978-3-11-052483-3

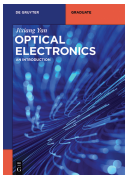


*Optical Electronics*.
*An Introduction*
Jixiang Yan, 2019
Together with: Tsinghua University Press
ISBN 978-3-11-050049-3, e-ISBN 978-3-11-050060-8


*Biosensors*.
*Fundamentals and Applications*
Chandra Mouli Pandey and Bansi Dhar Malhotra, 2019
ISBN 978-3-11-063780-9, e-ISBN 978-3-11-064108-0

Karen K. Gleason,
Meysam Heydari Gharahcheshmeh

# Conjugated Polymers at Nanoscale

Engineering Orientation, Nanostructure, and Properties

DE GRUYTER

**Authors**
Prof. Karen K. Gleason
Department of Chemical Engineering
Massachusetts Institute of Technology
NE47-507
77 Massachusetts Avenue
Cambridge, MA 02139
United States of America
kkg@mit.edu

Dr. Meysam Heydari Gharahcheshmeh
Department of Chemical Engineering
Massachusetts Institute of Technology
NE47-507
77 Massachusetts Avenue
Cambridge, MA 02139
United States of America
mheydari@mit.edu

ISBN 978-1-5015-2460-8
e-ISBN (PDF) 978-1-5015-2461-5
e-ISBN (EPUB) 978-1-5015-1617-7

**Library of Congress Control Number: 2021936865**

**Bibliographic information published by the Deutsche Nationalbibliothek**
The Deutsche Nationalbibliothek lists this publication in the Deutsche Nationalbibliografie; detailed bibliographic data are available on the Internet at http://dnb.dnb.de.


Cover image: Jian Fan/iStock/Getty Images Plus
Typesetting: Integra Software Services Pvt. Ltd.
Printing and binding: CPI books GmbH, Leck

www.degruyter.com

# Contents

# Symbols for physical constants and properties

**Tab. 1:** Symbols for physical constants and properties frequently used in this book.

| Quantity | Symbol | Value or typical units |
|---|---|---|
| Permittivity of free space | $\varepsilon_0$ | $8.854 \times 10^{-12}$ F/m |
| Dielectric constant (relative permittivity) | $\varepsilon_r$ | Dimensionless |
| Unit charge | $e$ | $1.602 \times 10^{-19}$ coulombs |
| Energy of an electronic state | $E$ | eV |
| Fermi energy | $E_F$ | eV |
| Band gap energy | $E_g$ | eV |
| Urbach energy | $E_U$ | meV |
| Density of states (DOS) | $g(E)$ | $cm^{-3}$ |
| Reduced Planck constant | $\hbar$ | $6.582 \times 10^{-16}$ eV·s |
| Boltzmann constant | $k_B$ | $8.617 \times 10^{-5}$ eV/K |
| Mass of a free electron | $m_e$ | $9.109 \times 10^{-31}$ kg |
| Effective mass of the charge carrier | $m^*$ | kg |
| Charge carrier mobility | $\mu$ | $m^2/(V \cdot s)$ |
| Charge carrier concentration | $n_c$ | $cm^{-3}$ |
| Sheet resistance | $R_s$ | Ω/sq |
| Electrical conductivity | $\sigma$ | S/cm |
| Absolute temperature | $T$ | Kelvin |

https://doi.org/10.1515/9781501524615-203

# 1 Introduction

This book focuses on the fundamental interconnection between the nanostructure and the properties of conjugated polymers. The linear and rigid polymeric backbones that favor extended conjugation are prone to crystallization. In many cases, the conjugated polymers are semicrystalline. Their morphology results from nanoscale crystallites which are surrounded by an amorphous phase [1, 2]. The nanocrystallites can adopt a preferential orientation, display a mixed texture, or have a completely random orientation distribution (Fig. 1.1).

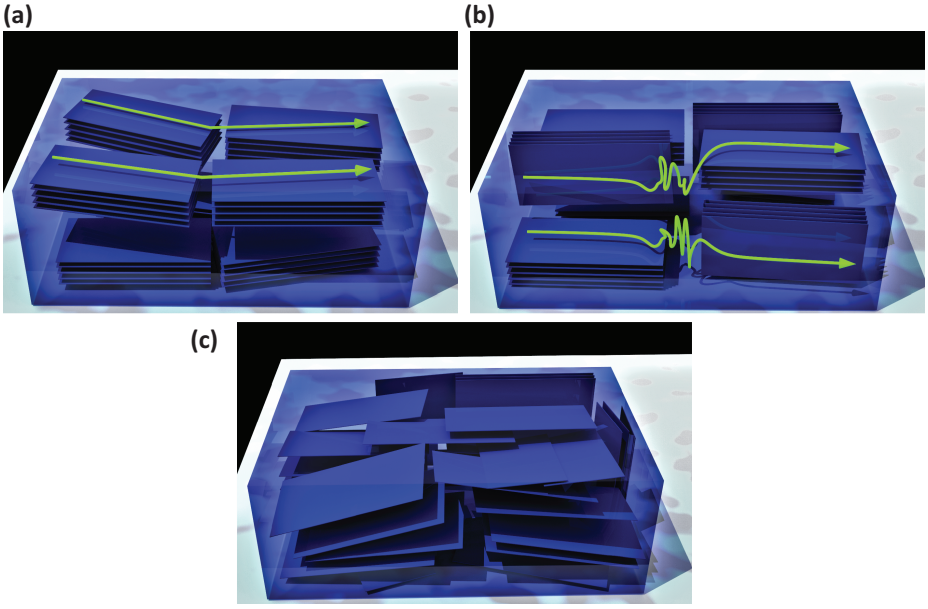


**Fig. 1.1:** Schematics of three possible nanocrystallite orientation distributions in semicrystalline conjugated polymers: (a) preferential face-on texture, (b) mixed face-on and edge-on texture, and (c) random orientation. The green lines with arrows suggest possible conformations for individual macromolecular chains.

In a semicrystalline conjugated polymer, individual chains are subjected to vastly different local environments. A chain can be confined entirely within a single nanocrystallite or segregate completely in the amorphous domain. Alternatively, part of the chain can reside in a nanocrystallite, while the remainder of the chain is part of the surrounding amorphous region. Additional possibilities arise for higher molecular weight chains. Of particular interest are tie chains, which fully span amorphous domains to interconnect two or more nanocrystallites. The electronic transport along the tie chains will be influenced by the relative orientation of the nanocrystals being connected.

https://doi.org/10.1515/9781501524615-001

Engineering order and orientation is essential for optimizing electronic transport in conjugated polymers. Undoped polymers can be useful as semiconductors. Through careful control over the nanoscale morphology and doping, metallic-like conduction can result. In addition, the nanoscale structure and texture of conjugated polymers underlie their optical, ionic, and thermal, transport properties.

Lightweight and mechanically compliant conjugated polymers have great potential for next generation flexible, mobile, and wearable devices. Semiconducting polymers are of interest for fabricating organic transistors, while semimetallic polymers are of interest for thermoelectric (Chapter 6) and spintronic (Chapter 7) applications [3]. Combining electrical conductivity with optical transparency is essential for forming transparent electrodes for optoelectronic devices [4–7]. Transparent conductors in displays, touchscreens, and light-emitting diodes allow light to be emitted, while in solar cells, transparent conductors allow for light to pass through for subsequent absorption in the active layer. Electrochemical energy storage devices, such as batteries [8–11] and supercapacitors [12–15], can benefit from pseudocapacitive behavior of conjugated polymers, which requires both electronic and ionic conductivity. Combining electrical conduction with organic functional groups is useful in chemical and biochemical sensors [1, 4, 16], as well as in biomedical devices [1]. Future applications of conjugated polymers may result in superconductivity, magneto-optics, and artificial muscles [17].

Combining the formal approaches of organic chemistry and solid-state physics is a powerful means to understand the charge transport mechanisms in semicrystalline conjugated polymers. The chemical perspective starts from atomic orbitals, which overlap to form extended molecular orbitals that delocalize electrons over multiple atoms. The solid-state physics approach starts from fully delocalized wavefunctions, known as Bloch waves, which give rise to electronic band structure. Upon the addition of disorder and defects, the extent of the wave function is reduced and can become partially localized over a subset of atoms.

This introductory chapter summarizes the chemistry- and physics-based descriptions of electronic conduction along a single isolated conjugated polymer chain. Subsequent chapters will focus on how the nanoscale morphology and orientation that develop when multiple conjugated polymer chains interact in the solid state impact electrical conduction as well as the transport of photons, phonons, and ions.

## 1.1 Chemical bonding and electronic states

The groundbreaking discovery of polymers that conduct electricity was recognized with Nobel Prize in Chemistry in 2000 to Hideki Shirakawa, Alan Heeger, and Alan MacDiarmid. Prior to this discovery, polymers were considered to be electrical insulators, having a band gap in excess of 5 eV between the valence and conduction

bands. Such dielectric polymers have only sigma (σ) chemical bonds, representing molecular orbitals which are spatially localized between pairs of atoms.

In addition to σ bonds, conjugated polymers possess π bonds formed from the overlap of p-orbitals on adjacent atoms (Fig. 1.2a). Each atom contributes one electron to the π bond. The π bond formation requires that the p-orbitals are orthogonal to the *xy* plane of the σ bond. Figure 1.2b schematically shows the two molecular orbitals formed from the overlap of two $p_z$-orbitals. The lower energy molecular orbital is the π bonding state, formed by the constructive addition of the two atomic orbitals. The other is a higher energy π* antibonding state resulting from the destructive (out-of-phase) addition of the two atomic orbitals. In the molecular ground state, both electrons fill the bonding state, leaving the antibonding state unoccupied.

A simple example of π bonding occurs between the two carbon atoms in a molecule of ethylene, which has the chemical structure, $H_2C{=}CH_2$. The carbon–carbon double bond consists of both σ and π bonding components (Fig. 1.2c). The σ bonding occurs between the $sp^2$ hybridized orbitals of the two carbon atoms. The $sp^2$ hybridization involves the s, $p_x$, and $p_y$ atomic orbitals. The three resulting hybrid orbitals lie in the *xy*-plane and form σ bonds with the other carbon atom and with two hydrogen atoms. The $sp^2$ hybridization leaves the $p_z$-orbital available to participate in π bonding.

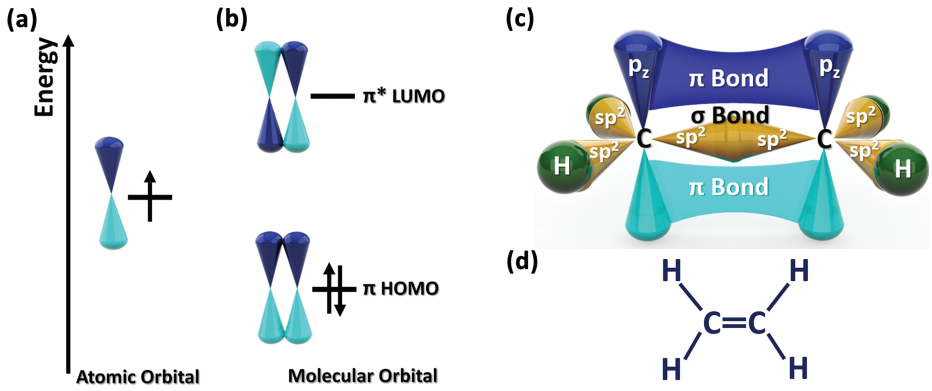


**Fig. 1.2:** Schematics of electronic orbitals and their associated ground state energy level diagrams: (a) an atomic p-orbital having two lobes of different phase, occupied by a single electron, and (b) the two molecular orbitals resulting from overlap p-orbitals on two adjacent atoms. The lower energy π bonding state is fully occupied by two electrons, while the higher energy π* antibonding state is unoccupied. For the molecule ethylene, (c) a schematic of the molecular orbitals, revealing both the σ and the π bonding characteristics of the carbon–carbon double bond, and (d) the formal chemical structure. Adapted with permission from Heydari Gharahcheshmeh and Gleason, Mater. Today Adv., 8, 10008 (2020) Copyright 2020, Elsevier.

**Conjugation** forms the spatially extended states responsible for electronic conduction. The term conjugation refers to the delocalized molecular orbitals formed from overlap

of $p_z$-orbitals from more than two atoms. For conjugation to develop, p-orbitals on adjacent atoms must be in the same orientation. The resulting states extend over all the participating atoms. Figure 1.3a schematically shows the four molecular orbitals for a chain of four conjugated atoms as occurs in the molecule 1,3-butadiene. The corresponding formal chemical structure $H_2C{=}CH{-}CH{=}CH_2$ contains alternating double and single bonds connecting the four $sp^2$ hybridized carbon atoms (Fig. 1.3b).

The molecular orbitals for conjugated macromolecules fall in two bands of allowed energies (Fig. 1.3c). In the ground state, the low π bonding energy band contains the highest occupied molecular orbital, denoted as the HOMO level, while the higher energy π* antibonding band contains the lowest unoccupied molecular orbital, denoted as the LUMO level. In the absence of defects and disorder, there are no electronic states having energies which fall in energy gap between the HOMO and LUMO levels. The alternating pattern of single and double bonds observed in 1,3-butadiene also occurs along the much longer backbone of the conjugated polymer poly(acetylene) (Fig. 1.3d). The alternation pattern can be drawn in two ways (Fig. 1.4a). These two

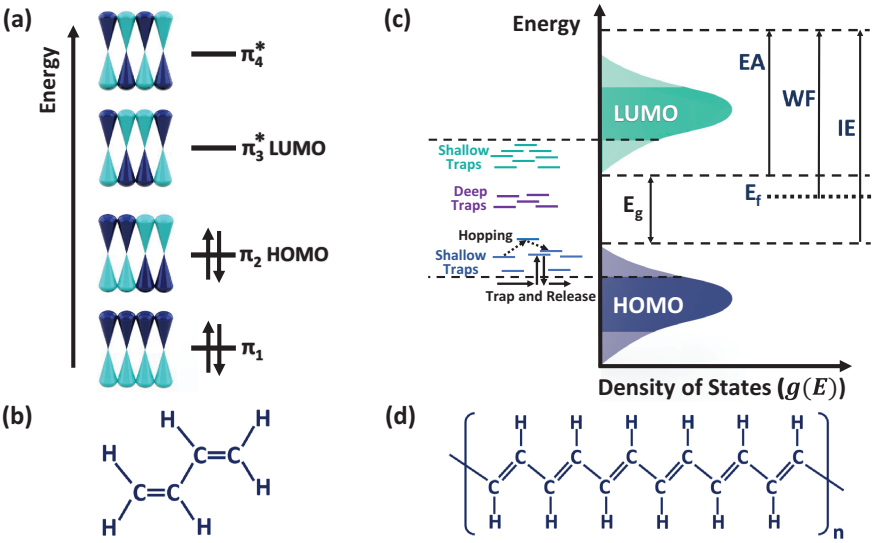


**Fig. 1.3:** (a) The four molecular orbitals resulting from the overlap of p-orbitals on four adjacent atoms and the associated ground state energy level diagram. The two π bonding states are of lower energy than the original atomic orbitals and are fully occupied. The two higher energy π* antibonding states are unoccupied. (b) The formal chemical structure of 1,3-butadiene, having alternating double and single carbon–carbon bonds. (c) For a large number of atoms participating in conjugation, the energy levels fall in two allowable bands. The gap separating the bands falls between the highest occupied molecular orbital (HOMO) and the lowest unoccupied molecular orbital (LUMO). The lighter shaded regions are localized states and the darker regions are extended states. (d) The formal chemical structure of poly(acetylene) having all carbon backbone with alternating double and single bonds. Adapted with permission from Heydari Gharahcheshmeh and Gleason, Mater. Today Adv., 8, 10008 (2020) Copyright 2020, Elsevier.

resonance structures are of identical energy, and thus the ground state of poly(acetylene) has a twofold degeneracy.

In addition to $sp^2$ hybridized carbon atoms, conjugated polymer chains can also contain heteroatoms with $p_z$-orbitals, such as nitrogen, sulfur, and selenium, as well as aromatic ring structures. As the chemical structure of the conjugated polymer becomes more complex, the energies of the resonance structures become different. An example, Fig. 1.4b shows the nondegenerate states for poly(thiophene). Displaying the double bonds in the form of an aromatic ring is termed a benzoid structure. Representing double bonds as positioned between the rings is called a quinoid structure.

If each backbone atom has a $p_z$-orbital oriented in the same orientation, the conjugation length can extend for the full length of the polymer chain. Any changes in regioregularity or rotational angles along the chain disrupt the π bond formation and shorten the conjugation length. In some cases, a single polymer chain can be divided into multiple segments of conjugation due to steric defects.

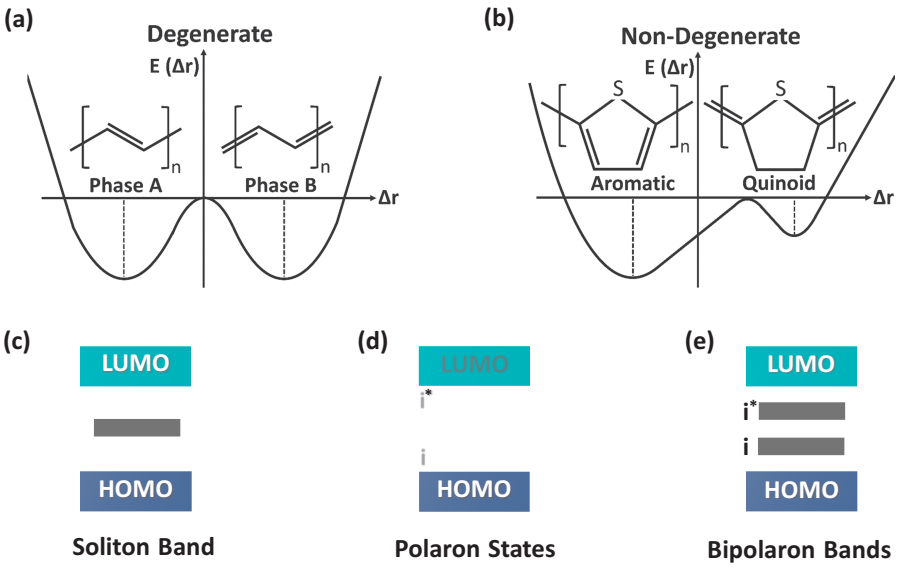


**Fig. 1.4:** Schematic diagrams of potential energy, $E(\Delta r)$, versus bond length alternation, $(\Delta r)$ for (a) poly(acetylene), having a twofold degenerate ground state, and (b) poly(thiophene), having a nondegenerate ground state. Schematic energy level diagrams for doped conjugated polymers showing (c) the soliton band produce in the degenerate case, and the (d) polaron states and (e) bipolaron bands resulting in the nondegenerate case. Adapted with permission from Heydari Gharahcheshmeh M and Gleason KK, Mater. Today Adv., 8, 10008 (2020) Copyright 2020, Elsevier.

## 1.2 Electronic band structure

The allowable HOMO and LUMO energy bands and HOMO-LUMO gap for molecular orbitals find analogy to the solid-state physics description of the electronic band structure in a perfectly periodic solid. From the physics perspective, the wavefunctions responsible for electronic conduction are fully delocalized over the crystal lattice. These extended states are called Bloch waves. The energies of the Bloch waves are restricted to discrete energy bands as a consequence of the regular positions of the atoms in a crystal.

Band structures are often visualized using a density of states (DOS) diagram (Fig. 1.3c). The vertical axis displays the energy of the states, $E$, while the horizontal axis gives the DOS at a given energy, $g(E)$. For a perfect single crystal semiconductor in its ground state, the lower energy valence band states are fully occupied and the higher energy conduction band states are unoccupied. The difference in energy between the bottom edge of the conduction band and the top edge of the valence band is the band gap energy ($E_g$). No electronic states exist in the corresponding band gap.

The DOS diagram allows visualization of the Fermi energy ($E_F$), the work function (WF), the ionization energy (IE), and electron affinity (EA). The values of these characteristic parameters of the electronic structure depend on the precise conditions of synthesis and post-processing, such as doping and annealing. The ability to tune electronic structure is often essential for optimizing device performance.

For a semiconductor, an electronic state at $E_F$ has a 50% probability of occupancy by an electron. The WF is the energy barrier for an electron to escape from a solid. The WF is equal to the energy difference the vacuum level, $E_{vac}$, and $E_F$. At $E_{vac}$, an electron within a few nanometers outside a solid surface has zero kinetic energy [18]. The IE is the minimum energy required to remove an electron from the valence band. Thus, the IE equals the difference between $E_{vac}$ and the energy level at the top edge of valence band. The EA is energy gained by adding an electron at the vacuum level to the bottom edge of the conduction band. The values of IE and EA represent important constraints when selecting dopants for semiconducting materials.

Defects, including intentionally added impurities that serve as dopants, alter the electronic states, changing both their energy and degree of delocalization. The altered states can be spatially localized near a defect and have energy levels located in the gap region. Such localized midgap states serve to trap electrons which could otherwise occupy more delocalized states. The presence of trap states reduces charge carrier mobility.

An isolated single chain of a conjugated polymer can be considered a one-dimensional (1D) conductor. All 1D metals can lower their energy by undergoing a Peierls distortion, which causes an alternation of short and long bond lengths along the chain [17]. This alternation reduces the energy as compared to a chain of identical bond lengths. The Peierls distortion also introduces an energy gap into the band

structure. Larger differences between the resulting bond lengths increase the size of the gap.

In a perfect crystal of infinite extent, the $g(E)$ has a sharp transition at a band edge. In a disordered solid having finite dimensions, the transition of $g(E)$ at a band edge is more gradual and is often approximated by a Gaussian distribution. For a band of states having a density of $N_0$ states per unit volume and a mean energy of $E_0$, a Gaussian band tail of width $\sigma_{DOS}$ is expressed as [2, 19]

$$g(E) = \frac{N_0}{\sigma_{DOS}\sqrt{2\pi}} \exp\left(\frac{-(E-E_0)^2}{2\sigma_{DOS}^2}\right) \tag{1.1}$$

Larger values of $\sigma_{DOS}$ correspond to increasing the width of the band tail in the DOS diagram and a higher degree of disorder in the solid. Examples of disorder include deviations of atomic positions from a periodic lattice (paracrystallinity) and the presence of interfaces and interfacial roughness. Thus, the value of $\sigma_{DOS}$ is sensitive to both materials processing conditions and nanostructure dimensions.

Measuring the temperature dependence of charge carrier mobility allows determination of the value of $\sigma_{DOS}$. Values of $\sigma_{DOS}$ are generally in the range of few $k_BT$ [2, 20], where $k_B$ is the Boltzmann constant and $T$ is the absolute temperature. Higher values of $\sigma_{DOS}$ are associated with reduced charge carrier mobility. As will be discussed in more detail in the chapter on optical properties, the Urbach energy, which is measured by optical absorption, can be attributed to the partially localized electronic states in the band tail.

## 1.3 Doping

Without doping, conjugated polymers are neutrally charged and generally have the modest levels of electrical conductivity associated with semiconductors. Doping ionizes the conjugated polymer and can significantly increase electrical conductivity and, in some cases, metallic values are achieved. The introduction of dopants also strongly influences the optical and thermoelectric properties of conjugated polymers [7, 21–23].

The dopant process for the conjugated polymer can be considered as a redox reaction between a neutral macromolecular chain and a redox agent [24]. Significant dopant concentrations are common and the fraction of all monomer units in the polymer that are doped can exceed 10%. This high degree of doping differs dramatically from the low dopant concentrations utilized in single crystal inorganic semiconductors, which are often in the range of parts per million.

For p-type doping of a conjugated polymer, an oxidizing agent serves the electron acceptor. When the IE of the polymer exceeds by the EA of the oxidant, it becomes energetically favorable for an electron from the HOMO level of polymer to

transfer to lower lying LUMO level of the oxidant. Multiple p-type doping events occurring on a single chain produces a polymeric polycation. Complexation with negatively charged counterions is required to maintain charge neutrality. The needed anions are redox products formed from the oxidizing agent. For instance, adding an electron to the oxidizing agent iron (III) chloride, $FeCl_3$, gives a $Cl^-$ anion and iron (II) chloride, $FeCl_2$, as the redox products. The $Cl^-$ anion is available for the complexation with the p-doped polymer. A multitude of p-type conjugated polymers have been studied extensively, including poly(thiophene), poly(pyrrole), poly(aniline), and their derivatives. For these polymers their neutral state ground state is the aromatic benzoid structure. The p-type doping induces a localized conformational change to the quinoid state.

The complementary situation for n-type doping involves polyanionic conjugated polymer complexes with cations derived from the reducing agent. When the HOMO level of the reducing agent is above the LUMO level of the polymer, n-type doping becomes energetically favored. Because electron-deficient monomers are generally less available, less stable in ambient air, and challenging to polymerize, n-type conjugated polymers have been less frequently studied than their p-type counterparts (Section 7.2.2) [2, 25]. Unless otherwise noted, the examples discussed in this book are for p-type conjugated polymers.

The charge carriers for n-type and p-type doped inorganic semiconductors are electrons and holes, respectively. These charge carriers are only weakly coupled to the lattice phonons. As a result, the positions of atoms in inorganic semiconductors are considered invariant to changes in dopant concentrations. In contrast, electrons and holes in conjugated polymers often display strong couplings with phonons. As a result, doping to increase the charge carrier density also produces displacements in atomic positions, such as the conformation change from benzoid to quinoid. The coupling with phonons results in quasiparticles as the charge carriers. The type quasiparticle which acts as the charge carrier depends on whether the conjugated polymer has a ground state which is degenerate (Fig. 1.4a) or nondegenerate (Fig. 1.4b).

For conjugated polymers with a degenerate ground state, doping results in soliton formation. Neutral solitons, $S_0$, have a spin of ½, whereas positively charged solitons, $S_+$, and negatively charged solitons, $S_-$, both have zero spin [2, 26, 27]. The electronic states of the solitons produce new energy bands which can either fall entirely in the gap region or partially overlap the HOMO or LUMO bands.

When the conjugated polymer has a nondegenerate ground state, low levels of doping result in the formation of polarons, which are electronic charges surrounded by phonon clouds. The spin 1/2 polarons can recombine to form bipolarons, which have zero spin [2, 26, 27]. In polymers where the recombination of two polarons to form a bipolaron is energetically favorable, bipolarons are observed at high doping levels. If bipolar formation is unfavorable, polarons persist as the charge carriers as the doping level increases [3].

In the case of p-type doping, the polarons and bipolarons are positively charged and correspond to radical cations and dications, respectively [2, 3, 22]. Majority of conjugated polymers have a nondegenerate ground state, where the benzoid structure has lower energy than the quinoid (Fig. 1.4c). Therefore, in contrast to the formation of single-bond defect in terms of soliton, the double-bond defects ($i$ and $i^*$) appear in nondegenerate conjugated polymers. In the case of bipolaron, the spectroscopic properties of conjugated polymers are influences by two subgap energy transitions from the HOMO to the localized bipolaronic states of $i$ and $i^*$. The polaronic and bipolaronic states introduce new energy bands into electronic structure (Fig. 1.4d and e). These new bands can appear entirely within the gap or can merge with HOMO or LUMO bands, reducing resulting the band gap.

If the broadening of the bands completely eliminates the energy gap, the electronic structure of the conjugated polymer becomes metal-like. It is important to note that polaronic and bipolaronic states located in the region of former energy gap are only partially delocalized, while in a true metal, all states are fully delocalized. Thus, a conjugated polymer can be metal-like in terms of a similar DOS per unit of energy and the absence of band gap. However, in a true metal, all the states are fully delocalized, which is not typically the situation in conjugated polymers.

## References


[1] Gleason KK Nanoscale control by chemically vapour-deposited polymers. Nat Rev Phys 2020, 2, 347–364.

[2] Heydari Gharahcheshmeh M, Gleason KK Texture and nanostructural engineering of conjugated conducting and semiconducting polymers. Mater Today Adv 2020, 8, 100086.

[3] Kaloni TP, Giesbrecht PK, Schreckenbach G, Freund MS Polythiophene: From fundamental perspectives to applications. Chem Mater 2017, 29, 10248–10283.

[4] Heydari Gharahcheshmeh M, Gleason KK Device fabrication based on oxidative chemical vapor deposition (oCVD) synthesis of conducting polymers and related conjugated organic materials. Adv Mater Interfaces 2019, 6, 1801564.

[5] Ahn S, Jeong SH, Han TH, Lee TW Conducting polymers as anode buffer materials in organic and perovskite optoelectronics. Adv Opt Mater 2017, 5, 1600512.

[6] Tavakoli MM, Heydari Gharahcheshmeh M, Moody N, Bawendi MG, Gleason KK, Kong J Efficient, flexible, and ultra-lightweight inverted PbS quantum dots solar cells on All-CVD-growth of parylene/Graphene/oCVD PEDOT substrate with high power-per-weight. Adv Mater Interfaces 2020, 7, 2000498.

[7] Heydari Gharahcheshmeh M, Tavakoli MM, Gleason EF, Robinson MT, Kong J, Gleason KK Tuning, optimization, and perovskite solar cell device integration of ultrathin poly(3,4-ethylene dioxythiophene) films via a single-step all-dry process. Sci Adv 2019, 5, eaay0414.

[8] Heydari Gharahcheshmeh M, Wan CT, Gandomi YA, et al. Ultrathin conformal oCVD PEDOT coatings on carbon electrodes enable improved performance of redox flow batteries. Adv Mater Interfaces 2020, 7, 2000855.

[9] Xu GL, Liu Q, Lau KKS, et al. Building ultraconformal protective layers on both secondary and primary particles of layered lithium transition metal oxide cathodes. Nat Energy 2019, 4, 484–494.
[10] Kim BH, Bae KY, Cho SH, Yoon WY Electrochemical behaviors of a vapor-phase polymerized conductive polymer coated on LiV3O8 in Li – metal rechargeable batteries. ACS Appl Mater Interfaces 2018, 10, 28695–28701.
[11] Xu G, Li Y, Ma T, et al. PEDOT-PSS coated ZnO/C hierarchical porous nanorods as ultralong-life anode material for lithium ion batteries. Nano Energy 2015, 18, 253–264.
[12] Liu A, Kovacik P, Peard N, et al. Monolithic flexible supercapacitors integrated into single sheets of paper and membrane via vapor printing. Adv Mater 2017, 29, 1606091.
[13] Ni D, Chen Y, Song H, Liu C, Yang X, Cai K Free-standing and highly conductive PEDOT nanowire films for high-performance all-solid-state supercapacitors. J Mater Chem A 2019, 7, 1323–1333.
[14] Nejati S, Minford TE, Smolin YY, Lau KKS Enhanced charge storage of ultrathin polythiophene films within porous nanostructures. ACS Nano 2014, 8, 5413–5422.
[15] Li B, Lopez-beltran H, Siu C, et al. Vaper phase polymerized PEDOT / Cellulose paper composite for flexible solid-state supercapacitor. ACS Appl Mater Interfaces 2020, 3, 1559–1568.
[16] Wang X, Ugur A, Goktas H, et al. Room temperature resistive volatile organic compound sensing materials based on a hybrid structure of vertically aligned carbon nanotubes and conformal oCVD/iCVD polymer coatings. ACS Sens 2016, 1, 374–383.
[17] Swager TM 50th anniversary perspective: Conducting/Semiconducting conjugated polymers. A personal perspective on the past and the future. Macromolecules 2017, 50, 4867–4886.
[18] Kahn A Fermi level, work function and vacuum level. Mater Horizons 2016, 3, 7–10.
[19] Ouyang J, Xu Q, Chu CW, Yang Y, Li G, Shinar J On the mechanism of conductivity enhancement in poly(3,4- ethylenedioxythiophene):Poly(styrene sulfonate) film through solvent treatment. Polymer (Guildf) 2004, 45, 8443–8450.
[20] Abtahi A, Johnson S, Park M, et al. Designing p -conjugated polymer blends with improved thermoelectric power factors. J Mater Chem A 2019, 7, 19774–19785.
[21] Heydari Gharahcheshmeh M, Robinson MT, Gleason EF, Gleason KK Optimizing the optoelectronic properties of face-on oriented chemical vapor deposition. Adv Funct Mater 2020, 2008712.
[22] Gueye MN, Carella A, Faure-vincent J Progress in materials science progress in understanding structure and transport properties of PEDOT-based materials : A critical review. Prog Mater Sci 2020, 108, 100616.
[23] Shi W, Zhao T, Xi J, Wang D, Shuai Z Unravelling doping effects on PEDOT at the molecular level: From geometry to thermoelectric transport properties. J Am Chem Soc 2015, 137, 12929–12938.
[24] Bredas JL, Street GB Polarons, bipolarons, and solitons in conducting polymers. Acc Chem Res 1985, 18, 309–315.
[25] Li H, Kim FS, Ren G, Jenekhe SA High-mobility n-type conjugated polymers based on electron-deficient tetraazabenzodifluoranthene diimide for organic electronics. J Am Chem Soc 2013, 135, 14920–14923.
[26] De CL, Appliqude T, Corporation A The role of mobile organic radicals and ions (solitons, polarons, and bipolarons) in the transport properties of doped conjugated polymers. Synth Met 1984, 9, 265–274.
[27] Heeger AJ, Kivelson S, Schrieffer JR, Su WP Solitons in conducting polymers. Rev Mod Phys 1988, 60, 781–850.

# 2 Order and orientation

## 2.1 Overview

In the introductory chapter, conjugated polymers were considered from the viewpoint of individual isolated chains. For an idealized neutral macromolecule free of defects, the conjugation length extends over the entire backbone. The electrical conduction along a linear chain is inherently 1D. Electrical conductivity is enhanced by doping.

This chapter considers ensembles of conjugated chains that form semicrystalline polymers. The intermolecular forces between the polymer chains include van der Waals forces and hydrogen bonding [1]. These forces play vital roles in the formation of the crystalline and amorphous domains. The formation of crystalline regions is driven in part by the overlap between π orbitals on adjacent chains. Weaker intermolecular forces are present in the amorphous regions.

The order and orientation in the solid polymeric matrix introduces many new phenomena. For example, the conductivity can occur in 2D or 3D. Effects that increase disorder tend to increase the localization of electronic states and lead to a corresponding decrease in charge carrier mobility. Conversely, interactions that promote delocalization of the charge carriers tend to enhance mobility [2].

**Intrachain and interchain couplings** are mechanisms to increase charge carrier delocalization (Fig. 2.1a, b). Intrachain couplings produce delocalization along a single chain. Interchain couplings occur between two adjacent chains or between different segments of the same chain, which has folded back on itself. The interchain couplings result from the overlap of two π bonding molecular orbitals. Hence, the degree of overlap is highly sensitive to the interchain distance. The intra- and interchain couplings produce shifts in the energy levels of the electronics states, which can decrease the band gap energy. When a sufficiently low band gap is reached, semimetallic and metallic-like conduction in conjugated polymers can result.

**Counterions** that complex with the doped polymer are intentionally introduced impurities. The motivation for doping is to increase the charge carrier density, which favors increased conductivity. However, each new charge carrier along the backbone has an associated counterion which increases disorder. For each new charge carrier created by a doping event, the degree of associated disorder determines if the overall electrical conductivity increases, decreases or remains the same. The type of counterion will also affect the packing of the doped conjugated polymer chains.

**Lattice phonons** can also scatter charge carriers. Thus, the temperature-dependent occupation of vibrational modes contributes to the variation of electrical conductivity with temperature.

https://doi.org/10.1515/9781501524615-002

## 2.2 Types of disorder

Long-range order in conjugated polymers is typically lower than what is found in single crystal inorganic conductors and semiconductors. Spatial disorder describes the deviation of atomic positions from a periodic lattice. Spatial disorder induces energetic disorder, as reflected by the formation of trapping states in the band gap and creation of band tails of localized states (Fig. 1.3c). In general, the electronic structure of a disordered material depends on both position and energy.

There are multiple measures of average disorder. One metric of average spatial disorder is the volume fraction of the amorphous domain. Another is the average root mean square deviation of atomic positions from crystal lattices site, known as paracrystallinity [3]. The width of the band tail states is yet another measure of the average energetic disorder.

Two materials can have the same average disorder, but differ in local disorder. Local disorder results from variations in the size and orientation of the individual crystallites. There is also variability in the geometric relationships that each crystallite has with its neighboring domains. Clearly, semi-crystalline polymers have a distinct difference in the degree of local disorder between the crystalline and amorphous domains.

Models of electronic structure simplify if the same degree of local energetic disorder is present throughout the material. In this case, the local order at each position equals the average disorder for the entire sample. The absence of local variations in disorder is easy to visualize for an amorphous glass or semiconductor having no density gradients and a completely isotropic orientation distribution.

Comparing average to local disorder is more complex in semi-crystalline materials. At measurement length scales smaller than the crystallite dimensions, the spatial disorder clearly varies with position. High disorder will be present in the amorphous regions and low disorder will be found in the crystalline domains. However, at larger measurement length scales, both amorphous and crystalline domains will be sampled together, providing an averaged value. It is possible for this microscale spatial average to be independent of position and be equal to the macroscopic average.

The extent of wave function delocalization is a characteristic length scale for the electronic structure. A sufficient degree of delocalizaton allows charge carriers to experience the average disorder over multiple domains. Thus, the disordered averaged over the extent of the wave function can become the same at each position, even though there is a distinct variation in spatial disorder at smaller length scales. As the extent of the electronic states increases, the overall electronic structure more closely approaches the classical band transport conduction model for inorganic crystalline solids.

In the absence of variation in the local energetic disorder, the electronic structure can readily be displayed on a band energy diagram, such as Fig. 1.3c. These diagrams display the density of states at a given energy. The band shapes are given by relationships such as eq. (1.1), in which the density of states, $g(E)$, is only a function of energy. No coordinates of physical position appear in eq. (1.1) or are represented in Fig. 1.3c.

Shading, or lines of limited extent, schematically indicates the varying extents of delocalization. However, the diagram makes no explicit linkage between any given electronic state and a physical location in the sample.

When the extent of the electronic wave function is too small to average the effects of spatial disorder, the density of states is a function of both energy and position. The added dimensions of physical space lead to more complex models and graphical representations.

**Point defects** are an additional source of disorder. The point defects can act as scattering centers and traps, hence reducing charge carrier mobility. For example, some of the chains in the ensemble will have defects in bonding configurations that prevent conjugation from forming along the entire backbone. Reducing conjugation length corresponds to localization of the π bonding electronic states. Impurities, incorporated into the matrix, either intentionally or unintentionally, are point defects that create new localized electronic states.

## 2.3 Intrachain coupling

Various defects can disrupt the conjugation along the backbone and lead to discrete electronic states localized on a subsegment of the chain. High doping levels can cause these states to broaden and overlap, allowing the generation of 1D intrachain charge carrier coupling. Figure 2.1a shows schematically shows how intrachain coupling creates a pathway for charge transport between the localized segments along a single chain. The delocalization promoted by intrachain coupling is generally favorable for enhancing charge transport.

Conjugation requires that all of the p-orbitals participating in π bonding have the same orientation. Thus, conjugation can be disrupted by conformational defects along the backbone, including simple torsion. Additionally, variations in bonding configurations are possible if a monomer lacks symmetry along the chain direction. If conjugation only results from head-to-tail linkages, head-to-head and tail-to-tail configurations represent defects. If the synthesis is controlled to achieve only a single type of linkage, the resulting polymer is said to be regioregular.

Monomers that polymerize through sites on their aromatic rings can lead to multiple bonding configurations during synthesis. Chain formation requires reaction at two locations on the ring. The conformation of the chain depends on the positions of the two sites participating in polymerization. For example, consider thiophene, which is a five-membered ring (Fig. 1.4b). A sulfur atom is at the first position, and the $sp^2$ hybridized carbon atoms occupy positions 2, 3, 4, and 5. To form a straight chain, the polymerization of thiophene must occur through positions 2 and 5, as shown in Fig.1.4b. If, instead, polymerization proceeds through position 3 or 4, the chain will acquire a kink. Nonlinear chain conformations tend to both lower charge transport mobility along the chain and reduce the ability of the chains to assemble into crystallites.

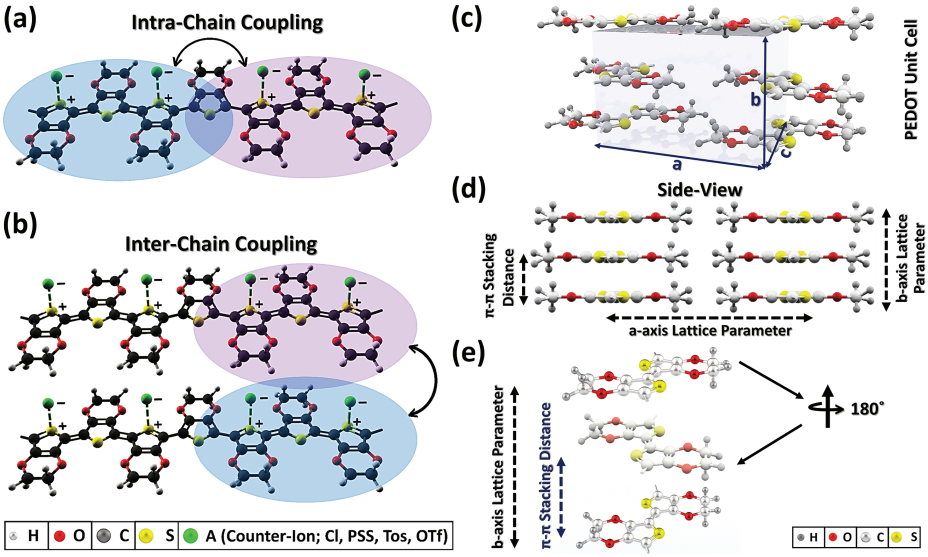


**Fig. 2.1:** Schematic depiction of regions of conjugation region (shaded ovals) in doped poly(3,4-ethylenedioxythiophene) (PEDOT). Overlap of the molecular orbitals produces (a) intrachain or (b) interchain coupling [1]. (c) Off-angle and (d) side-views of neutral PEDOT having an orthorhombic crystal structure with lattice parameters *a*, *b*, and *c* [1]. The polymer backbone lies along the *c*-axis. The side view (d) gives the clearest view of the distance between the π–π stacking planes, which is equal to b/2. (e) The orientation of EDOT monomeric units alternate with 180° along the polymer backbone to achieve a minimum energy configuration. (a–d) Adapted with permission from [1], Heydari Gharahcheshmeh and Gleason, Mater. Today Adv., 8, 10008 (2020) Copyright 2020, Elsevier.

Monomer design can reduce the possibility of variation in bonding configuration along the chain. The goal of achieving linear regioregular polymer chains motivates the synthesis of substituted thiophene monomers. Incorporating organic substituents at position 3, or at both positions 3 and 4, blocks polymerization at the corresponding positions, increasing the probability of polymerization proceeding through positions 2 and 5. Thus, the substituted thiophene monomers are more likely to produce linear macromolecular chains.

Figure 2.1 shows the chemical structure of poly(3,4-ethylenedioxythiophene) (PEDOT). The symmetry of the monomer unit avoids the potential for head-to-head or tail-to-tail defects. Additionally, the back-bonded ring blocks polymerization at the 3 and 4 positions of the thiophene ring. Thus, polymerization occurs only through positions 2 and 5, yielding linear chains. The linear PEDOT chains are favorable for intrachain charge carrier mobility (Fig. 2.1a). Additionally, the linear chains can readily pack together, creating the possibility for overlap of the molecular orbitals from adjacent chains to produce interchain coupling (Fig. 2.1b).

## 2.4 Interchain coupling

Chain packing controls the overlap of π bonding orbitals responsible for interchain couplings (Fig. 2.1b). This type of packing is most probable in the crystallites but can occur to a more limited extent in the amorphous domains. The interchain couplings are important for achieving high charge carrier mobility. Although weaker than the intrachain couplings, the interchain couplings increase the number of potential pathways for charge transport. When the new pathways avoid regions where charge localization occurs, mobility can be enhanced. For example, for a chain containing a defect that would interrupt intrachain transport, an interchain coupling can allow charge transport to proceed on an adjacent chain. Heavy levels of doping can produce 3D extended electronic states that enable metallic-like conduction.

One geometry of chain packing favorable for intrachain coupling will be illustrated using PEDOT. Each monomer unit contains a five-membered thiophene ring which connects through the 3 and 4 positions to a six-membered ring. For adjacent monomer units, the orientation of the six-member backbonded ring differs by 180°. In this configuration, the sulfur from one monomer unit can interact with the oxygen on an adjacent unit, helping to planarize the PEDOT chain [4].

The orthorhombic crystal structure of PEDOT is shown from different perspectives in Fig. 2.1c–e. The backbone of each chain lies along the *c*-axis direction. As a result of the strong intrachain couplings, charge carrier mobility is highest along the direction of the *c*-axis. The *c*-axis lattice parameter corresponds to the width of the thiophene ring [1]. Indeed, the *c*-axis lattice parameter of 0.76 nm for PEDOT is similar to the values obtained for other thiophene-based polymers [4].

The π–π stacks that produce intrachain coupling occur along the *b*-axis. Thus, the *b*-axis direction has the second-highest values of charge carrier mobility. As the chains stack along the *b*-axis (Fig. 2.1d), the direction of the monomer unit alternates by 180º. Thus, the π–π stacking distance is half of the *b*-axis lattice parameter, *b*/2. The π–π stacking distance varies with processing conditions and, as will be discussed in Section 2.6, with the type of counterion. Lower values of the π–π stacking distance are expected to allow for more significant overlap and hence increased delocalization.

The side view (Fig. 2.1d) reveals that the *a*-axis lattice parameter represents the width of the PEDOT chain, 1.4 nm [5]. The lowest charge carrier mobility occurs along the direction of the *a*-axis [1, 5].

## 2.5 Orientation

The orientations of nanocrystallites in a conjugated polymer film relative to the surface can be influenced by the conditions of synthesis and post-processing steps, such as annealing or rinsing. Orientation can also be influences by interfacial forces, which

become significant relative to bulk forces with decreased film thickness or reduced nanostructure dimension.

The π bonding plane can be considered to be a lamella which has three possible preferential textures: face-on, edge-on, and end-on. For the face-on texture (Fig. 2.2a), both the lamella and the *c*-axis are parallel to the substrate's surface. For edge-on texture (Fig. 2.2b), the *c*-axis remains parallel to the surface, but the lamella adopts an orientation perpendicular to the surface. In end-on-texture, both the lamella and *c*-axis are perpendicular to the surface (not shown). The lamella can also possess a mixture of preferential textures or have a random orientation. It is also possible for conjugated polymers to be fully amorphous.

Nonrandom distributions of nanocrystallite orientations can give rise to anisotropic transport properties. For example, the high carrier mobility along the polymer backbone is likely to lead to higher electrical conductivity along the direction of intrachain conjugation. Orientation also influences the magnitude of charge carrier scattering at the grain boundaries. For a thin film, these effects can lead to a difference between in-plane versus out-of-plane properties.

Differences in ionic transport with texture have also been observed [6–8]. High ion conductivity is desired for electrochemical energy storage applications for which the

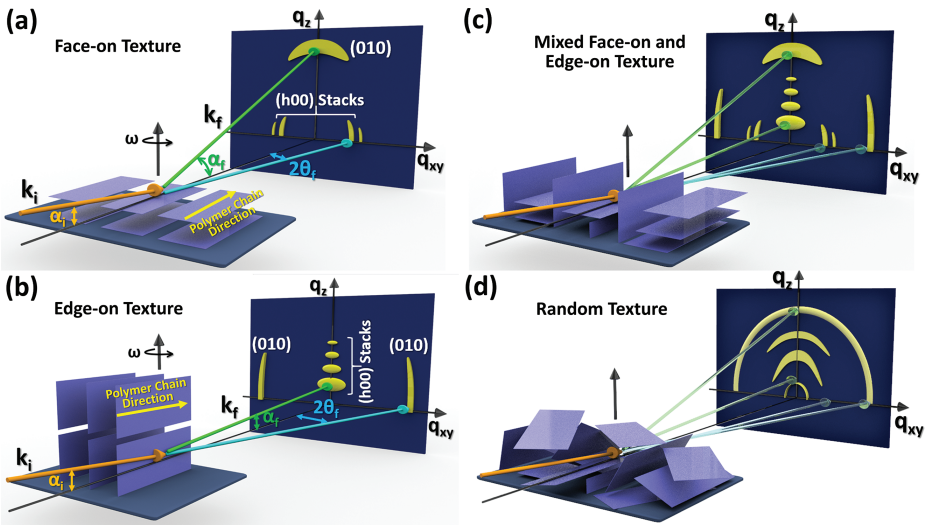


**Fig. 2.2:** Grazing incidence wide-angle X-ray scattering (GIWAXS) gives distinctive 2D patterns for (a) face-on and (b) edge-on preferential texture. The geometry of the incident X-ray wavevector, $k_i$, and the forward scatter X-ray wavevector, $k_f$, are shown in both (a) and (b). The $q_z$ versus $q_{xy}$ GIWAXS 2D patterns are also displayed for (c) mixed and (d) random textures. Adapted with permission from [1], Heydari Gharahcheshmeh M and Gleason KK, Mater. Today Adv., 8, 10008 (2020) Copyright 2020, Elsevier.

conjugated polymer provides Faradaic pseudocapacitive charge storage. Repeated doping and dedoping of the polymers corresponds to cycles of charging and discharging.

### 2.5.1 Measuring order and orientation

Quantifying order and orientation in semicrystalline conjugated polymers is essential for developing property-processing relationships. As discussed in Section 2.2, metrics of average disorder include amorphous fraction, paracrystallinity, and width of the band tail. The ordered regions will have a defined symmetry for chain packing and associated lattice parameters. Crystallites can vary in both physical dimension and orientation. For thin films, the distribution of crystallite orientations relative to the surface of the substrate, known as the texture, is critically important. Indeed, nonrandom distributions can lead to anisotropy in the material properties.

Various microscopy techniques have revealed valuable insights into the structure of semicrystalline conjugated polymers [9]. The surface morphology is readily probed using atomic force microscopy. Bulk structural characteristics are revealed by transmission electron microscopy (TEM). However, TEM sample preparation is often time-consuming and is destructive to the sample. Quantitative bulk measurements of nanostructure and texture can also be obtained using X-ray characterization methods. Little or no sample preparation is required for the nondestructive X-ray measurements.

For X-ray diffraction (XRD), the incident X-ray beam is diffracted by the periodic planes of atoms of the crystallites. The conditions for constructive interference of an X-ray beam of wavelength $\lambda$, arriving at an angle of incident of $\theta$, are given by **Bragg's law** [10]:

$$d_{hkl} = \frac{n\lambda}{2\sin\theta} \tag{2.1}$$

where $d_{hkl}$ is the spacing between the periodic atomic planes; the integers $h$, $k$, and $l$ are the Miller indices of the plane; and the integer $n$ is the order of the reflection.

The full width at half maximum of the diffraction peak, $\beta$, can be used to estimate the average crystallite size, $D$, using the **Scherrer equation:**

$$D = \frac{s\,\lambda}{(\beta - \beta_{\text{inst}})\cos\theta} \tag{2.2}$$

where $s$ is the dimensionless shape factor, which is typically set to 0.9, and $\beta_{\text{inst}}$ is the instrumental broadening. Equation (2.2) reveals the inverse correlation between $\beta$ and $D$. Thus, sharp peaks having low values of $\beta$ indicate large crystalline domains. Increasing $D$ can contribute to enhanced charge transport [11–13].

Geometries for X-ray analysis include transmission, reflection, and grazing incidence (GI) [1]. For thin films, GI is preferred because it minimizes interference from

signals arising from the substrate. When a point detector is employed, the method is known as grazing incidence XRD (GIXRD, or sometimes abbreviated GIXD). Using area detectors allows measurement of X-ray scattering, which is particularly valuable for disordered materials, including conjugated polymers. Reducing the distance between the sample and the detector widens the observable range of scattering angles. Wide-angle scattering probes the smallest structural dimensions. Thus, grazing incidence wide-angle X-ray scattering (GIWAXS) provides short-range (~5 to ~20 nm) structural characterization of disordered conjugated polymer thin films. Longer range order (~10 to ~1000 nm) can be probed by other X-ray methods, such as polarized resonant soft X-ray scattering [14].

Figure 2.2 shows the GI geometry, where the incident X-ray beam is at a grazing angle, $\alpha_i$, with respect to the surface of the thin film. The smaller the value of $\alpha_i$, the greater the degree of surface sensitivity. However, $\alpha_i$ must remain above the critical angle to avoid total internal reflection by the sample. The forward scattered beam makes an angle of $\alpha_f$ with respect to the surface and has an in-plane angle of $2\theta_f$. The components of the forward scattering wavevector are

$$q_{xy} = \left|q_{xy}\right| = (q_x^2 + q_y^2)^{\frac{1}{2}} = \frac{2\pi}{\lambda}\left\{\left[\cos(2\theta_f)\cos(\alpha_f) - \cos(\alpha_i)\right]^2 + \left[\sin(2\theta_f)\cos(\alpha_f)\right]^2\right\}^{\frac{1}{2}} \tag{2.3}$$

and

$$q_z = \frac{2\pi}{\lambda}\left[\sin(\alpha_f) + \sin(\alpha_i)\right] \tag{2.4}$$

The 2D GIWAXS patterns are often displayed as 2D diagrams of $q_z$ versus $q_{xy}$, as shown schematically in Fig. 2.2. The magnitude of $q_z$ equals $2\pi/d_{hkl}$. When a single texture is present, sharp features emerge associated with $n$ order scattering from periodically spaced planes with Miller indices ($h$, $k$, $l$). For the same material, changing only the texture with respect to the substrate results in a dramatic change in GIWAXS pattern, as can be seen by comparing face-on (Fig. 2.2a) to edge-on (Fig. 2.2b) texture. For a film with mixed texture, the GIWAXS pattern will contain the features from each texture present (Fig. 2.2c, d). For an isotropic distribution of crystallites, circular rings will emerge.

### 2.5.2 Interfacial effects

At smaller dimensions, interfacial energies become more important in determining morphology. The impact of vertical confinement can be studied using systematic variations in film thickness.

The effects of vertical confinement were quantified for films of poly(3-hexylthiophene-2,5-diyl) with [6,6]-phenyl C61 butyric acid methyl ester. Such a solid-state

mixture of conjugated polymer with a fullerene has been widely studied for fabricating organic solar cells. The crystallite size was determined by a Scherrer analysis on the widths of the (100) GIWAXS scattering peak from the conjugated polymer. The smallest average crystallite size, 6.86 ± 0.04 nm, was observed in the thinnest film, 15 nm. As film thickness increased up to 200 nm, crystallite size also increased. Further increasing film thickness to a maximum value of 920 nm produced no further crystallite size changes. For thickness >200 nm, the average crystallite size plateaued at ~21 nm. The GIWAXS analysis showed that all films displayed an edge-on texture, with the thinnest films having the highest degree of orientation.

The texture of the nanocrystallites in the near interfacial region can be altered by surface engineering. Films synthesized under otherwise identical conditions displayed either edge-on or face-on texture depending on if their interfaces were grafted or nongrafted, respectively [12]. The interfacial energies at both film interfaces can alter polymer morphology, a phenomenon that has been widely adopted for controlling the orientation of lamella in block copolymers [15].

Nanostructures represent 2D or 3D confinement. Templating methods for nanowires, 100-nm wide and 150-nm wide, have resulted in single-crystal PEDOT [16]. These remarkable electronic transport characteristics or these nanowires will be discussed further in Chapter 3. Confined PEDOT growth has also been demonstrated within the nanophase segregated structure of block copolymers [17].

### 2.5.3 Grain boundaries

In disordered inorganic materials, crystallites are sometimes referred to as grains. Grain boundaries represent a quasi-2D disruption to long-range order [1]. The barrier to electronic transport between two adjacent grains can depend on texture. The distortion can be minimized if the two grains have a similar orientation (Fig. 2.3a). In this low-angle grain boundary regime, the barrier to charge transport by quantum mechanical jumps is lowered. A significant difference in orientation between a pair of crystallites corresponds to a high-angle grain boundary (Fig. 2.3b). A mismatch in orientation increases the barrier to hopping transport.

Additional considerations arise at the grain boundaries of conjugated polymers. Polymer chains can directly interconnect crystallites. These tie chains bridge through the amorphous domain and represent an added pathway for electronic transport [1, 11, 18]. Tie chains with a linear backbone configuration provide the highest degree of conjugation and thus the maximum charge carrier mobility. The formation of a linear bridge requires the adjacent crystallites to have similar orientations, corresponding to a low-angle grain boundary. A high-angle grain boundary results if there is larger degree of misorientation. In this case, many of the tie chains will have nonlinear configurations, making these interconnections less conductive.

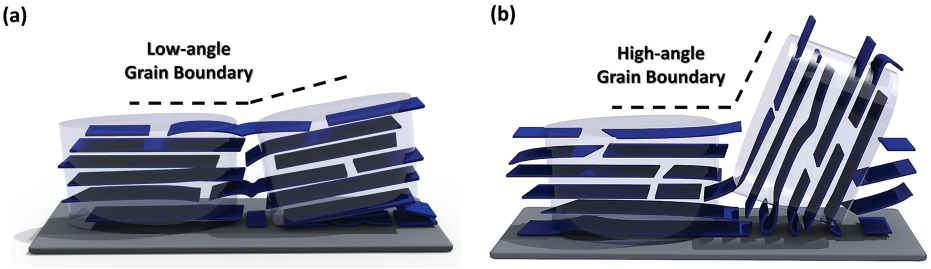


**Fig. 2.3:** Lamella of π bonding conjugation (dark blue) is shown for two adjacent crystallites for orientations corresponding to (a) a low-angle grain boundary and (b) a high-angle grain boundary. Reprinted with permission from Heydari Gharahcheshmeh and Gleason, Mater. Today Adv., 8, 10008 (2020) Copyright 2020, Elsevier.

In an isotropic distribution, all orientations are possible. Thus, the probability of two adjacent crystallites having the same orientation is low. When a pure preferential orientation exists, the likelihood of adjacent crystallites having the same orientation improves, creating a high fraction of low-angle grain boundaries. The presence of vertical confinement will further reduce the number of possible orientations and increase the probability of a low-angle grain boundary. Conversely, mixed texture is likely to increase the occurrence of high-angle grain boundaries.

## 2.6 Counterions

Many different types of counterions have been used in doped conjugated polymers [19]. Anions for p-type polymers can be single atoms (e.g., $Cl^-$, $Br^-$, $I^-$), molecular ions (e.g., $PF_6^-$), or polyions (e.g., poly(styrene sulfone) (PSS)). The molecular ions can be further classified according to their geometry. These classes include tetragonal anions, such as $ClO_4^-$ and $HSO_4^-$; or planar anions, tosylate ($Tos^-$, $H_3C\text{-}C_6H_4\text{-}SO_3^-$)$NO_3^-$ [20]. The geometry of the anions plays a role in the crystal structure adopted by the doped nanocrystals in the conjugated polymer.

In oxidative synthesis, the oxidant reacts with monomers and oligomers to produce higher molecular weight chains. The oxidant also produces counterions through redox reactions with the polymer to dope the chains. Requirements for solubility or volatility constrain the selection of the oxidant used with a given film forming method. Thus, when considering the role of counterions, care must be taken to factor in the potential impacts of the various processes used in polymer synthesis and thin film formation. For PEDOT, examples of counterions commonly associated with different processing methods are [21]:

- PSS for solution application,
- $Cl^-$ for oxidative chemical vapor deposition, and
- $Tos^-$ for vapor-phase polymerization (VPP) and in situ chemical polymerization.

Counterions can also be introduced through post-processing treatments. These post-treatments can result in doping. For instance, exposing neutral poly(acetylene) to iodine gas, $I_2$, can achieve doping where $I^-$ is the counterion [22]. For poly(2,5-bis(3-tetradecylthiophen-2-yl)thieno [3,2-b]thiophene) (PBTTT), organic acceptors were introduced by vapor-phase and solution processing. Both processes yielded p-type doping of PBTTT with the planar molecule 2,3,5,6-tetrafluoro-7,7,8,8-tetracyanoquinodimethane [14]. Post-processing steps can also use to cause ion exchange between a doped polymer and salt or acidic solution containing a different anion. The ion exchange process can be referred to as secondary doping [23].

The type of counterion selected can dramatically alter the conformation of the individual chains in the amorphous domains, as observed in electrochemically polymerized PEDOT [24]. Small counterions minimize the disruption to the random coil morphology of the polymer. As electrostatic interactions increase with the counterion size, the polymer chain adopts a more extended configuration. Conductivity increases as the chains become more extended.

The type of counterion and the doping level effect crystallization. With the large macromolecular counterion PSS, the ordered packing of the PEDOT chains can be inhibited, and the amorphous phase can dominate. When crystallinity is present, the *a*-axis lattice parameter can increase with doping level, suggesting that the PSS resides outside the π–π stacks (Fig. 2.1d,e) [1]. For smaller counterions, PEDOT nanocrystallites typically have dimensions between 4 and 10 nm [9]. The type of counterion and the doping level can impact both the *a*-axis and *b*-axis lattice parameters. A change in the *b*-axis parameter suggests that the anion resides within the π–π stack. In a study of VPP synthesized PEDOT, ion exchange was used to vary the type of counterion. For the *a*-axis lattice parameter, the maximum value, 1.43 nm, resulted from complexation with $Tos^-$. The minimum value, 1.26 nm, was found for $ClO_4^-$ and the $NO_3^-$ counterions [20]. At high doping levels (>50%), molecular dynamics simulations suggest that the planar anions $Tos^-$ and $NO_3^-$ may intercalate into the π–π stacks [20]. This type of sandwich structure is not predicted to form with the tetrahedral $ClO_4^-$ anion.

Electronic transport may be influence by the location of the counterions in the conjugated polymers. The ions represent point defects that can scatter charge carriers. A reduced degree of scattering is anticipated if the ions are spatially separated from the path for electronic conduction produced by the π bonding orbitals [25].

## References


[1] Heydari Gharahcheshmeh M, Gleason KK. Texture and nanostructural engineering of conjugated conducting and semiconducting polymers. Mater Today Adv 2020, 8, 100086.

[2] Reynolds JR, Thompson BC, Skotheim TA. Conjugated Polymers Properties, Processing, and Applications, 4th Edition. Boca Raton, London, New York, CRC Press, Taylor and Francis Group, 2019.

[3] Abutaha A, Kumar P, Yildirim E, et al. Correlating charge and thermoelectric transport to paracrystallinity in conducting polymers. Nat Commun 2020, 11, 1–8.

[4] Kim EG, Brédas JL. Electronic evolution of poly(3,4-ethylenedioxythiophene) (PEDOT): From the isolated chain to the pristine and heavily doped crystals. J Am Chem Soc 2008, 130, 16880–16889.

[5] Aasmundtveit KE, Samuelsen EJ, Pettersson LAA, Inganäs O, Johansson T, Feidenhans'l R. Structure of thin films of poly(3,4-ethylenedioxythiophene). Synth Met 1999, 101, 561–564.

[6] Moni P, Lau J, Mohr AC, et al. Growth temperature and electrochemical performance in vapor-deposited Poly(3,4-ethylenedioxythiophene) thin films for high-rate electrochemical energy storage. ACS Appl Energy Mater 2018, 1, 7093–7105.

[7] Arnold SP, Harris JK, Neelamraju B, Rudolph M, Ratcliff EL. Microstructure-dependent electrochemical properties of chemical-vapor deposited poly(3,4-ethylenedioxythiophene) (PEDOT) films. Synth Met 2019, 253, 26–33.

[8] Heydari Gharahcheshmeh M, Wan CT, Gandomi YA, et al. Ultrathin conformal oCVD PEDOT coatings on carbon electrodes enable improved performance of redox flow batteries. Adv Mater Interfaces 2020, 7, 2000855.

[9] Kim N, Petsagkourakis I, Chen S, et al. Electric Transport Properties in PEDOT Thin Films from: Conjugated Polymers, Properties, Processing, and Applications. CRC Press, 2019, p.

[10] Cullity BD. Elements of X-Ray Diffraction. Addison-Wesley. London, Addison-Wesley, 1978.

[11] Heydari Gharahcheshmeh M, Robinson MT, Gleason EF, Gleason KK. Optimizing the optoelectronic properties of face-on oriented chemical vapor deposition. Adv Funct Mater 2020, 2008712.

[12] Ugur A, Katmis F, Li M, et al. Low-dimensional conduction mechanisms in highly conductive and transparent conjugated polymers. Adv Mater 2015, 27, 4604–4610.

[13] Heydari Gharahcheshmeh M, Gleason KK. Device fabrication based on oxidative chemical vapor deposition (oCVD) synthesis of conducting polymers and related conjugated organic materials. Adv Mater Interfaces 2019, 6, 1801564.

[14] Patel SN, Glaudell AM, Peterson KA, et al. Morphology controls the thermoelectric power factor of a doped semiconducting polymer. Sci Adv 2017, 3, e1700434.

[15] Bita I, Yang JKW, Jung YS, Ross CA, Thomas EL, Berggren KK. Graphoepitaxy of self-assembled block copolymers on two-dimensional periodic patterned templates. Science (80-) 2008, 321, 939–943.

[16] Cho B, Park KS, Baek J, Oh HS, Koo Lee YE, Sung MM. Single-crystal poly(3,4-ethylenedioxythiophene) nanowires with ultrahigh conductivity. Nano Lett 2014, 14, 3321–3327.

[17] Lee YH, Oh J, Lee S, Kim H, Son JG. highly ordered nanocon fi nement effect from evaporation-induced self-assembly of block copolymers on in situ polymerized PEDOT:Tos. ACS Macro Lett 2017, 6, 386–392.

[18] Heydari Gharahcheshmeh M, Tavakoli MM, Gleason EF, Robinson MT, Kong J, Gleason KK. Tuning, optimization, and perovskite solar cell device integration of ultrathin poly(3,4-ethylenedioxythiophene) films via a single-step all-dry process. Sci Adv 2019, 5, eaay0414.

[19] Le TH, Kim Y, Yoon H. Electrical and electrochemical properties of conducting polymers. Polymers (Basel) 2017, 9, 150.
[20] Rudd S, Franco-gonzalez JF, Singh SK, et al. Charge transport and structure in semimetallic polymers. J Polym Sci Part B Polym Phys 2018, 56, 97–104.
[21] Gueye MN, Carella A, Faure-vincent J. Progress in materials science progress in understanding structure and transport properties of PEDOT-based materials : A critical review. Prog Mater Sci 2020, 108, 100616.
[22] Heeger AJ. Semiconducting and metallic polymers : The fourth generation of polymeric materials ( Nobel Lecture). Angew Chem Int Ed 2001, 40, 2591–2611.
[23] Itoh K, Kato Y, Honma Y, et al. Structural alternation correlated to the conductivity enhancement of PEDOT:PSS films by secondary doping. J Phys Chem C 2019, 123, 13467–13471.
[24] Culebras M, Gomez CM, Cantarero A. Enhanced thermoelectric performance of PEDOT with different counter-ions optimized by chemical reduction. J Mater Chem A 2014, 2, 10109–10115.
[25] Kivelson S, Heeger AJ. Intrinsic conductivity of conducting polymers. Synth Met 1988, 22, 371–384.

# 3 Electronic transport

This chapter explores electronic transport in semicrystalline conjugated polymers from multiple perspectives [1–6]. Despite the complex morphology and texture present in the macromolecular condensed phase, insights into charge carrier behavior can be gained from applying fundamental concepts from solid-state physics, materials science, and organic chemistry.

The synthesis and processing methods for conjugated polymers continue to evolve, improving the control over order, orientation, and properties. Characterization methods to quantify this improvement have also advanced. Better materials and improved measurements provide the required knowledge base for rationally designing and engineering conjugated polymers.

Mechanistic hypotheses regarding charge transport can be tested by combining controlled synthesis with targeted electronic characterization. The electronic characterization may explore systematic changes in temperature, pressure, doping level, electric field, or magnetic field. Selective comparisons of theory to experiments will be discussed.

In a perfect, infinite single crystal, the density of states (DOS) depends only the energies of the electronic states. Because each lattice site of the crystal is identical and the wave functions extend over the entire lattice, spatial location need not be considered. Thus, no variation in charge transport occurs for different positions on the lattice. The ability to consider charge transport solely as a function of energy is the reason DOS diagrams are so useful for crystalline solids.

In contrast, the electronic transport characteristics of conjugated polymers require simultaneous consideration of both energetic and spatial disorder. Spatial disorder localizes charge carriers. As discussed in Chapter 2, conjugated polymers display a variety of morphological features. The corresponding spatial disorder is not uniform across the polymer, as shown schematically in Fig. 3.1. Since the amorphous region is more disordered than the crystalline regions, a higher density of localized electronic states will be found in the amorphous regions. Additionally, the energies associated with the localized states are not uniformly distributed in the DOS diagram. For example, the localized states in Fig. 3.1c are found at the energies associated with the band tails and trapping states. Mobile charge carriers occupy only those states in the DOS within a few $k_B T$ of $E_F$. Thus, different charge transport behaviors are expected if the states with energies near $E_F$ are localized or extended.

By controlling crystallinity and orientation, the corresponding increase in the extent of the wave functions provides spatial averaging over conjugated polymer morphology (Section 2.2). With this averaging, charge transport will depend only on the energy of the electronic states, analogous to the situation discussed above for a single crystal. In this case, solid-state physics models of electronic transport, typically applied to disordered inorganic solids, can also be applied to conjugated polymers. These models include classical and semiclassical approaches and electronic

https://doi.org/10.1515/9781501524615-003

band structure theory derived from quantum mechanics. In some cases, metallic-like conductivity can be achieved.

When higher levels of disorder remain, the wave functions are more localized and electronic transport through phonon-assisted hopping between localized sites. Disordered conjugated polymers may behave as electrical insulators at low levels of hopping conduction. Electronic transport models must consider that localized states occur only at particular locations and have only specific energies. One approach is to consider spatial disorder at the level of the macromolecule, where intrachain and interchain charge transport are distinctly different. Alternately, the spatial inhomogeneity can be deemed to arise from the difference in charge transport between the crystalline and amorphous domains.

A generalized model provides simultaneous consideration of both spatial and energetic disorders [4]. In the presence of inhomogeneous disorder, electronic transport behavior has a multiscale nature [7]. Charge transport may be rapid over short distances, and hence for short times. For example, a charge carrier mobility along a single macromolecular chain can be high. Longer range transport may proceed at slower rates corresponding to an interchain or intercrystallite hop.

Many models have been proposed to provide insight into the complex charge transport in organic semiconductors. The models for the electronic structure of conjugated polymers discussed in this chapter will be classified into three groups. An overview of each group is given in the paragraphs that follow. More extensive discussion for each of the three approaches is provided in the subsequent sections of this chapter. The models selected for discussion enable trends in electronic characteristics to be evaluated across multiple materials and can provide specific insight useful for designing and optimizing conjugated polymers.

For a given polymer with a specific nanomorphology (Fig. 3.1), multiple approaches can be applied. The use of one method does not render another approach incorrect. However, for a particular case, more insights will be derived by using an informed choice of the appropriate type of model.

**Group I models** start by considering states that are fully extended over the entire polymeric solid. Then the addition of defects and structural disorder introduces localization of the charge carriers. This approach is often applied to disordered inorganic semiconductors. While crystalline inorganic semiconductors like silicon are more familiar, a greater degree of morphological similarity exists between polycrystalline inorganic semiconductors and semicrystalline conjugated polymers. Transparent conducting oxides (TCO) are one class of polycrystalline semiconductors [8–10]. Like conjugated polymers, TCOs can have high levels of doping. TCOs have been widely utilized in optoelectronic devices such as displays and photovoltaics. For these applications, conjugated polymers have been explored as mechanically flexible alternatives to TCOs. Technologically relevant TCOs include indium tin oxide (ITO), aluminum-doped zinc oxide (AZO), and fluorine-doped tin oxide.

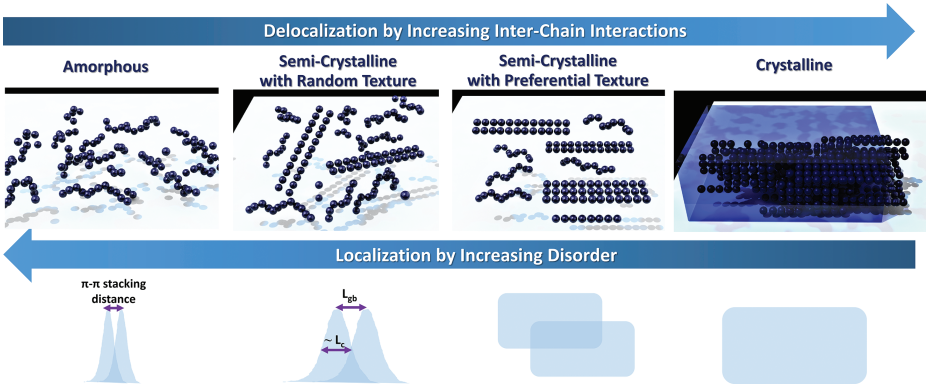


**Fig. 3.1:** Top row, left to right: Schematic representations of spatial disorder for amorphous, semicrystalline with random texture, semicrystalline with preferential texture, and single crystal domains. The extent of the corresponding electronic states is shown schematically along the bottom row, revealing the overlap of the molecular orbitals between two chains (Group II), the overlap of coarse-grained wave functions from the nanocrystals (Group III), and fully extended states (Group I).

**Group II models** start from the localized molecular orbitals of the polymer chains. Adding interactions between the chains partially delocalizes the wave functions. The viewpoint of intrachain and interchain contributions for conjugated polymers does not find an analogy to TCOs. However, the concepts of intramolecular and intermolecular interactions are essential in organic semiconductors [11]. In both conjugated polymers and organic semiconductors, π–π stacking is often the strongest form of intermolecular interactions between electronic orbitals (Fig. 2.1b). One key parameter for Group II models is the π–π stacking distance. Another is the distribution of orientations for the π–π stack direction, which describes the polymer's nanotexture.

**Group III models** represent semicrystalline polymers as a mixture of ordered and disordered regions. For the ordered domains, coarse-grained models consider states that fully extend over the nanocrystals but have a limited degree of extent into the surrounding amorphous phase. Group III models are appropriate when intercrystallite transport limits the overall charge carrier mobility. With advanced control over polymer morphology, the intercrystalline resistance to charge transport can be reduced. In this case, Group I models become more appropriate.

Electrical conductivity, $\sigma$, depends on the direction and frequency of the measurement. Unless otherwise specified, this chapter considers the dc conductivity of thin films in the plane of the substrate. The frequency dependence of electrical conductivity and its relationship to optical properties will be discussed in Chapter 4.

## 3.1 Extended and localized electronic states

This section explores the role of energetic inhomogeneity in the charge transport behavior of conjugated polymers. For some range of energies, states are localized, leading to relatively immobile charge carriers. In other ranges of energy, partially extended states allow for higher charge carrier mobility.

In a periodic solid, the electronic wave functions, known as Bloch waves, extend over the entire lattice. The energy for a given state will fall within quantum-mechanically allowed bands. Thus, there is a sharp transition between the finite value of $g(E)$ at the edge of the band to $g(E) = 0$ in the band gap. Within the energy range of the band, $g(E)$ has a constant value, a characteristic described as a flat band structure. As discussed in Chapter 2, several types of disorder reduce the extent of the electronic states in semicrystalline conjugated polymers. The spatial disorder produces energy bands in the DOS that are not flat (Fig. 1.3c).

The **Gaussian disorder model (GDM)** approximates the DOS for the HOMO and LUMO bands as Gaussian functions [12, 13]. For a band having a mean energy of $E_o$, the band shape as a function of energy, $E$, is given by

$$g(E) = \frac{N_0}{\sigma_{DOS}\sqrt{2\pi}} \exp\left(\frac{-(E-E_0)^2}{2\sigma_{DOS}^2}\right) \tag{3.1}$$

In this DOS expression, $N_0$ is the total DOS, including spin degeneracy per unit volume, and $\sigma_{DOS}$ is the standard deviation of the collection of individual energy levels. Large values of $\sigma_{DOS}$ indicate high-level disorder. With increasing disorder, the width of the Gaussian tails of the HOMO and LUMO bands increase, causing the bandgap to decrease. In the case of heavily doped nondegenerate conjugated polymers, the bipolaron bands (Fig. 1.4e) will also cause the band gap to decrease.

The states in the center of a band, that is, having energies near $E_0$, are considered to be delocalized and have high mobility (dark shaded regions in Fig. 1.3c). In contrast, the band tails contain localized states of limited mobility (light shaded regions in Fig. 1.3c). The critical energy, $E_c$, divides the extended states at the center of the band from the localized states in the band tail. Thus, $E_c$ is also known as the mobility edge. For this band energy description, metallic-like conduction occurs if the Fermi energy, $E_F$, lies in a band of extended states. When $E_F$ is in a region of the DOS with localized states, conduction proceeds through a thermally activated hopping charge transport mechanism.

The lighter shading in Fig. 1.3c schematically shows energy ranges where localized states are found in the band tails. Additionally, this energy diagram indicates several discrete localized energy states that act as traps for electronic charge carriers. The trapping states are an additional manifestation of disorder in the conjugated polymer. The traps are classified as shallow or deep, depending on their energy. Shallow traps have

energies separated by only a few $k_B T$ from the band edge, while the energies for deep traps are further removed from the band edge.

The GDM model has been successfully used with many types of conjugated polymers and organic glasses [5]. The corresponding $\sigma_{DOS}$ values are often in the range of ~50 to ~150 meV. For $N_0$, the typical range is ~$10^{20}$ to ~$10^{21}$ $cm^{-3}$.

## 3.2 Metal–insulator (M–I) transition

The semiclassical criteria for metallic behavior can be thought of from either the perspective of energy or distance [14, 15]. From the viewpoint of energy, the thermal fluctuations in a charge carrier's energy must be smaller than the energy range for the band of delocalized states. Reducing temperature reduces the magnitude of thermal fluctuations, keeping the charge carrier within the band of extended as desired for metallic behavior. Alternatively, metallic behavior can be considered the condition where the average mean free path of the charge carriers between collisions, $\lambda$, becomes larger than the periodic solid's lattice spacing. Lowering temperature reduces scattering by phonons, making $\lambda$ longer, thus favoring metallic conduction. For metallic behavior, a finite conductivity is predicted at absolute zero. In contrast, zero conductivity is expected for an insulator at absolute zero.

A **Zabrodskii plot ($W$ plot)** (Fig. 3.2a) reveals if the temperature dependence of electrical conductivity, $\sigma$, is characteristic of a metal, an insulator, or of the critical region [3, 16, 17]. This analysis defines $W$ as the dimensionless activation energy for charge carrier transport, where $W = (d \ln \sigma)/(d \ln T)$. On the plot of (ln $W$) versus (ln $T$), the slope will either be positive, zero, or negative, corresponding to the metallic, critical, and insulating behavior, respectively. Based on the Zabrodskii plot analysis, metallic behavior has been observed in several different conjugated polymers [16, 18, 19] and other disordered systems including CdSe quantum dot films [20] and metal-organic frameworks [21].

The critical region on the Zabrodskii, $W$, is independent of temperature. In this critical region, the conductivity displays a power-law dependence on temperature as given by

$$\sigma(T) \approx \left(\frac{4\pi^2 e^2 k_F}{\hbar}\right)\left(\frac{k_B T}{E_F}\right)^{\beta} = AT^{\beta} \tag{3.2}$$

where $A$ is a constant and $\frac{1}{3} < \beta < 1$.

The **Ioffe–Regel** criteria for metal–insulator (M–I) transition [22], expressed in terms of the Fermi wavenumber, $k_F$ as follows:

$$k_F\lambda = \left(3\pi^2 n_c\right)^{1/3}\lambda \sim 1 \tag{3.3}$$

In the insulating regime, all the states at the Fermi level are localized, and the electrical conductivity reaches zero as the temperature approaches absolute. Conversely, the metallic regime has delocalized states at the Fermi level and a finite electrical conductivity near absolute zero.

Schematic DOS diagrams for a p-type semicrystalline conjugated polymer are shown at low and high doping levels (Fig. 3.2b and c). Band broadening results from interchain coupling and Coulombic interactions between the charge carriers and the counterions. Both the band tails regions and the new band of states created by doping contain localized states. The location of $E_F$ determines the type of electronic behavior observed. If $E_F$ is located in a gap region, insulating behavior is observed. In disordered solids, $E_F$ can exist in an energy region populated with localized states. In this case, the electronic behavior is known as a Fermi glass insulator (Fig. 3.2b). At high doping levels (Fig. 3.2c), the bipolaron bands and the LUMO band (conduction band) can merge. From the perspective of band structure, semimetallic behavior exists if $E_F$ is located in a band of energies where the electronic [16] states are delocalized. For comparison, in a heavily doped p-type semicrystalline semiconductor (Fig. 3.2d), the Fermi energy lies at the acceptor level.

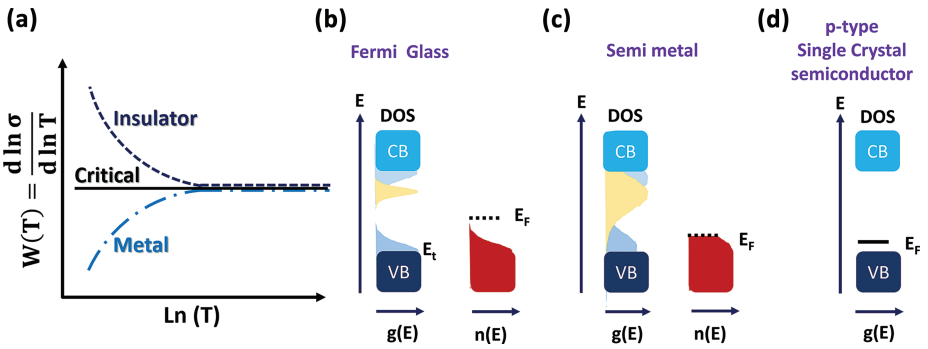


**Fig. 3.2:** (a) Zabrodskii plot (*W* plot) reveals the temperature-dependent conductivity of electronic transport behavior for an insulator, a metal, and the critical region. Density of states (DOS) diagram, *g*(E) and populated state diagrams, *n*(*E*) for (a) Fermi glass insulator, (c) semimetal, and (d) heavily doped p-type single crystal semiconductor. For (b) and (c), dark shaded regions indicated the extended states of the conduction band (CB, LUMO) and valence band (VB, HOMO). The light blue regions below the CB and above VB are the band tails of localized states. The yellow shaded regions indicated the new electronic states produced by doping.

## 3.3 Partial localization of extended states (Group I)

As opposed to considering charge carriers as being associated with a particular atom or molecule, solid-state physics allows for the possibility of a charge carrier being found anywhere in a crystalline solid. The corresponding electronic states are said to be fully extended. The electronic states become partially localized as disorder is introduced into the crystal. Partially localized states can extend over multiple atoms.

Electrical current results from motion of both positive and negative charge carriers. Applying an external electric field produces a drift current. Gradients in charge carrier density, such as those resulting from dopant concentration profiles, give rise to diffusion currents. The total current is the sum of the drift and diffusion currents.

**Drude theory** relies on classical mechanics [2, 3, 9, 23]. Indeed, the development of Drude theory predates quantum theory. In the Drude model, each charge carrier is considered to act independently, except for collisions. Thus, a charge carrier travels in a straight line until an instantaneous scattering event alters its direction. These assumptions parallel those for the kinetic theory of an ideal gas. Indeed, the ensemble of delocalized charge carriers considered in Drude theory is often referred to as a "gas". Charge neutrality is maintained by the lattice of immobile ions of the opposite charge.

The electric field accelerates charge carriers. Thus, the drift velocity is linearly proportional to $E$. The corresponding proportionality constant is known as the charge carrier mobility, $\mu$. The overall electrical conductivity, $\sigma$, of a material will depend on both $\mu$, and the density of charge carriers, $n_c$; and is proportional to the magnitude of the unit charge, $|e|$:

$$\sigma = |e| n_c \mu \tag{3.4}$$

Rather than reporting $\sigma$, as in commonly done in the conjugated polymer literature, the TCO literature frequently provides values of resistivity, $\rho$:

$$\rho = \frac{1}{\sigma} = \frac{1}{|e| n_c \mu} \tag{3.5}$$

Equations (3.4) and (3.5) show that electronic transport depends on both $\mu$ and $n_c$. The value of $\mu$ depends on the composition of the material and its nanostructure. For amorphous materials, $\mu$ is an isotropic property. However, in materials with structural anisotropy, $\mu$ will likely change with the direction of measurement. For a given material, the higher the concentration of defects, the lower the value of $\mu$. A decrease in $\mu$ occurs even for intentionally introduced defects, such as doping. With doping, $n_c$ increases, but to increase conductivity, the product $n^{\star}\mu$ must also increase.

**Charge carrier mobility**, $\mu$, in a bulk solid with homogeneous properties reflects contributions from individual components, $\mu_{i,}$ where the index i denotes a particular type of scattering event [24]. For each class, the rate of charge carrier

scattering is proportional to $1/\mu_i$. Considering the rates of scattering to be additive leads to **Matthiessen's rule**, which gives the overall scattering rate, $1/\mu$, as follows:

$$\frac{1}{\mu} = \frac{1}{\mu_{II}} + \frac{1}{\mu_{gb}} + \frac{1}{\mu_{ph}} + \frac{1}{\mu_N} + \frac{1}{\mu_{dis}} + \frac{1}{\mu_{other}} \tag{3.6}$$

The terms $\mu_{II}$, $\mu_{gb}$, $\mu_{ph}$, $\mu_N$, and $\mu_{dis}$ are individual components of mobility associated with ionized impurities (II), grain boundaries (gb), phonons (ph), neutrals (N), and dislocations (dis), respectively. Other sources of charge scattering include surfaces and interfaces, a mechanism that can become a significant source of charge carrier scattering as film thickness and nanostructure dimensions decrease [10].

In a particular situation, many of the $1/\mu_i$ terms will have negligible values, reducing the number of significant terms remaining in eq. (3.6). Each of the individual components $\mu_i$ has a unique functional dependence on parameters such as temperature, crystal size, and crystal lattice parameters.

The most straightforward situation is when a single type of scattering is dominant. In this case, the right-hand side of eq. (3.6) can be approximated as a single term. In this limit, $\mu$ equals the mobility value associated with the dominant scattering mechanism. A dominant mechanism has a high scattering rate, corresponding to a low value of mobility.

When a dominant mechanism exists, the description of electronic charge transport dramatically simplifies. Simplification is possible even for complex disorder materials, such as semicrystalline conjugated polymers. A series of samples having the same dominant scattering mechanism is highly desirable for developing meaningful trends based on structure–processing–property relationships. When such a trend is established, care should be taken not to assume the same trend for samples where different sources of scattering are significant.

**Dislocations** are significant as scattering centers in single crystals but typically play an insignificant role in more disordered materials. Thus, the term $1/\mu_{dis}$ in eq. (3.6) is typically neglected when applied to polycrystalline TCOs and semicrystalline conjugated polymers.

**Neutral scattering centers** at a concentration of $n_N$ have an associated mobility of $\mu_N$ given by

$$\mu_N = \frac{m^* e^3}{20\varepsilon_0 \varepsilon_r \hbar^3 n_N} \tag{3.7}$$

where the definition of the remaining variables and physical constants can be found in Tab. 1. Because the term $1/\mu_N$ typically has small magnitude relative to other terms in eq. (3.6), $1/\mu_N$ is often neglected when analyzing polycrystalline TCOs and semicrystalline conjugated polymers.

**Ionized impurities** most often result from the doping process, which also produces charge carriers. Thus, the charge carrier mobility due to the ionized scattering

centers, $\mu_I$, will depend on the doping level and determine the concentration of both the charge carriers, $n$, and ions, $n_I$. Charge neutrality can be maintained because the charge carriers and ionized scattering centers have charges of opposite sign. The integer $Z$ is the number of unit charges per scattering center. For an individual, singly ionized species, like $Cl^-$, $Z = 1$. For a multiply ionized species like $SO_4^{2-}$ or for a scattering center comprised of a cluster of ions, $Z > 1$.

**Brook–Herring–Dingle (BHD) theory** assumes that collision events with dopant counterions dominate charge carrier scattering. Indeed, for heavily doped inorganic semiconductors, including silicon and several TCOs such as ITO, AZO, indium oxide, gallium arsenide, tin oxide, and zinc tin oxide, BHD theory has been widely applied [9, 10, 25]. The ionized dopants decrease $\mu$, limiting the increase in $\sigma$ as the doping level is increased. Between collision events, the charge carriers experience Coulombic screening from the lattice ions. The BHD-derived charge carrier mobility due to the ionized scattering centers is given by

$$\mu_I = \frac{24\pi^3(\varepsilon_0\varepsilon_r)^2\hbar^3 n_c}{e^3 m^{*2} s(x) Z^2 n_I} \tag{3.8}$$

In addition to the variables and constants defined in Tab. 1, eq. (3.8) reveals that $\mu_I$ is inversely proportional to $s(x)$, which is the scattering function.. The definition for $s(x)$ is

$$s(x) = \ln\left(1 + \frac{4}{x}\right) - \left(\frac{1}{1 + \frac{x}{4}}\right) \tag{3.9}$$

where the dimensionless parameter $x$ is given by

$$x = \frac{e^2 m^*}{\pi\varepsilon_0\varepsilon_r\hbar^2\sqrt[3]{3\pi^5 n_c}} \tag{3.10}$$

When BHD theory applies, the overall mobility can be predicted with variation in the doping level, which produces $n_c$ and $n_I$. BHD theory also predicts that differences in dielectric constants, $\varepsilon_r$, and the effective mass of the electron, $m^*$, will impact mobility. By increasing Coulombic screening, higher values of $\varepsilon_r$ lead to increased $\mu_I$. Because organic films are primarily comprised of light atoms from the top of the periodic table having low electronic polarizability, $\varepsilon_r$ is typically low for organics. Because inorganic materials are comprised of heavier and more polarizable atoms, the corresponding values of $\varepsilon_r$ are typically higher than for organics. The shape of DOS functions, $g(E)$, of the conduction bands determines the value $m^*$ [9]. Lower $m^*$ corresponds to higher charge carrier velocities at a given kinetic energy, favoring increased $\mu_I$.

**Grain boundaries** play a critical role in the charge transport of polycrystalline inorganic materials. Impurity species, including dopants, often segregate to the grain boundaries. Both changes in crystallite orientation and composition at the

grain boundary result in a different potential energy, $V_{gb}$, in the grain boundary region.

Figure 2.3 schematically displays two structures for nanocrystallites in a conjugated polymer. These structures bear some analogy to the grain boundaries of a polycrystalline inorganic semiconductor. One difference is that an amorphous phase separates the polymeric nanocrystals. A second difference is that a macromolecule can act as a tie chain by incorporating in more than one nanocrystal. However, in both TCOs and conjugated polymers, the relative orientation of two crystallites, known as the tilt angle, is important in charge transport. Also, in both cases, a potential barrier to charge transport occurs between the two ordered domains.

**Seto's model** for inorganic materials with grain boundaries was derived starting from the consideration of thermionic emission [26]. Using the definitions supplied in Tab. 1, Seto's model expresses the mobility associated with scattering by grain boundaries, $\mu_{gb}$, as follows:

$$\mu_{gb} = e \times L \times (2\pi m^* k_B T)^{1/2} \times \exp\left(-\frac{eV_{gb}}{k_B T}\right) \tag{3.11}$$

Equation (3.11) shows that $\mu_{gb}$ depends linearly on the average grain boundary dimension $L$ and is strongly temperature dependent. The value of $V_{gb}$ is given by

$$V_{gb} = \frac{e}{8\varepsilon_0\varepsilon_r} \cdot \frac{Q_t^2}{N} \text{ when } LN > Q_t \tag{3.12}$$

or by

$$V_{gb} = \frac{e}{8\varepsilon_0\varepsilon_r} \times NL^2 \text{ when } LN < Q_t \tag{3.13}$$

In eqs. (3.12) and (3.13), $Q_t$ is the areal concentration of trapping defects at the grain boundary. $N$ is the charge carrier density in the grain, far away from the boundary region. Equation (3.12) represents the case of partial occupation of the interfacial trapping states, while eq. (3.13) represents the case of partial depletion of carriers in the crystallite. In both eqs. (3.12) and (3.13), higher values of $\varepsilon_r$ decrease the barrier height of the grain boundary region, favoring high values of mobility.

### 3.3.1 Interchain coupling due to π–π stacking

In ordered domains, the second highest value of charge carrier mobility, $\mu_{CC,}$ in conjugated polymers is along the direction of the π–π interchain stacking (Fig. 2.1d). The π–π stacking direction is orthogonal to the backbone.The magnitude of the interchain coupling depends on the distance separating the two chains, $x$. Along the π–π stacking distance, each chain's electronic wave function is assumed to have an exponentially decaying tail, with a characteristic decay length of $1/\Upsilon$.

The **interchain charge transfer integral**, $t_\perp$, can be expressed as

$$t_\perp = t_0 \exp(-\gamma x) \tag{3.14}$$

The pre-exponential factor $t_0$ is the value of the charge transfer integral at the minimum distance of separation [27].

The **Marcus–Hush theory** is a semiclassical model that relates the hopping rate, $k_{ij}$, between states localized on the chains $i$ and $j$ to the square of $t_\perp$ according to the relationship [28, 29]:

$$k_{ij} = \frac{{t_\perp}^2}{\hbar}\sqrt{\frac{\pi}{\beta k_B T}}\exp\left[-\frac{(\Delta E_{ij}+\lambda)^2}{4\beta k_B T}\right] \propto ({t_\perp}^2) \tag{3.15}$$

In addition to the variables defined in Tab. 1, $E_{ij}$ represents the difference in energy between states $i$ and $j$, and $\beta$ is the energy to molecular reorganization during the charge transfer event. The polymer conformational change upon the transition in electronic state results from the coupling between the lattice phonons and the electronic energy states in polaronic charge transport. Expression (3.15) for $k_{ij}$ can be used in the **Einstein equation** to arrive at a relationship for the charge carrier mobility due to chain-to-chain coupling, $\mu_{cc}$

$$\mu_{cc} = \frac{e}{k_B T}\left(\frac{1}{2n}\sum_i d_{ij}^2 k_{ij} P_{ij}\right) \propto ({t_\perp}^2) \tag{3.16}$$

where $i$ is an index that runs over all neighboring chains to chain $j$. The $d_{ij}$ is the distance to the $i$th neighbor, and $P_{ij}$ is the relative diffusional probability to the $i$th neighbor. The primary conclusion of this analysis is that $\mu_{cc}$ is proportional to ${t_\perp}^2$.

## 3.4 Partial delocalization of molecular orbitals (Group II)

The polymeric backbone in a crystallite is an inherent source of structural anisotropy. When the distribution of chains is nonrandom, property values can depend on the direction of measurement. The value along the backbone, $\mu_{IC}$, is likely higher for charge carrier mobility than in the orthogonal directions [30]. Because $\mu_{IC}$ has a high value, it is unlikely to be the limiting component for the semicrystalline polymer's overall mobility.

The conjugation length along a polymer will depend on its backbone conformation. Linear and rigid backbones tend to increase the extent of the conjugated regions. Any torsional change along the backbone disrupts the conjugation, breaking it into multiple subunits. Charge transfer between the conjugated subunits can occur by intra- and interchain hopping (Fig. 2.1a,b).

Interchain coupling increases the delocalization of the charge carriers. Without interchain coupling, the electronic states of linear conjugated chains are isolated and provide only 1D conduction pathways. As the coupling between chains occurs, 2D and 3D pathways for charge transport can form. The interchain coupling enhances the delocalization of the charge carriers. Greater delocalization can enable charge carriers to avoid disordered regions, such as the amorphous phase surrounding the nanocrystallites. Thus, interchain coupling tends to increase the charge carrier mobility.

More densely packed chains will have a higher degree of interchain coupling. For conjugated polymers, the density of packing depends on many factors, including, but not limited to, the synthesis method and the associated processing conditions, the doping level, the type of counterion, and the requirements of any postprocessing steps. The importance of the interchain separation distance has frequently been recognized in other organic conductors, such as the first organic superconductor, di(2,3,6,7-tetramethyl-1,4,5,8-tetraselenafulvalenium) hexafluorophosphate). When subjected to an external pressure of 11 kbar, the interchain distance decreases, increasing the interchain couplings and current flow in the organic superconductor.

### 3.4.1 Variable range hopping (VRH)

For higher levels of disorder, mobile charge carrier transport is often represented as a quantum mechanical "hop" from one localized state to another or the release of charges from trap states into the extended band (Fig. 1.3c). The hop will occur between an initial occupied state, *i*, and an empty state, *j*. The probability of hopping, $P_{ij}$, will depend on both the hopping distance, $L$, and the energy barrier, $\Delta E_{ij}$ between states *i* and *j*. When the thermal energy, $k_B T$ is high relative to $\Delta E$, hopping between nearest neighbors is the most probable event. Conversely, at low $k_B T$, hopping between similar energy states dominates, independent of the states' physical location.

The **Miller–Abrahams model** considers that $P_{ij}$ will have contributions from a tunneling factor and a Boltzmann factor [3, 5, 31] expressed as

$$P_{ij} \propto \exp\left\{\frac{-2L}{\xi_0} - \frac{\Delta E_{ij}}{k_B T}\right\} \tag{3.17}$$

where $\xi_0$ is the localization length as zero magnetic field. In the high-temperature limit, the Boltzmann factor will dominate. This model predicts the same probability for both directions of hopping (i.e., $P_{ij} = P_{ji}$). An underlying assumption of the Miller–Abraham model is a weak coupling between the charge carriers and the lattice phonons. This assumption has been questioned for solitons, polarons, and bipolarons representing charge carriers coupled to the lattice phonons. Alternative hopping models have been proposed and tested for their ability to predict trends in mobility as a function of electric field, temperature, and magnetic field [13].

**Mott's variable range hopping (VRH) theory** considers a network of states where the Miller–Abrahams model describes each hop [32, 33]. At high temperatures, hopping conduction is dominated by short-range events. At reduced temperatures, the probability of hopping between two localized states very close to the Fermi energy becomes more probable, even when long-range hopping is required. Thus, the average hopping distance increases as the temperature is reduced. Mott's law gives the associated temperature-dependent electrical conductivity:

$$\sigma_{\text{Mott}}\ (T) = \sigma_0 \exp\left[-\left(\frac{T_{\text{M}}}{T}\right)^{1/1+d}\right] \tag{3.18}$$

where $\sigma_0$ is an exponential prefactor. The exponent inside the exponential contains the integer, $d$, is known as the dimension factor. In a bulk solid with 3D conduction pathways, $d = 3$. At nanoscale thicknesses, 2D conduction ($d = 2$) can arise in thin films. Isolated conjugated polymer chains or nanowires can be considered as 1D conduction pathways ($d = 1$) [34].

The Mott's transitions temperature, $T_{\text{M}}$, is related to the DOS at the Fermi level, $g(E_{\text{F}})$, and the localization length at zero magnetic field $\xi_0$ is given as

$$T_{\text{M}} = \frac{\beta}{k_{\text{B}}\ g(E_f)\ \xi_0^d} \tag{3.19}$$

where $\beta$ is a proportionality constant. Both $\sigma_0$ and $T_{\text{M}}$ generally have only a weak dependence on temperature, in which case, eq. (3.15) can be restated as

$$\sigma_{\text{Mott}}\ (T) = \sigma_0 \exp\left[-\left(\frac{E_a}{k_{\text{b}}T}\right)^{1/1+d}\right] \tag{3.20}$$

where $E_{\text{a}}$ is the activation energy associated with thermally activated conduction by VRH hopping. Thus, for 3D conduction, ln $\sigma_{\text{VRH}}$ is expected to have a $T^{-1/4}$ dependence. For the same material, if $\sigma_0$ and $E_{\text{a}}$ remain fixed while the film thickness or nanostructure dimensions decrease to the point where the conduction pathways are no longer 3D, $d$ is lowered and thus $\sigma_{\text{Mott}}\ (T)$ increases.

The mean free path, $\lambda$, of the charge carrier in a 3D solid can be calculated using the formula [35]

$$\lambda = \frac{\pi\hbar}{e}\left(\frac{3n_{\text{c}}}{\pi}\right)^{1/3}\mu \tag{3.21}$$

Mott's law was derived by assuming that the hopping energy exceeds the Coulombic interactions between localized charge carriers. Hopping energy decreases as the temperature is reduced. Thus, at extremely low temperatures, typically <10 K, the Coulombic interactions may become significant relative to the hopping energy. Near absolute zero, a soft gap opens due to the Coulombic interactions. This soft gap is

accounted for by the **Efros–Shklovskii (ES)-VRH model** [36, 37], which gives the following expression:

$$\sigma_{\mathrm{ES}}\ (T) = \sigma_{0,\,\mathrm{ES}} \exp\left[ -\left(\frac{T_{\mathrm{ES}}}{T}\right)^{1/2}\right] \tag{3.22}$$

where $\sigma_{0,\,\mathrm{ES}}$ is a dimensionless amplitude. The characteristic temperature, $T_{\mathrm{ES}}$, associated with the ES-VRH model is given by

$$T_{\mathrm{ES}} = \frac{\beta\ e^2}{\varepsilon_{\mathrm{r}}\ k_{\mathrm{B}}\ \xi_0} \tag{3.23}$$

where $\beta$ is a numerical constant that depends on the dimensionality of conduction. For 3D conduction, $\beta = 2.8$.

A linear combination of $\sigma_{\mathrm{Mott}}$ and $\sigma_{\mathrm{ES}}$ can be used as empirical fit for the observed trends in resistivity with temperature:

$$\frac{\rho(T)}{\rho(300\,\mathrm{K})} = \left[\sigma_{\mathrm{Mott}}(T) + \sigma_{\mathrm{ES}}\ (T)\right]^{-1} \tag{3.24}$$

where the ratio $\sigma_{\mathrm{Mott}}\ (T)/\sigma_{\mathrm{ES}}\ (T)$ increases as the temperature increases. The interchain coupling due to the π–π stacking distance is significant for this group of conjugated conducting polymers, as discussed earlier in Section 3.3.1.

### 3.4.2 Additional hopping conduction models

**GDM** is an analytic model which assumes that a band can be represented as a Gaussian distribution of states (eq. (3.1)) and that hopping conduction occurs among these states [12, 13]. The GDM has been applied to a wide range of organic conductors [38] and can predict how conductivity will vary under various circumstances. The GDM has predicted the temperature dependence of mobility as $\ln(\mu)\ \alpha\ T^{-2}$. In the limit of high carrier concentration, the GDM model simplifies and predicts, $\ln(\mu)\ \alpha\ T^{-1}$, which corresponds to Arrhenius behavior which is expressed as

$$\sigma = \sigma_0 \exp\left( -\frac{E_{\mathrm{a}}}{k_{\mathrm{B}}\ T}\right) \tag{3.25}$$

where $E_{\mathrm{a}}$ is the activation energy and $\sigma_0$ is the prefactor that is weakly dependent on temperature and customarily taken as a constant.

**Multiple trapping and release** is a charge transport mechanism hypothesized for charge carriers in shallow traps [6]. The charge carrier hopping between shallow traps and their release back into the lower energy extended states is modeled as a thermally activated process. This electrical transport model, which contemplates the combination of extended states and trapping states, has been developed and

applied to conjugated polymers with ionized impurities. The conductivity depends on the energy of the charge carrier, $E$. The conductivity has a power-law dependence when $E$ is above the critical value, known as the transport edge energy $E_t$, and zero below it, as stated explicitly by the pair of following equations:

$$\sigma(E,T) = \sigma_{E_0}(T) \times \left(\frac{E - E_t}{k_b T}\right)^s, \ E \geq E_t \tag{3.26}$$

and

$$\sigma(E) = 0, \ E < E_t \tag{3.27}$$

where $\sigma_{E_0}(T)$ is temperature dependent, and $s$ is an integer that depends on the type of charge carrier transport. For transport at the mobility edge (i.e., at the metal–insulator transition), $s = 0$. For a typical 3D solid, $s = 1$, while for a solid with ionized impurities, $s = 3$.

## 3.5 Partial delocalization due to ordered domains (Group III)

The spatial disorder of the semicrystalline nature of conjugated polymers has been explicitly incorporated into various charge transport models, which are classified here as Group III. The chains are densely packed in an ordered fashion within the ordered nanocrystals, and the charge carriers are delocalized over the "grain." In the disordered amorphous region surrounding the grains, lower packing density and lack of long-range order lead to localization of the charge carriers.

Interestingly, a correlation between average crystallite size and conductivity is found in some experimental studies but not others. If delocalization has exceeded the crystallite's dimensions, the use of Group I models is likely appropriate. For Group I models, charge transport is predicted to be independent of local structure details, such as the crystallite size. However, for a more localized charge carrier, the conductivity would indeed be expected to depend on crystallite size, as expected from Group III models.

**Effective mobility**, $\mu_{eff}$, for a semicrystalline or polycrystalline solid can be modeled as multiple resistances in series along the direction of measurement. The crystallites will have a mobility, $\mu_c$, and average dimension, $L_c$. The corresponding properties in the grain boundary regions are $\mu_{gb}$ and $L_{gb}$. The resulting expression is

$$\frac{L_c + L_{gb}}{\mu_{eff}} = \frac{L_c}{\mu_c} + \frac{L_{gb}}{\mu_{gb}} \tag{3.28}$$

Note that eq. (3.28) describes a solid having two distinct regions and thus differs from eq. (3.6), which considers the solid as a single homogeneous phase (Group I models). If a high degree of disorder is present in the grain boundary region, the resulting electronic trap states will reduce $\mu_{gb}$. When $\mu_{gb}$ is much lower than $\mu_c$, optimizing $\mu_{gb}$ is critically important for improving $\mu_{eff}$.

**Coarse-grained VRH** models are extensions of the original theories of hopping conduction developed for localized atomic or molecular orbitals (Section 3.4.1). In the coarse-grained approach, the wave functions are delocalized over the ordered "grain" [39]. The wave functions have a limited extent into the surrounding amorphous region. Applying VRH theories to the partially delocalized states associated with the grains leads to the coarse-grained models. The overlap of wave functions between a pair of grains gives rise to intercrystallite hopping conduction. The extent of the wave function for an individual nanocrystal will depend on its dimensions and the degree of interchain overlap due to π–π stacking. The rate of charge transport between grains will depend on the overlap of their wave functions. The magnitude of overlap will depend on the extent of wave functions for each nanocrystal and the distance that separates them. The set equations describing coarse-grained VRH are identical to those used for the original VRH model (Section 3.4.1). As compared to the original VRH models, the coarse-grained results are interpreted in terms of the delocalized wave functions associated with the grains.

**Fluctuation-induced tunneling (FIT)** is another model that describes the charge between metallic domains separated by insulating junctions [40]. These junctions represent energy barriers of area $A$, having a height $v$ and a width $w$. In Section 3.2, a similar concept of an energy barrier between ordered regions was used in Seto's model for polycrystalline materials. Temperature fluctuations influence the rate of charge transfer across the gaps. The FIT model results in the following expression for electrical conductivity:

$$\sigma_{FIT}\ (T) = \sigma_{0,FIT} \exp\left[ - \frac{T_1}{T + T_0} \right] \tag{3.29}$$

where $\sigma_{0,FIT}$ is constant for a given film. At temperature $T_1$, the average kinetic energy of the charge carrier is equal to the energy required to classically overcome the barrier, leading to the relationship:

$$T_1 = \frac{8\varepsilon_0}{e^2 k_B} \left( \frac{Av^2}{w} \right) \tag{3.30}$$

Below temperature $T_0$, elastic tunneling dominates the charge transport across the junction, giving the expression:

$$T_0 = \frac{16\varepsilon_0 \hbar}{\pi e^2 k_B \sqrt{2m^*}} \left( \frac{Av^{3/2}}{w^2} \right) \tag{3.31}$$

## 3.6 Intercrystallite hopping and tie chains

The intercrystallite junctions play a critical role in the electronic transport behavior of semicrystalline conducting polymers. Some of the chains in conjugated polymers have been proposed to connect directly from one nanocrystal to another. In such a tie chain, a linear conformation allows for conjugation that provides an efficient bridge for charge transport across the amorphous phase. Tie chains with nonlinear conformations are less efficient for intercrystallite charge conduction [41]. Distortion, bending, and twisting of the polymer chain results in the localization of the charge carrier. Indeed, conformational changes along the backbone can lead to shallow and deep trapping states.

The concentration of tie chains will be determined by synthesis and postprocessing conditions, increasing chain length, and decreasing intercrystallite spaces. Increasing the molecular weight of the polymer creates longer tie chains. The separation between two crystallites depends both on the degree of crystallinity and distribution of crystallite sizes.

The probability of forming linear tie chains will increase for polymers with rigid backbone structures and higher degrees of regioregularity. Such polymers will have a higher propensity to crystallize. The persistence length describes the average distance over which a macromolecular chain remains linear and is correlated with the polymer's mechanical stiffness. Rapid charge transport through a percolation network of tie chains is thought to be possible when the persistence length exceeds the intercrystallite spacing.

The constraint of having a linear tie chain is more readily achieved when the crystallites being connected have a similar orientation (Fig. 1.1). The correlation of crystallite orientations depends on nanotexture. Pure face-on orientation increases the probability that linear tie chains will form intercrystallite connections that lead to enhanced in-plane conductivity. The high degree of misorientation between adjacent grains occurs when there is a mixed texture of face-on and edge-on orientations. A mixed texture decreases the occurrence of linear tie chains. At physical dimensions approaching the size of the nanocrystals, interfacial energies are likely to influence nanotexture development. Thus, 1D or 2D confinement represents an additional means for controlling the orientational distribution between pairs of crystallites.

Analogous effects of nanotexture have long been known in polycrystalline inorganic solids. In these materials, the alignment of crystallite orientations is also favorable for enhancing the electrical conductivity. Adjacent crystallites with similar orientations are described as low-angle grain boundaries (Fig. 2.3). Poor intercrystallite connectivity occurs at high-tilt angle grain boundaries, resulting in electrically isolated grains. Thus, a larger energy barrier for intercrystallite transport was proposed by Kang–Snyder [23] according to the following equation:

$$\sigma(T) \propto \exp\left[-\left(\frac{W_\gamma}{k_b T}\right)^{\frac{1}{2}}\right] \tag{3.32}$$

where $\sigma(T)$ is the electrical conductivity as a function of temperature, and $W_\gamma$ is the energy barrier of intercrystallite charge transport. This model will be discussed further in Section 6.2.3.2.

Intercrystallite charge transport mechanisms occur in parallel. Thus, the components of intercrystallite mobility due to hopping and tie chain bridges will be added. When mobility due to bridging conducting is much higher, the contribution from intercrystallite hopping can be neglected.

## 3.7 Comparing interchain and intercrystal carrier mobility

The spatial localization of disorder can be formulated starting from molecular orbitals associated with polymer chains (Group II) or the confinement of crystallite wave functions by the amorphous domains (Group III). For Group II models, the rate-limiting step is often interchain charge transport due to π–π stacking interactions (Section 3.1.1). From this viewpoint, the π–π stacking distance is the critical parameter. The rate-limiting step for Group III models is intercrystallite transport, which is improved with increasing alignment between pairs of crystallites (Section 3.6).

Group II and Group III models are the limiting cases for interchain and intercrystallite charge transport. Figure 3.3a shows a schematic of interchain and intercrystallite processes occurring in series. The intercrystallite rate will increase with increasing crystallite order and orientation (Fig. 3.3b). The interchain rate will be far less sensitive to crystallite order and orientation but will depend on the π–π stacking distance. A small π–π stacking distance will lead to a higher interchain rate. For processes occurring in series, the slowest step limits the overall rate.

Figure 3.3c shows the overall rate for the cases of small and large π–π stacking distances. At a low degree of order, the intercrystallite charge transfer is rate limiting. This behavior corresponds to the Group III limit, where conductivity increase with improved order but is insensitive to the π–π stacking distances. Once a threshold degree of order has been achieved, the rate limitation transitions to the intrachain process, corresponding to the Group II limit. Once sufficient order has been achieved, no further gains in conductivity will be made by further improving the order, as can be seen by the plateaus in Fig. 3.3c. When the π–π stacking distance is large, the transition to the Group II limit occurs at a modest degree of order. The plateau is at a moderate value of conductivity. For a small π–π stacking distance, a higher degree of order must be achieved to reach the Group II limit, and the plateau will occur at a larger value of conductivity. In summary, to reach high conductivity, select a polymer with low π–π stacking distance and improve the nanotexture to a

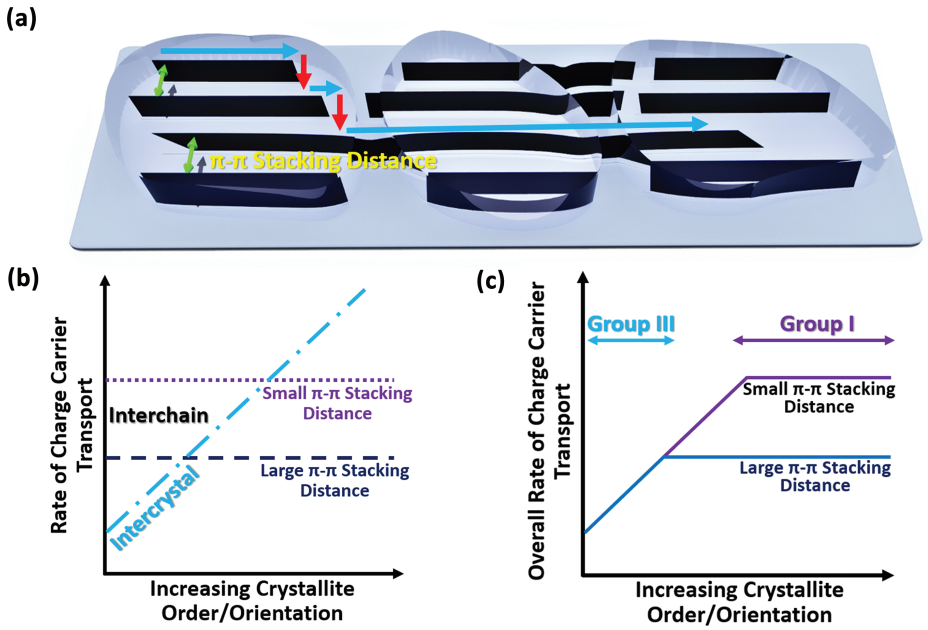


**Fig. 3.3:** (a) Schematic of lamella and oriented crystallites, showing intrachain (blue arrows) and interchain (red arrows) transport steps occurring in series, with a linear tie chain providing rapid intercrystallite transport. (b) Rates for interchain transport rate for two different π–π stacking distances and the intercrystallite rate, which improves as more linear tie chains form with increased order and orientation. (c) The overall charge transport rates. At a low degree of order and orientation, the intercrystal transport is the slow step, and the overall rate is improved by increasing order and orientation (Group III models). Once a sufficient degree of order and orientation is reached, the rate plateaus, indicating that the interchain transport becomes rate limiting (Group I models). Adapted with permission from Heydari Gharahcheshmeh M and Gleason KK, Mater. Today, Adv., 8, 10008 (2020) Copywrite 2020, Elsevier.

point where it no longer limits conductivity. Crystallinity is not essential for high charge carrier mobility in conjugated polymers (Section 4.5).

## 3.8 Electronic transport models and λ

Insight into the extent of spatial averaging due to charge carrier transport can be gained by estimating the mean free path of charge carrier, $\lambda$, using eq. (3.8). The calculation requires independent knowledge of the charge carrier mobility, $\mu$, and charge carrier density, $n_c$, which are less frequently measured than the overall conductivity value. Inorganic semiconductors, such as amorphous and polycrystalline silicon and polycrystalline TCOs, have $\lambda \sim 1$–$50$ μm [42]. Larger $\lambda$ is a measure of increased order and orientation.

### 3.8.1 Small $\lambda$

The $\lambda$ ranges from only ~$10^{-5}$ to $10^{-4}$ nm in undoped poly(thiophene) [42]. Bulk conjugated polymers with small $\lambda$ are expected to follow 3D VRH conduction (eq. (3.20), with $d = 3$). Temperature-dependent experiments that reveal a correlation between $\ln \sigma$ and $T^{-1/4}$ allow the activation energy, $E_a$, for the hopping to be determined (eq. (3.20)). A few examples of conjugated polymers displaying 3D VRH transport along with their corresponding $E_a$ values are listed as follows:

- poly(thiophene), 48 meV [42];
- poly(3-hexylthiophene) (P3HT), 80–280 meV [43, 44]; and
- poly(aniline), 22–29 meV [45, 46].

### 3.8.2 Large $\lambda$

To avoid grain boundary scattering, single-crystal poly(3,4-ethylenedioxythiophene) (PEDOT):Cl nanowires were nanotemplated by VPP [47]. The nanowires had cross-sectional dimensions of 95 nm × 100 nm and displayed an average conductivity of 7619 S/cm, achieving a high value of 8797 S/cm. The single-crystal nature of the PEDOT was confirmed by selective-area electron diffraction, which gave lattice parameters of $a = 1.101$ nm, $b = 0.464$ nm, and $c = 0.791$ nm. The values for both $a$ and $b$ were smaller than typically reported. The observed tight packing of the chains was hypothesized to result from the combined effects of nanoconfinement and the small counterion used. The $b$-axis was parallel to the nanowire axis, and the $c$-axis was parallel to the substrate, representing an edge-on orientation (Fig. 2.2b). The estimated doping level was 10% of the monomer units ($n_c \sim 0.6 \times 10^{21}$ cm$^{-3}$). From eq. (3.4), the calculated mobility was 88.08 cm$^2$/Vs. Applying eq. (3.21) gives a corresponding value for $\lambda$ of ~27 nm.

In some cases, doped semicrystalline PEDOT can have $\lambda > 1$ nm [48]. For example, PEDOT:Br film 10 nm thick [49], with a conductivity of 6259 S/cm, had measured values of $n_c \sim 2.1 \times 10^{21}$ cm$^{-3}$ and $\mu = 18.45$ cm$^2$/Vs. The resulting $\lambda$ of ~9 nm far exceeds the mean crystallite size of ~3.2 nm. This spatial averaging is compatible with the GDM (Section 3.4.2) or its Group II variants. For example, the transport behavior of the specific PEDOT example in this paragraph was analyzed by the Kang–Snyder model [23, 50], as will be discussed further in Section 6.2.3.2.

Each doping event in a conjugated polymer produces one charge carrier and one counterion (Section 1.3). Thus, increasing the doping level increases both the charge carrier density, $n_c$, and scattering by ionized impurities (Section 3.3). At high levels of doping, the counterions represent the dominant source of charge carrier scattering [50]. A higher scattering rate lowers charge carrier mobility, $\mu$. Since electrical conductivity, $\sigma$, is proportional to both $n_c$ and $\sigma$ (eq. (3.4)), there is an optimal doping level which maximizes $\sigma$. At low levels of doping, the mobility is high, but

the charge carrier density is low. Conversely, at high doping levels, $n_c$ is high but $\mu$ is low.

The BHD model (Section 3.3) has been applied to both PEDOT:Br [50] and PEDOT:Tos [51]. In this Group I model, the charge carriers are considered to be a "gas," which is independent of any particular lattice site. Consistent with this composition-independent assumption, the maximum isotropic conductivity is observed at $n_c \sim 2 \times 10^{21}$ cm$^{-3}$ for both ITO and PEDOT. However, at this optimum, the $\mu$ for ITO is ~10× higher than for PEDOT due to the differences in their dielectric constants, $\epsilon_r$, and effective masses, $m^*$ (eq. (3.8)). This BHD analysis suggests that $n_c \sim 2 \times 10^{21}$ cm$^{-3}$ will be the optimal doping level for other highly doped conjugated polymers and that value electrical conductivity achieved can be engineered through $\epsilon_r$ and $m^*$.

The full range of doping for conjugated polymers from 0% to 100% has been followed by electrochemical measurement (Section 5.1), where the maximum ionic conductivity is often observed at doping levels of ~50% [55]. Carrier densities corresponding to oxidation levels of >90% have also been observed for PEDOT:Br and PEDOT:Cl [35, 50]. In PEDOT:Tos/$ClO_4^-$, doping levels >50% have been reported, and computations suggest that some counterions can intercalate into the π–π stacking structure [53]. In these studies, the oxidation levels are much higher than the often quoted limit of 33% of the monomer units of PEDOT units being oxidized [54]. Rather than being a limit, the 33% doping level may correspond to the level for optimal conductivity. The $n_c$ for maximum conductivity of PEDOT, given in the preceding paragraph, corresponds to the ionization of ~1 out of ~3 monomer units. Higher doping levels increase $n_c$, but lower $\mu$ as the dopant counterions increase the rate of ionized impurity scattering (eq. (3.8)). Lowering $n_c$ increases $\mu$. For example, a charge carrier mobility of 33.6 cm$^2$/Vs was measured in PEDOT:Br for $n = 1.8 \times 10^{20}$ cm$^{-3}$ [50].

For mechanically strained PEDOT:PSS (poly(styrene sulfone)) microfibers of ~10 μm diameter, electrical transport becomes anisotropic with a mobility of 12.9 cm$^2$/Vs measured along the fiber axis [52]. The carrier density was $5.8 \times 10^{20}$ cm$^{-3}$, which corresponds to nearly full oxidation of the PEDOT. Carrier densities $>6 \times 10^{21}$ cm$^{-3}$ were also reported for PEDOT:PSS after treatment in sulfuric acid [52] with a corresponding mobility of ~4 cm$^2$/Vs.

### 3.8.3 Intermediate $\lambda$

The details of the spatial disorder in semicrystalline polymers become important when $\lambda$ is comparable to the mean crystallite size. Examples that include spatial inhomogeneity based on the ordered and disordered domains (i.e., Group III models) are discussed below for PEDOT doped with $Br^-$, PSS, or $HSO_4^-$ and having preferential texture.

**Coarse-grained VRH transport** (Section 3.5) was observed in preferentially edge-on and face-on textured PEDOT:Br films. The models quantitatively predicted

the electrical conductivity from 300 K down to <10 K. The coarse-grained wave functions are delocalized over the ordered lattice sites of the individual nanocrystals. The wave functions have a limited extent in the surrounding amorphous PEDOT domain. Charge transport is the result of the overlap of the wave functions from adjacent grains.

High-angle annual dark-field scanning transmission electron micrographs (TEM) revealed the nanoscale dimensions of ordered and disordered domains. The edge-on oriented films had a mean crystallite size of 5.5 nm, larger than the 3 nm value for the face-on oriented films. Despite their larger crystallites, the edge-on films had lower room-temperature in-plane conductivity than the face-on films.

For film thicknesses >10 nm and <80 nm, a linear combination of the 3D ($d = 3$) Mott's and ES-VRH coarse-grained models (eq. (3.24)) accurately predicted the temperature-dependent conductivity. For films <10 nm thick, Mott's 2D ($d = 2$) model (eq. (3.18)) was applied. The 2D conduction is indicative of the film thickness becoming comparable to the crystallite size. Because the ES correction was not needed for the thinner films, these films were hypothesized to possess a higher degree of spatial order than their thicker counterparts. The highest room-temperature in-plane conductivities were found in films <10 nm thick, where a maximum value of 2000 S/cm was reached. The higher conductivity of the thinner PEDOT layer is in contrast to the behavior of inorganic films. For the inorganics, the increased interfacial charge carrier scattering in thinner films lowers their conductivity.

**Coarse-grained 3D VRH transport** has also been observed for in-plane conductivity measurement of PEDOT:PSS. The morphology of PEDOT:PSS leads to anisotropic electronic transport. Based on the temperature-dependent and electric field-dependent electrical conductivity measurement of PEDOT:PSS, the in-plane 3D coarse-grained VRH process was modeled to occur between flattened quasimetallic PEDOT particles separated by insulating PEDOT:PSS [56, 57]. The expected dependence ln $\sigma$ on $T^{-1/4}$ was observed, and the lateral grain size was estimated to be 20–30 nm. In the perpendicular direction, the conductivity was up to 1000× lower, hypothesized to result from thicker insulating PSS layers.

Using high-field magnetoconductance measurements, 2D electronic transport was observed in PEDOT:PSS treated with ethylene glycol but not seen in pristine PEDOT:PSS [58]. The ethylene glycol treatment was hypothesized to cause the phase segregation of the PEDOT and the PSS into lamellar layers parallel to the film's surface. The laminated structure had a period of 3.0 nm in the free-standing film of ~5 μm overall thickness. Within the PEDOT layers, the horizontal mean free path for transport was estimated as ~30 nm. GIWAXS (grazing-incidence wide-angle X-ray scattering) analysis revealed that face-on oriented PEDOT nanocrystals with a π–π stacking distance of 0.343 nm. The dielectric PSS remained amorphous. Conduction perpendicular to the substrates occurred by hopping across the PSS domains between the 2D PEDOT states. The room-temperature in-plane conductivity was 714 S/cm.

**Inhomogeneous quasi-1D electronic transport** was modeled by Gueye et al. for PEDOT films having in-plane room conductivity values between 1200 and 5400 S/cm [59]. The films were ~10–40 nm thick. The in situ polymerization of the PEDOT utilized the oxidant $Fe(CF_3SO_3^-)_3$, resulting in $CF_3SO_3^-$ counterions. Dopant exchange to $HSO_4^-$ was achieved by rinsing in sulfuric acid. A posttreatment using both acid rinsing and solvent exposure gave the highest conductivity. In this film, the crystallite size was ~7 nm (>20 monomeric units), and the oxidation level was ~39%. High-resolution TEMs (HRTEMs) confirmed that the amorphous domain surrounded the nanocrystallites. The HRTEMs also clearly showed the periodic structure inside the nanocrystallite. For the sulfuric acid–rinsed, solvent-treated film, a π–π stacking distance of 0.346 nm was determined by both HRTEM and GIWAXS, and the GIWAXS also confirmed the face-on preferential texture.

The temperature-dependent electrical conductivity behavior from room temperature down to 3 K was measured and modeled. At low temperature, a positive slope of $W$ was observed (Section 3.2), consistent with metallic-like conduction. The electronic transport model included the spatial heterogeneity of the semicrystalline PEDOT. Specifically, the ordered and disordered regions were considered to alternate along a single direction, corresponding to a quasi-1D structure. Metallic conductivity was assumed in the nanocrystals. In the intervening amorphous regions, **FIT** (Section 3.5) was assumed to occur in parallel with disordered metallic conduction. Excellent agreement between the model and data was achieved over the entire temperature range for the as-grown and three differently post-treated PEDOT films. The model predicted that the conductivity inside the nanocrystallites ranged between 37,224 and 81,187 S/cm in all four films. Thus, the lower conductivity in the amorphous PEDOT domain dominates the overall conductivity of the semicrystalline films.

## 3.9 Electronic transport and π–π stacking distance

When the rate of intercrystallite charge carrier mobility is high, the conductivity is no longer dependent on crystal size (Fig. 3.3c). Charge transport between crystallites is schematically shown along a tie chain in Fig. 3.3a. Intercrystallite charge transport through tie chains will occur in parallel with hopping conduction across the amorphous regions. The intercrystallite hopping rate can be described by either a coarse-grained VRH or FIT model (Section 3.5). As order increases, the sum of the intercrystallite rates (e.g., tie chain and intercrystal hopping) can exceed the interchain transport rate (Fig. 3.3b). Tie chains between crystallites improve intercrystallite transport [7]. Tie chains must be of sufficient molecular weight to bridge between crystallites. Conjugation breaks along the tie chain are less frequent when the chains connect the crystallites with the same orientation. The probability of having similarly aligned nanocrystals in thin films is highest for face-on preferential texture (Fig. 1.1). Indeed, the energy barrier to in-plane charge carrier transport for PEDOT is two to

three orders of magnitude lower for face-on than edge-on preferential orientation [61]. In the face-on orientation, $W_Y$ (eq. (3.32)) is <1 meV.

The interchain charge transport rate depends on the π–π stacking distance. When interchain charge transport dominants the overall transport rate, the maximum level of conductivity is expected to increase as the π–π stacking distance becomes smaller (Fig. 3.3c). Computational models have also concluded that effective π–π stacking is essential for achieving high conductivity [60]. In PEDOT, the π–π stacking distance equals $b/2$, half of the $b$-axis lattice parameter (Section 2.4).

Interchain coupling in quasimetallic PEDOT grains was critical for achieving high conductivity in PEDOT:PSS [62]. The X-ray diffraction measured π–π stacking distance of pristine PEDOT:PSS of 0.350 nm dropped to 0.341 nm after treatment in the solvent dimethyl sulfoxide (DMSO). The DMSO treatment caused little change in the PSS content but increased the in-plane room-temperature conductivity to 660 S/cm, a dramatic change from the 2 S/cm value of the pristine material. Using GIWAXS, the results for pristine and DMSO-treated PEDOT:PSS have been confirmed, and data for other solvent-treated PEDOT:PSS layers have been reported [63]. For PEDOT:PSS materials, a general correlation was observed between decreased π–π stacking distance and ln $\sigma$. The postprocessing treatments can also alter the morphology of the PEDOT:PSS polymer chains [64]. Both the charge carrier density and charge carrier mobility increase upon the formation of crystalline and fibrillary microstructure [52].

Decreased π–π stacking distance also correlates with increased in-plane conductivity for a series of face-on-oriented PEDOT:Cl films [65, 66]. All the films had a mean crystallite size of ~3 nm. Using systematic changes in the oxidative chemical vapor deposition growth conditions, the π–π stacking distance was reduced from 0.350 nm down to 0.343 nm [66]. A corresponding increase of more than tenfold was observed in the conductivity, and a maximum value of 7420 S/cm was reached. The observed correlation was considered in terms of the charge transfer integral (eq. (3.14)) and tie chains (Fig. 3.3a). Both the $a$-axis and $b$-axis lattice parameters decreased at lower levels of incorporation of the $Cl^-$ counterion [65].

A conductivity of 6259 S/cm was previously reported for face-on-oriented PEDOT:Br with a π–π stacking distance of 0.340 nm [61]. Thus, for PSS, $Cl^-$, and $Br^-$, high levels of conductivity are achieved as the π–π stacking distance is lowered to a value of ~0.34 nm.

## 3.10 Measuring electrical transport properties

The electrical conductivity of a conjugated polymer thin film is most commonly measured in the plane of the substrate but through-plane measurements have also been reported. The in-plane value depends on both sheet resistance, $R_s$, and film thickness, $t$, as shown in the following expression:

$$\sigma = \frac{1}{(R_s t)} \tag{3.33}$$

Using a four-point probe, current, $I$, is measured in response to an applied voltage, $V$, and giving $R_s = 4.5324\ V/I$. The units of $R_s$ are ohms per square and indicate that this same value of resistance will be measured for a square of any size. Using a four-point rather than a two-point measurement reduces the error associated with the resistance in contacting the film. The factor of $\pi/\ln 2 \sim 4.532$ arises from the linear geometry of four equidistant contacting points, and a film is considered to be an infinite plane with a thickness approaching zero [2]. Care must be taken to understand if the value read out by the four-point probe instrument has already taken the factor of 4.532 into account or not. For room-temperature measurements, the four probes typically directly contact a blanket polymer layer. For resistivity measurements as a function of temperature, pressure, magnetic field (**Hall effect**), or another external parameter, it is preferable to make electrical contact to the polymer film using a patterned metal layer to form a two-terminal [67] or a **van der Pauw** device.

The methods typically used to measure thickness include profilometry, microscopy, and ellipsometry. Because of the inverse relationship between $\sigma$ at $t$, at low thickness, a small uncertainty in $t$ corresponds to a large uncertainty in $\sigma$ [68]. The accurate determination of film thickness is a significant consideration for profilometry measurement on soft conducting polymer films, which can suffer mechanical deformation when physically contacted. Hall effect measurements can be used to obtain charge carrier mobility and concentrations [48]. Alternatively, these properties can be extracted from device models of the performance of thin-film transistors (TFTs) fabricated with the conjugated polymer of interest [69].

## References


[1] Bässler H. Charge transport in disordered organic photoconductors a Monte Carlo simulation study. Phys Status Solidi 1993, 175, 15–56.

[2] Kim N, Petsagkourakis I, Chen S, et al. Electric Transport Properties in PEDOT Thin Films from: Conjugated Polymers, Properties, Processing, and Applications. CRC Press, 2019, p. 45.

[3] Heydari Gharahcheshmeh M, Gleason KK. Texture and nanostructural engineering of conjugated conducting and semiconducting polymers. Mater Today Adv 2020, 8, 100086.

[4] Liu C, Huang K, Park WT, et al. A unified understanding of charge transport in organic semiconductors: The importance of attenuated delocalization for the carriers. Mater Horizons 2017, 4, 608–618.

[5] Ostroverkhova O. Organic optoelectronic materials: Mechanisms and applications. Chem Rev 2016, 116, 13279–13412.

[6] Nenashev A, Oelerich J, Baranovskii S. Theoretical tools for the description of charge transport in disordered organic semiconductor. J Phys Condens Matter 2015, 27, 093201.

[7] Noriega R, Rivnay J, Vandewal K, et al. A general relationship between disorder, aggregation and charge transport in conjugated polymers. Nat Mater 2013, 12, 1038–1044.

[8] Bikowski A, Ellmer K. Analytical model of electron transport in polycrystalline, degenerately doped ZnO films. J Appl Phys 2014, 116.
[9] Kinemuchi Y, Nakano H, Kaga H, Tanaka S, Uematsu K, Watari K. Microstructural evidence of Hall mobility anisotropy in c-axis textured Al-doped ZnO. J Am Ceram Soc 2011, 94, 2339–2343.
[10] Minami T. Transparent conducting oxide semiconductors for transparent electrodes. Semicond Sci Technol 2005, 20, S37.
[11] Jiang H, Hu W. The emergence of organic single-crystal electronics. Angew Chemie – Int Ed 2020, 59, 1408–1428.
[12] Bassler H. Charge transport in disordered organic photoconductors a Monte Carlo simulation study. Phys Status Solidi b 1993, 175, 15–56.
[13] Baranovskii SD. Mott lecture: Description of charge transport in disordered organic semiconductors: Analytical theories and computer simulations. Phys Status Solidi A 2018, 215, 1700676.
[14] Hussey NE, Takenaka K, Takagi H. Universality of the Mott-Ioffe-Regel limit in metals. Philos Mag 2004, 84, 2847–2864.
[15] Heeger A. Nobel lecture: "Synthetic metals": A novel role for organic polymer. Rev Mod Phys 2001, 73, 681–700.
[16] Stadler P. Isotropic metallic transport in conducting polymers. Synth Met 2019, 254, 106–113.
[17] Zabrodskii AG, Zinov'eva KN. Low-temperature conductivity and metal-insulator transition in compensate n-Ge. Sov Phys JETP 1984, 59, 425–433.
[18] Kohlman RS, Zibold A, Tanner DB, et al. Limits for metallic conductivity in conducting polymers. Phys Rev Lett 1997, 78, 3915–3918.
[19] Wang X, Zhang X, Sun L, et al. High electrical conductivity and carrier mobility in oCVD PEDOT thin films by engineered crystallization and acid treatment. Sci Adv 2018, 4.
[20] Liu H, Pourret A, Guyot-Sionnest P. Mott and Efros-Shklovskii variable range hopping in CdSe quantum dots films. ACS Nano 2010, 4, 5211–5216.
[21] Day R, Bediako D, Rezaee M, et al. Single crystals of electrically conductive two-dimensional metal–organic frameworks: Structural and electrical transport properties. ACS Cent Sci 2019, 5, 1959–1964.
[22] Graham M, Adkins C, Behar H, Rosenbaum R. Experimental study of the Ioffe-Regel criterion for amorphous indium oxide films. J Condens Matter 1998, 10, 809–819.
[23] Kang SD. Charge-transport model for conducting polymers. Nat Mater 2017, 16.
[24] Heydari Gharahcheshmeh M, Gleason KK. Texture and nanostructural engineering of conjugated conduction and semiconducting polymers. Mater Today Adv 2020, 100086.
[25] Pozdnyakov D. Scattering of electrons by ionized impurities in semiconductors: Quantum-mechanical approach to third body exclusion. J Comput Electron 2014, 13, 338–351.
[26] Seto JYW. The electrical properties of polycrystalline silicon films. J Appl Phys 1975, 46, 5247–5254.
[27] Heydari Gharahcheshmeh M, Gleason KK. Device fabrication based on oxidative chemical vapor deposition (oCVD) synthesis of conducting polymers and related conjugated organic materials. Adv Mater Interfaces 2019, 6, 1801564.
[28] Marcus RA, Sutin N. Electron transfers in chemistry and biology. BBA Rev Bioenerg 1985, 811, 265–322.
[29] Coropceanu V, Cornil J, Da Silva Filho DA, Olivier Y, Silbey R, Brédas JL. Charge transport in organic semiconductors. Chem Rev 2007, 107, 926–952.
[30] Kivelson S, Heeger AJ. Intrinsic conductivity of conducting polymers. Synth Met 1988, 22, 371–384.
[31] Miller A, Abrahams E. Impurity conduction at low concentrations. 1960, 120, 745–755.

[32] Gueye MN, Carella A, Faure-vincent J. Progress in materials science progress in understanding structure and transport properties of PEDOT-based materials: A critical review. Prog Mater Sci 2020, 108, 100616.
[33] Mott N. Conduction in non-crystalline materials: III. Localized states in a pseudogap and near extremities of conduction and valence bands. Philos Mag 1969, 19, 835–852.
[34] Lim JA, Liu F, Ferdous S, Muthukumar M, Briseno AL. Polymer semiconductor crystals. Mater Today 2010, 13, 14–24.
[35] Drewelow G, Wook Song H, Jiang ZT, Lee S. Factors controlling conductivity of PEDOT deposited using oxidative chemical vapor deposition. Appl Surf Sci 2020, 501, 144105.
[36] Efros AL, Shklovskii BI. Coulomb gap and low temperature conductivity of disordered systems. J Phys C Solid State Phys 1975, 8, 49–51.
[37] Efros AL, Skinner B, Shklovskii BI. Coulomb gap in the one-particle density of states in three-dimensional systems with localized electrons. Phys Rev B – Condens Matter Mater Phys 2011, 84, 1–5.
[38] Liu C, Huang K, Park WT, et al. A unified understanding of charge transport in organic semiconductors: The importance of attenuated delocalization for the carriers. Mater Horizons 2017, 4, 608–618.
[39] Ugur A, Katmis F, Li M, et al. Low-dimensional conduction mechanisms in highly conductive and transparent conjugated polymers. Adv Mater 2015, 27, 4604–4610.
[40] Sheng P. Fluctuation-induced tunneling conduction in disordered materials. Phys Rev B 1980, 21, 2180–2195.
[41] Mollinger SA, Krajina BA, Noriega R, Salleo A, Spakowitz AJ. Percolation, tie-molecules, and the microstructural determinants of charge transport in semicrystalline conjugated polymers. ACS Macro Lett 2015, 4, 708–712.
[42] Lee S, Borrelli DC, Jo WJ, Reed AS, Gleason KK. Nanostructured unsubstituted polythiophene films deposited using oxidative chemical vapor deposition: Hopping conduction and thermal stability. Adv Mater Interfaces 2018, 5, 1701513.
[43] Cui J, Martínez-Tong DE, Sanz A, Ezquerra TA, Rebollar E, Nogales A. Relaxation and conductivity in P3HT/PC71BM Blends as revealed by dielectric spectroscopy. Macromolecules 2016, 49, 2709–2717.
[44] Obrzut J, Page KA. Electrical conductivity and relaxation in poly(3-hexylthiophene). Phys Rev B – Condens Matter Mater Phys 2009, 80, 195211.
[45] Reynolds JR, Thompson BC, Skotheim TA. Conjugated Polymers Properties, Processing, and Applications, 4th Edition. Boca Raton, London, New York, CRC Press, Taylor and Francis Group, 2019.
[46] Li JT, Lu YC, Jiang S Bin, Zhong YL, Yeh JM. Phase diagram of hopping conduction mechanisms in polymer nanofiber network. J Appl Phys 2015, 118, 4–8.
[47] Cho B, Park KS, Baek J, Oh HS, Koo Lee YE, Sung MM. Single-crystal poly(3,4-ethylenedioxythiophene) nanowires with ultrahigh conductivity. Nano Lett 2014, 14, 3321–3327.
[48] Drewelow G, Wook Song H, Jiang ZT, Lee S. Factors controlling conductivity of PEDOT deposited using oxidative chemical vapor deposition. Appl Surf Sci 2020, 501, 144105.
[49] Wang X, Zhang X, Sun L, et al. High electrical conductivity and carrier mobility in oCVD PEDOT thin films by engineered crystallization and acid treatment. Sci Adv 2018, 4, eaat5780.
[50] Lee S, Paine DC, Gleason KK. Heavily doped poly(3,4-ethylenedioxythiophene) thin films with high carrier mobility deposited using oxidative CVD: Conductivity stability and carrier transport. Adv Funct Mater 2014, 24, 7187–7196.

[51] Shi W, Zhao T, Xi J, Wang D, Shuai Z. Unravelling doping effects on PEDOT at the molecular level: From geometry to thermoelectric transport properties. J Am Chem Soc 2015, 137, 12929–12938.
[52] Kim N, Kee S, Lee SH, et al. Highly conductive PEDOT:PSS nanofibrils induced by solution-processed crystallization. Adv Mater 2014, 26, 2268–2272.
[53] Rudd S, Franco-gonzalez JF, Singh SK, et al. Charge transport and structure in semimetallic polymers. J Polym Sci Part B Polym Phys 2018, 56, 97–104.
[54] Kim D, Zozoulenko I. Why is pristine PEDOT Oxidized to 33%? A density functional theory study of oxidative polymerization mechanism. J Phys Chem B 2019, 123, 5160–5167.
[55] Heinze J, Frontana-Uribe BA, Ludwigs S. Electrochemistry of conducting polymers-persistent models and new concepts. Chem Rev 2010, 110, 4724–4771.
[56] Nardes AM, Kemerink M, Janssen RAJ, et al. Microscopic understanding of the anisotropic conductivity of PEDOT:PSS thin films. Adv Mater 2007, 19, 1196–1200.
[57] Nardes AM, Kemerink M, Janssen RAJ. Anisotropic hopping conduction in spin-coated PEDOT: PSS thin films. Phys Rev B – Condens Matter Mater Phys 2007, 76, 085208.
[58] Honma Y, Itoh K, Masunaga H, et al. Mesoscopic 2D charge transport in commonplace PEDOT: PSS films. Adv Electron Mater 2018, 4, 2–7.
[59] Gueye MN, Carella A, Massonnet N, et al. Structure and dopant engineering in PEDOT thin films: Practical tools for a dramatic conductivity enhancement. Chem Mater 2016, 28, 3462–3468.
[60] Rolland N, Franco-Gonzalez JF, Volpi R, Linares M, Zozoulenko I V. Understanding morphology-mobility dependence in PEDOT:Tos. Phys Rev Mater 2018, 2, 045605.
[61] Xu Y, Wang X, Zhou J, et al. Molecular engineered conjugated polymer with high thermal conductivity. Sci Adv 2018, 4, eaar3031.
[62] Kim N, Lee BH, Choi D, et al. Role of interchain coupling in the metallic state of conducting polymers. Phys Rev Lett 2012, 109, 106405.
[63] Dong J, Portale G. Role of the processing solvent on the electrical conductivity of PEDOT:PSS. Adv Mater Interfaces 2020, 7.
[64] Fan X, Nie W, Tsai H, et al. PEDOT:PSS for flexible and stretchable electronics: Modifications, strategies, and applications. Adv Sci 2019, 6, 1900813.
[65] Heydari Gharahcheshmeh M, Tavakoli MM, Gleason EF, Robinson MT, Kong J, Gleason KK. Tuning, optimization, and perovskite solar cell device integration of ultrathin poly(3,4-ethylene dioxythiophene) films via a single-step all-dry process. Sci Adv 2019, 5, eaay0414.
[66] Heydari Gharahcheshmeh M, Robinson MT, Gleason EF, Gleason K. Optimizing the optoelectronic properties of face-on oriented Poly(3,4-Ethylenedioxythiophene) via water-assisted oxidative chemical vapor deposition. Adv Funct Mater 2020, 2008712.
[67] Lee S, Borrelli DC, Jo WJ, Reed AS, Gleason KK. Nanostructured unsubstituted polythiophene films deposited using oxidative chemical vapor deposition: Hopping conduction and thermal stability. Adv Mater Interfaces 2018, 5, 1701513.
[68] Fabretto M, Zuber K, Jariego-Moncunill C, Murphy P. Measurement protocols for reporting PEDOT thin film conductivity and optical transmission: A critical survey. Macromol Chem Phys 2011, 212, 2173–2180.
[69] Borrelli DC, Lee S, Gleason KK. Optoelectronic properties of polythiophene thin films and organic TFTs fabricated by oxidative chemical vapor deposition. J Mater Chem C 2014, 2, 7223–7231.

# 4 Optoelectronic properties

Conjugated polymers are of broad interest for optoelectronic devices [1–7]. One motivation is the desire to fabricate flexible versions of mechanically rigid inorganic devices. Inorganic materials are often mechanically brittle and thus can crack when flexed. Additionally, inorganic layers often require deposition temperatures higher than flexible plastic substrates can withstand. Conjugated polymers can be both more mechanically flexible and are able to be applied at low temperatures. Additionally, there is a desire to eliminate specific inorganic elements because they are either toxic or rare, and hence expensive.

For photovoltaic devices and light-emitting diodes, conjugated polymers have been extensively researched as transparent conducting electrodes (TCEs), hole transport layers, and as semiconductive active layers [8]. Conductive conjugated polymers are also of interest for use as crack-resistant TCEs for touchscreens [7, 9]. Nanostructures from conjugated polymers can possess attractive properties for applications including light harvesting, plasmonic lasing, biophotonics, and photocatalysis [10].

## 4.1 Frequency dependent dielectric behavior

All the fixed and mobile charges in a material respond to the electromagnetic field of light [3, 5]. The response depends on the angular frequency of the light and is described by the complex dielectric function, $\varepsilon(\omega) = \varepsilon_1(\omega) + i\varepsilon_2(\omega)$. The dielectric function can be obtained from transmission or reflection measurements. Absorption peaks in the spectral range for ultraviolet and visible light typically correspond to transitions between electronic states that can be displayed on a DOS diagram. Covalent chemical bonds act as local oscillators at infrared frequencies. The corresponding transitions between vibronic states are typically observed at infrared frequencies using Fourier transform infrared (FTIR) or Raman spectroscopies. Because of the quantum mechanical selection rules governing the allowable optical transitions differ for FTIR and Raman, these two methods are complementary. Higher frequency processes can be accessed through terahertz (THz) spectroscopy. In nonisotropic materials, the optical constants can depend on the direction of measurement. This anisotropy can be observed using variable angle spectroscopic ellipsometry.

The frequency-dependent optoelectronic response of an electron has been modeled as **Lorentz oscillator** [11]. In a localized covalent bond, there is restorative force which depends on bond strength. Conventional dielectric polymers give rise to multiple optical adsorption peaks, each centered at a different frequency. A given peak appears at the energy which is signature of a particular type of covalent chemical bond, enabling the assignment of peaks in FTIR and Raman spectroscopy. Since bonding

https://doi.org/10.1515/9781501524615-004

orbitals are often not isotropic, varying the angle of incidence of the light can reveal the orientation distribution of the polymer chains.

The **Drude model** assumes only a single oscillator with no restoring force. The Drude model is widely used for conventional metals and has also been applied for conjugated polymers [3, 5, 7]. When low-frequency light is incident upon a metal, the displacement of mobile charge carriers can maintain a zero value of electric field in the solid. In this case, the incident oscillating electromagnetic wave is reflected. Reflection gives common metals their shiny appearance. Highly conductive poly(acetylene) (PA) has also been reported to have a silvery appearance [12].

At high frequencies, metals become transparent. Transparency occurs when the external field oscillates too rapidly for the free charge carrier gas of the metal to follow. According to the Drude model, the transition between a reflective and transparent response occurs at the **plasmon frequency,** $\omega_p$, as given by [7, 13]

$$\omega_p = \sqrt{\frac{n_c e^2}{\varepsilon_0 m^*}} \tag{4.1}$$

An important consequence of eq. (4.1) is that charge carrier density, $n_c$, determines range of the frequencies yielding transparent behavior, $\omega > \omega_p$.

More complex models incorporate deviations from the assumption of completely free charge carriers [5]. For example, the **Drude–Smith model** considers weak carrier confinement, where the mean free path of the charge carrier is comparable to the mesoscale of the confining structure. Indeed, the Drude–Smith model has been applied to a wide range of nanomaterials, where short-range charge carrier dynamics are studied by THz spectroscopy [14]. The Drude–Smith model also provides an accurate description of the frequency dependent dielectric behavior of conjugated polymers with mesoscale crystalline domains [5].

## 4.2 Transparent conductors

For TCEs, transparency is typically desired in the visible region, from ~400 to 800 nm. Using eq. (4.1), a corresponding plasmon wavelength for the Drude model can be defined as

$$\lambda_p = \frac{2\pi\hbar}{\omega_p} \tag{4.2}$$

In terms of wavelength, transparency requires that $\lambda < \lambda_p$, making materials with $\lambda_p$ values of 1 μm or more attractive candidates for TCEs. Since the transition between transmission and reflection in a real conductor is more gradual than in a Drude metal, the degree of transparency is generally improved by increasing $\lambda_p$ relative to the wavelength of interest. From eqs. (4.1) and (4.2), increasing $\lambda_p$ requires a lower

$\omega_p$, thus a lower charge carrier density, $n_c$. Thus, higher transparency is often associated with lower electrical conductivity, representing a general challenge for TCE materials development. Selected values of $\lambda_p$ are:

- <0.2 μm (deep UV) for metals, having $n_c \sim 10^{22}/cm^3$ [7],
- ~1 μm (near IR) for inorganic transparent conducting oxides, having $n_c \sim 10^{21}/cm^3$ [7],
- >2 μm (mid-IR) for carbon-based conductors, having $n_c \sim 10^{20}/cm^3$ [7],
- 0.4 μm for PA doped with $I_2$ ($\sigma_{dc}$ = 4500 S/cm) [15],
- 1.1 μm for poly(pyrrole) (PPy) doped with hexafluorophosphate ($PF_6$; $\sigma_{dc}$ = 300 S/cm) [15],
- 1.3 μm for poly(aniline) (PANI) doped with camphor sulfonic acid ($C_{10}H_{15}O-SO_3H$; $\sigma_{dc}$ = 400 S/cm) [15], and
- ~0.4 to 1.6 μm for various commercial grades of PEDOT:PSS of differing $\sigma_{dc}$ values [16, 17].

All the $\sigma_{dc}$ values listed above are from room-temperature measurements. In the case of highly conducting PA, PANI, and PPy, a second plasmon oscillation was observed, having $\lambda_p$ ~40 μm and representing a deviation from the Drude model that was attributed to the most delocalized electrons [15]. A similar second plasmon in PEDOT:PSS was reported as a deviation from the Drude model [17].

As introduced in Chapter 3, transparent conductive oxides (TCOs) are widely used as TCEs in conventional devices. The brittleness, high cost, and raw materials scarcity of TCOs make the more difficult to integrate into flexible and wearable devices. The comparison of TCE materials uses a figure of merit (FoM) which is the ratio of the dc electrical conductivity, $\sigma_{dc}$, to the electrical conductivity at the optical frequency of interest, $\sigma_{op.}$ The FoM is calculated from the measured values of transmittance at the optical frequency $T(\lambda)$, and the $R_s$, the sheet resistance (Section 3.10). The most commonly $\lambda$ is the visible wavelength of 550 nm. The FoM is extracted from the following equation [7, 18]:

$$T(\lambda) = \left(1 + \frac{z_0}{2R_{Sh}} \frac{1}{F_o M}\right)^{(-2)} \tag{4.3}$$

where $z_o$ is the impedance of free space, 377 Ω. At 550 nm, A TCO film of indium tin oxide with $R_{sh}$ =10 Ω/sq, has a transmittance of 0.9, corresponding to an FoM of ~348.

Desirable candidates for flexible TCE applications have FoM values >35, where even higher values preferred. For PEDOT:Cl synthesized by oxidative chemical vapor deposition (oCVD), FoM value of 94 has been reported [1]. Figure 4.1 summarizes recent results for PEDOT thin films produced by different methods, graphene, graphene oxide, carbon nanotubes, metal nanowires and their composites [7].

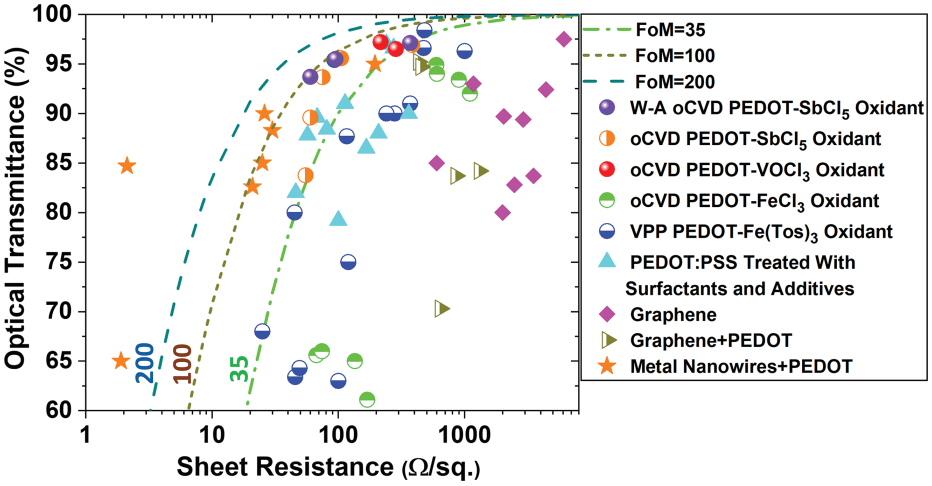


**Fig. 4.1:** The optical transmittance, $T$, and sheet resistance, $R_{sh}$, for several classes of mechanical flexible transparent conductors, taken from Refs. [1, 7]. The dotted lines display constant values of FoM of 35, 100, and 200, calculated using eq. (4.3). Adapted with permission from Heydari Gharahcheshmeh and Gleason, Mater. Today Adv., 8, 10008 (2020) Copyright 2020, Elsevier.

## 4.3 Anisotropy and chirality

Reflectivity spectroscopy combined with the Kramers–Kronig relationship was applied to well-oriented poly(acetylene) [3] doped with $I_2$. Reflectivity was high along the direction of the $-(CH_2)-$ backbone, but low in other directions. This observed anisotropy is consistent with metallic conduction in the direction parallel to the polymer chain, but semiconducting behavior in the perpendicular directions. Optical anisotropy has also been reported in a large number of other conjugated polymers including poly(phenylenevinylene) and its derivatives, poly(3-hexylthiophene) (P3HT), and n-type poly(fluorenes) [19].

Techniques for measuring the optical anisotropy of conjugated polymers have been reviewed [19]. For some methods, there is a high degree of correlation between in-plane and out-of-plane fitting parameters that can skew the results. Thus, the use of more than one method of measurement was recommended. Analyzing spectroscopic ellipsometry data with a Drude model modified by the inclusion of additional Lorentzian oscillators predicted the anisotropy of electrical conductivity in conjugated polymer films. With this method, the anisotropy ratio, equal to the in-plane divided by the out-of-plane electrical conductivity, was determined to be >1 for different PEDOT:counterion combinations synthesized by various methods. For a PEDOT:TOS film grown by vapor-phase polymerization and having an in-plane conductivity of 670 S/cm, the ellipsometrically determined anisotropic ratio was ~20 [20]. For a set of six PEDOT:PSS films of increasing PSS content, the anisotropic ratios

determined by ellipsometry ranges from ~20 to ~$1 \times 10^5$ [21]. The optically determined anisotropy in conductivity is consistent with values obtained by direct electrical measurements.

**Chiral conjugated polymers** have been used to recognize chiral biomolecules, allowing stereoisomers to be distinguished [22]. Chiral properties are also of interest for optoelectronic and photonic devices and for quantum computing [23]. Chiral conjugated polymers are also of high interest for their magneto-optical properties, which allow applied magnetic fields to modulate the transmission of polarized light [24]. Synthesis can either utilize a chiral monomer such as the one functionalized with an amino acid or an achiral molecule under polymerization conditions that induce chirality [22, 23]. For example, dilute solutions of deoxyribonucleic acid (DNA) form lyotropic chiral nematic liquid crystals. Using solutions of DNA for electropolymerization gave PEDOT with a helical structure which assembled into a fibril microstructure. Magnetic fields have been used to alter electropolymerization carried out in chiral liquid crystals. For the monomer 1,4-di(2-thienyl)benzene, helical structures resulted in the absence of magnetic field, while a strip texture formed parallel to an applied field of 4 Tesla.

Alternatively, the interchain interactions of conjugated molecules and polymers can create chiral supramolecular structures [25]. These aggregates have been intensively investigated using electronic circularly dichroism and circularly polarized luminescence. The most studied chiral polymers with conjugated backbones are based on poly(acetylene), poly(diacetylene), poly(*p*-phenylene), poly(fluorene), and poly(thiophene).

## 4.4 Optical absorption and emission

For a semiconducting material, light absorption results in the promotion of an electron to a state lying above an energy bandgap, leaving a hole behind the lower energy state. An electrostatic attraction exists between the newly created electron and hole, creating a bound state called an exciton. The **Coulomb's law** gives the attraction potential, $V$, for an electron and hole separated by a distance, $d$, is given by

$$V = \frac{e^2}{4\pi\varepsilon_r\varepsilon_0 d} \tag{4.4}$$

This Coulombic binding energy is higher when the dielectric constant of the material, $\varepsilon_r$, is low. Thus, in organic materials, where $2 < \varepsilon_r < 4$ is typical, excitons are more localized than in higher dielectric constant inorganics, such as GaAs with $\varepsilon_r = 11$ [26]. An exciton can migrate before decaying. One pathway for the relaxation of the excitonic state is luminescence, a phenomena that underlies the operation of light-emitting diodes.

The **optical band gap energy**, $E_g$, can be determined from the optical absorption spectrum. The spectrum is most commonly obtained using ultraviolet–visible–near-infrared (UV–vis–NIR) absorption spectroscopy, which uses widely available instrumentation and requires no special sample preparation [7]. More sensitive method of photothermal defection spectroscopy has also been used [27]. In both methods, the absorbance per unit of film thickness, $\alpha$, is measured as a function of the incident photon frequency, $\nu$.

In disordered materials, the optical absorption occurs as a direct band gap transition [7, 28]. Thus, for conjugated polymer, the bandgap energy, $E_g$, can be determined using the **Tauc relationship** [6]:

$$\alpha h\nu = A\left(h\nu - E_g\right)^{1/2} \tag{4.5}$$

Equation (4.5) predicts that a plot of $(\alpha h\nu)^{1/2}$ versus $h\nu$ will have a linear region near the band gap. The corresponding tangent line will have an intercept of $E_g$ on the $h\nu$ axis. Doping decreases the band gap as illustrated by a series of highly conductive PEDOT:Cl films in Fig. 4.2.

Crystalline and amorphous semiconductors, and well-as insulators, display exponential optical absorption tails, known as Urbach edges [29]. The larger the width of tail, the greater the degree of disorder. In the case of single crystal, the disorder arises from the temperature dependent occupation of the phonon states. For solids which are not single crystals, both thermally induced disorder and topological disorder contribute to the width of the Urbach edge.

The **Urbach energy**, $E_U$, represents the width of the optical absorption tail. In the band tail region below $E_g$, a plot of $\ln(\alpha)$ versus $h\nu$ is predicted to be a straight line. The inverse slope of this line equal gives $E_{U,}$ as shown by the following equation:

$$\ln \alpha = \ln \alpha_0 + \left(\frac{h\nu}{E_U}\right) \tag{4.6}$$

where $\alpha_0$ is constant.

The Urbach energy is related to the energy distribution of the localized electronic states responsible for hopping conduction (Fig. 1.3a). Indeed, an excellent correlation was found between the activation energy for charge carrier mobility, determine using field effect transistors (FETs), and the $E_U$ values measured by photothermal deflection spectroscopy [27]. This relationship between electronic conduction and optical absorption confirms that both processes involve the localized carriers at the top of the valence (HOMO) band.

The values of $E_U$ provide a means to compare the relative degree of disorder between materials. As a points of reference, $k_BT$ at 298 K, 25.7 meV and a typical $E_U$ value for the inorganic semiconductor amorphous silicon is 67 meV [28]. For a conjugated polymer, the lowest reported value is 24 meV [30], observed in undoped poly(indacenodithiophene-co-benzothiadiazole (IDT-BT). This $E_U$ value indicates a

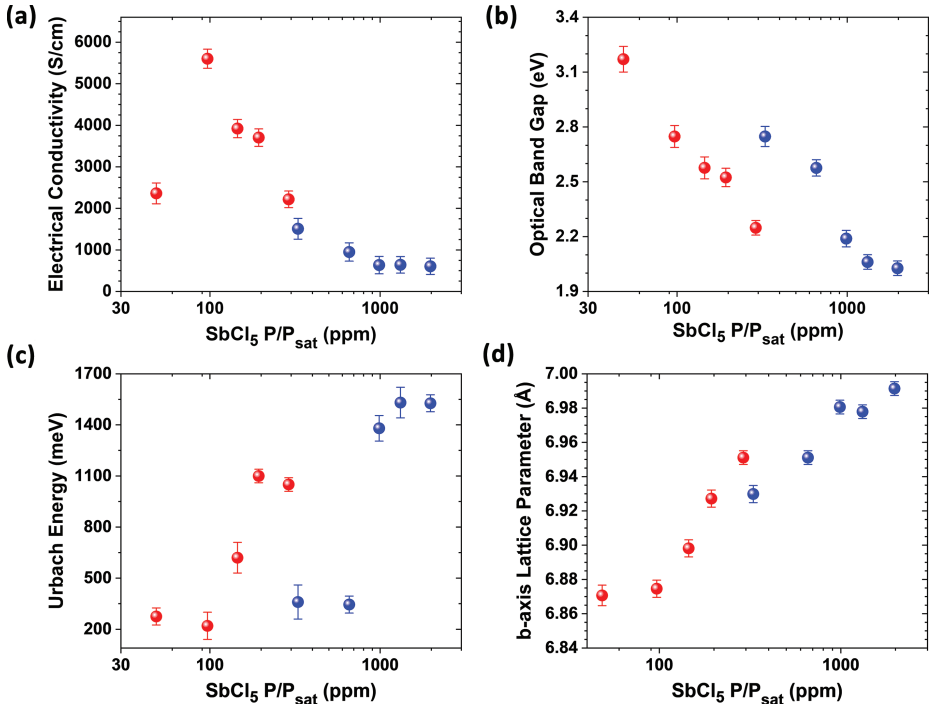


**Fig. 4.2:** The room-temperature optoelectronic properties of a series of PEDOT:Cl films depends on the partial pressure of the antimony pentachloride oxidant used during oCVD at surface growth temperatures of 90 °C (blue) and 140 °C (red) [1](a) electrical conductivity, $\sigma_{dc}$; (b) band gap energy, $E_g$; and (c) Urbach energy, $E_U$, and (d) the π–π stacking distance, on which the transfer integral depends (eq. (3.14)). Adapted with permission from Heydari Gharahcheshmeh and Gleason, Adv. Funct. Mater. 2008712. (2020) Copyright 2020, Wiley.

low degree of disorder in IDT-BT. Indeed, IDT-BT semiconducting thin films exhibited high charge carrier mobility when integrated in to FETs and the resulting devices displayed nearly ideal electrical characteristics [31].

For P3HT and poly(2,5-bis(3-alkylthiophen-2-yl)thieno(3,2-b)thiophene (PBTTT), $E_U$ ~ 40 meV [31]. The chemical structure, morphology, and charge transport mechanism of IDT-BT, P3HT, and PBTTT will be discussed further in Section 4.5.

The counterions present in doped conjugated polymers increase $E_U$. For a series of PEDOT films with $Cl^-$ counterions (Fig. 4.2), the $E_U$ varied from 205 to ~1600 meV. The highest conductivity film, 7520 ± 240 S/cm this series, corresponds to minimum Urbach energy. For poly(aniline) (PANI) with $Cl^-$ counterions, the measured value of $E_U$ was 3000 meV. In addition, a high degree of disorder may correspond to the multiple oxidation states doping possible for PANI. Blends of PEDOT:PSS with PANI had $E_U$ values ranging from 390 to 530 meV [32].

The conditions used for the synthesis and post-processing of a given material will affect $E_U$. A range of $E_U$ values between 390 and 530 meV was reported for

poly(*N*-benzylaniline) subjected to different annealing temperatures [33]. Blending with inorganic particles to create composites results in higher $E_U$ values. For hybrid organic–inorganic composites created using PEDOT:PSS, the $E_U$ values occurred in the range from 2200 to 3500 meV [34, 35].

## 4.5 Semiconducting conjugated polymers and their applications

Semiconducting conjugated polymers are of broad interest for the economical fabrication of devices over large areas and on to flexible substrates. Some of devices of interest are shown in Fig. 4.3 and include organic thin-film transistors [36], organic light-emitting diodes [36], and organic photovoltaics (oPV) [37]. The same electronic and optoelectronic applications have motivated interest in organic solids composed of small conjugated molecules. The ability to readily purify small molecules benefits the study of fundamental exciton physics and much of this understanding is transferable to macromolecular solids.

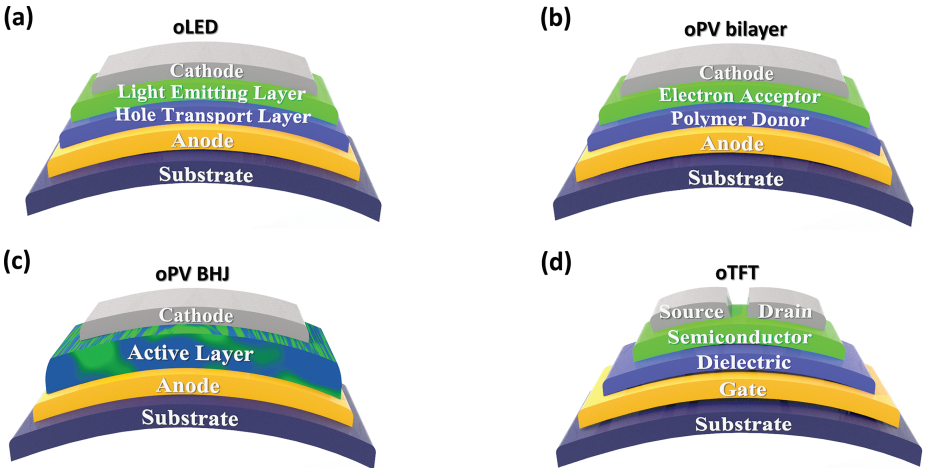


**Fig. 4.3:** Schematics of flexible organic device structures where semiconducting and conducting conjugated polymers can be integrated as one or more layers of the device stack: (a) organic light-emitting diode (oLED), (b) organic photovoltaic (oPV) where the photoactive region has a bilayer structure, (c) oPV with a bulk heterojunction (BHJ) photo active region, and (d) organic thin film transistor (oTFT).

In both small-molecule and polymeric organic optoelectronic materials, π–π stacking motifs control exciton delocalization and transport. The regions of conjugation are referred to as chromophores. Aggregates of small conjugated molecules determine their photophysics, and this concept has been extended to polymeric semiconductors [38]. Face-to-face packing, leading to interchain coupling (Fig. 2.1b), produce H-aggregates.

The side-by-side arrangement of regions of conjugation, as occurs for intrachain coupling (Fig. 2.1a), is denoted as J-aggregates. Indeed, single isolated chains give the expected photoemission behavior associated with J-aggregates.

In solid-state photocarrier generation, there is a competition between J-type and H-type behavior, depending both on the specific polymer of interest and the morphology induced by the processing method. For example, films of P3HT show H-type behavior, whereas whiskers of P3HT display J-aggregate characteristics [38]. For spin-cast P3HT films, temperature-dependent absorption and photoluminescence spectroscopy have virtually no contribution from intrachain excitons [39]. Interchain coupling energies of approximately 5 and 30 meV are observed when the solvents used for spin casting were isodurene and chloroform, respectively.

A variety of advanced spectroscopic techniques have been applied to visualizing the spatial localization and time-dependent behavior of excitons in small molecule organic semiconductors [40]. For example, time-delayed fluorescence provides spatiotemporal maps of mean square exciton displacement along different crystallographic axes [41]. In the single-crystal molecular semiconductor tetracene ($C_{18}H_{12}$), the exciton diffusivity was $2.28 \times 10^{-3}$ cm$^2$/s in the plane of conjugation. The diffusivity in the orthogonal direction was nearly ten times lower, $0.31 \times 10^{-3}$ cm$^2$/s. At 1 μs after laser-induced excitation, the measured mean square displacement of the exciton in the tetracene crystal was ~2000 nm in-plane and ~700 nm out-of-plane.

The total energy of electronically and vibronically excited states in organic molecules has several underlying contributions [40, 42]. The magnitude of each of these component energies can be determined though either optical spectroscopy methods or by the modeling of the operation of devices, such as TFTs. Often, temperature-dependent data is required. Additionally, the underlying Hamiltonians for each component allow the magnitudes of each contribution to be predicted through computations methods, such as density functional theory.

1) **Electronic and vibrational excitation energy** arising from an isolated molecule.
2) The **transfer integral**is the energy associated with charge carrier transfer between sites. In conjugated systems, this energy is the transfer integral resulting from to π–π stacking (3.14). Larger values of the transfer integral indicated larger degrees of charge carrier delocalization and are associated with increase values of charge carrier mobility [2, 6, 7]. The transfer integral energy typically falls in the range from 10 to 200 meV [40].
3) **Reorganization energy** is associated with the change in molecular geometry resulting from a charge transfer event. The change in geometry results in a corresponding change in the electronic polarization, representing a coupling between electrons and phonons. The reorganization energy typically falls in the range from 8 to 180 eV [40]. Large values are characteristic of polaronic charge transport by hopping (Section 3.4).
4) **Static disorder** corresponds to the temperature-independent proportion of the Urbach energy (Section 4.4).

Large values of the transfer integral and small values of the reorganization energy are desired for achieving high charge carrier mobility [7, 42]. Charge carriers motilities in excess of 7 $cm^2V/s$ have been reported for p-type, n-type, and ambipolar semiconducting polymers, with the highest value of 52.7 meV achieved using a p-type material [40].

Figure 4.4 shows the chemical structure of the semiconducting polymer, P3HT. The optoelectronic properties of P3HT have been extensively reported [43–45]. The conjugated backbone of the homopolymer P3HT is formed from thiophene rings substituted at position 3 with a hexyl group. The hexyl substituents make the P3HT solution processable, an important distinction from its unsubstituted counterpart, poly(thiophene). The hexyl groups also strongly influence solid-state morphology. In some cases, the pendent groups form insulating lamella between the conjugated backbones. Achieving a semicrystalline, edge-on microstructure results in P3HT films with high mobility in both the direction of the chain backbone and the direction of π–π stacking [42].

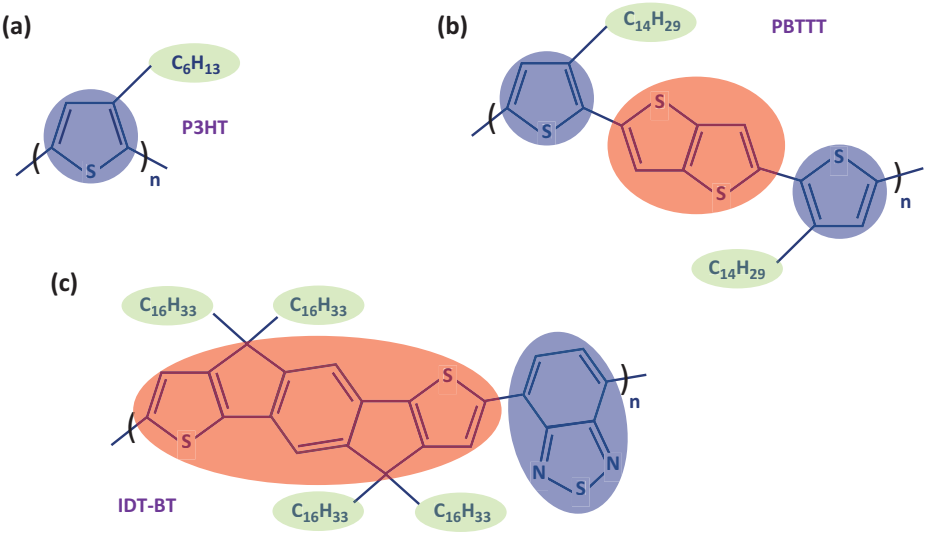


**Fig. 4.4:** The chemical structures of poly(3-hexylthiophene) (P3HT), poly(2,5-bis(2-alklythiophen-2-yl)thieno(3,2-b)thiophene) (PBTTT), and poly(indacenodithiophene-co-benzothiadiazole (IDT-BT). Green shading identifies the alkyl pendent groups on all three polymers. The conjugation regions along the backbone are shaded in blue or red. The blue shading is used to indicate an acceptor unit on the donor–acceptor copolymer IDT-BT.

Figure 4.4 also shows the chemical structure of poly(2,5-bis(2-alklythiophen-2-yl) thieno(3,2-b)thiophene) (PBTTT). Like P3HT, PBTTT possesses pendant alkyl groups ($-C_nH_{2n+1}$) attached to a conjugated backbone. The repeating polymeric units has two thiophene rings substituted at the 3-position with an intervening pair of fused thiophene rings. The same semicrystalline, edge-on morphology that optimized the mobility of P3HT results in an even higher mobility for PBTTT [42].

High-efficiency charge injection and extraction, as desired for oPV applications, along with high mobility can be achieved utilizing more sophisticated backbone structures, such as that of IDT-BT (Fig. 4.3, Section 4.4). The IDT units, which are electron rich, alternate with the BT units, which are electron deficient, to create a donor–acceptor (D–A) copolymer. Noncovalent interactions between the nitrogen on the BT unit and IDT units on the same chain may serve to stabilize the planar configuration of the chain [16]. The ability of noncovalent interactions between adjacent monomer units on a chain to stabilize a planar configuration was also noted in the case of PEDOT (Section 2.4).

Like P3HT and PBTTT, IDT-BT possesses alkyl side chains. However, unlike P3HT and PBTTT, an ordered semicrystalline morphology is not required to achieve high mobility in IDT-BT and many of its donor–acceptor copolymer counterparts [42]. The performance of the D–A copolymers may be a result from their planar conformations of their backbones. The extended fused-ring conjugated planar structures, such as IDT, result in efficient chain packing with a high transfer integral. Thus, significant interchain hopping may occur in both the crystalline and amorphous domains [46], making the mobility less sensitive to mesoscale semicrystalline morphology. Indeed, some total amorphous conjugated polymers, such as poly(triaryl amine), exhibit high mobility. Using near-edge X-ray adsorption fine structure measurements reveals a correlation between the orientation of the chains in both the crystalline and amorphous domains the D–A copolymer IDT-BT [46]. No such correlation was found for P3HT.

The microstructure of semicrystalline polymers has been classified according to a paracrystallinity parameter, $g$ [42, 47]. The value of $g$ is the standard deviation of atomic positions from a crystalline lattice site, normalized to the lattice spacing. When $g$ <1%, the materials is highly crystalline. Amorphous materials typically have $g$ > 10%. The values of g in the crystalline domains of high mobility P3HT and PBTTT are typically in the range of ~6–8%, while the corresponding range for D–A polymers. is 10–15% [42]. In both the highly ordered and less-ordered aggregates, tie chains between the crystalline domains are hypothesized to be critical for achieving high mobility.

## References

[1] Heydari Gharahcheshmeh M, Robinson MT, Gleason EF, Gleason KK. Optimizing the optoelectronic properties of face-on oriented chemical vapor deposition. Adv Funct Mater 2020, 2008712.

[2] Gleason KK. Nanoscale control by chemically vapour-deposited polymers. Nat Rev Phys 2020, 2, 347–364.

[3] Kiess HG, Harbeke G. Optical properties of conducting polymers. In: Conjugated Conducting Polymers Springer-V. 1992, 175–216.

[4] Alias A., Zabidi A., Ali AM., Harun M., Yahya MZ. Optical characterization and properties of polymeric materials for optoelectronic and photonic applications. Int J Appl Sci Technol 2013, 3, 11–38.

[5] Kim N, Petsagkourakis I, Chen S, et al. Electric Transport Properties in PEDOT Thin Films from: Conjugated Polymers, Properties, Processing, and Applications. CRC Press, 2019, p. 45.
[6] Heydari Gharahcheshmeh M, Tavakoli MM, Gleason EF, Robinson MT, Kong J, Gleason KK. Tuning, optimization, and perovskite solar cell device integration of ultrathin poly(3,4-ethylenedioxythiophene) films via a single-step all-dry process. Sci Adv 2019, 5, eaay0414.
[7] Heydari Gharahcheshmeh M, Gleason KK. Texture and nanostructural engineering of conjugated conducting and semiconducting polymers. Mater Today Adv 2020, 8, 100086.
[8] Jiang Y, Liu T, Zhou Y. Recent advances of synthesis, properties, film fabrication methods, modifications of Poly(3,4-ethylenedioxythiophene), and applications in solution-processed photovoltaics. Adv Funct Mater 2020, 51, 2006213.
[9] Cao W, Li J, Chen H, Xue J. Transparent electrodes for organic optoelectronic devices: A review. J Photonics Energy 2014, 4, 040990.
[10] Tuncel D. π-Conjugated nanostructured materials: Preparation, properties and photonic applications. Nanoscale Adv 2019, 1, 19–33.
[11] Ouyang J, Xu Q, Chu CW, Yang Y, Li G, Shinar J. On the mechanism of conductivity enhancement in poly(3,4- ethylenedioxythiophene):Poly(styrene sulfonate) film through solvent treatment. Polymer (Guildf) 2004, 45, 8443–8450.
[12] Minhai H, Mingku Y, Zhaowu T. Polyacetylene film formed by electrochemical technique. Acta Physico-Chemica Sin 1985, 1, 193–195.
[13] Wang Y, Plummer EW, Kempa K. Foundations of plasmonics. Adv Phys 2011, 60, 799–898.
[14] Cocker TL, Baillie D, Buruma M, et al. Microscopic origin of the Drude-Smith model. Phys Rev B 2017, 96, 205439.
[15] Epstein AJ, Joo J, Kohlman RS, et al. Inhomogeneous disorder and the modified Drude metallic state of conducting polymers. Synth Met 1994, 65, 149–157.
[16] Wadsworth A, Chen H, Thorley KJ, et al. Modification of indacenodithiophene-based polymers and its impact on charge carrier mobility in organic thin-film transistors. J Am Chem Soc 2020, 142, 652–664.
[17] Herrmann F, Engmann S, Presselt M, Hoppe H, Shokhovets S, Gobsch G. Correlation between near infrared-visible absorption, intrinsic local and global sheet resistance of poly ( 3, 4-ethylenedioxy- thiophene) poly ( styrene sulfonate) thin films. Appl Phys Lett 2012, 100, 153301.
[18] Heydari Gharahcheshmeh M, Gleason KK. Device fabrication based on oxidative chemical vapor deposition (oCVD) synthesis of conducting polymers and related conjugated organic materials. Adv Mater Interfaces 2019, 6, 1801564.
[19] Campoy-Quiles M, Etchegoin PG, Bradley DDC. On the optical anisotropy of conjugated polymer thin films. Phys Rev B – Condens Matter Mater Phys 2005, 72, 045209.
[20] Chen S, Kühne P, Stanishev V, et al. On the anomalous optical conductivity dispersion of electrically conducting polymers: Ultra-wide spectral range ellipsometry combined with a Drude-Lorentz model. J Mater Chem C 2019, 7, 4350–4362.
[21] Bracke W, Cheng WJ, Pearson JM, Szwarc M. Formation of carbonium Ions by Cl+ transfer from antimony pentachloride to olefins. J Am Chem Soc 1969, 91, 203–204.
[22] Ibanez JG, Rincón ME, Gutierrez-Granados S, Chahma M, Jaramillo-Quintero OA, Frontana-Uribe BA. Conducting polymers in the fields of energy, environmental remediation, and chemical-chiral sensors. Chem Rev 2018, 118, 4731–4816.
[23] He C, Feng Z, Shan S, Wang M, Chen X, Zou G. Highly enantioselective photo-polymerization enhanced by chiral nanoparticles and in situ photopatterning of chirality. Nat Commun 2020, 11. 1188.
[24] Swager TM. 50th anniversary perspective: Conducting/semiconducting conjugated polymers. A personal perspective on the past and the future. Macromolecules 2017, 50, 4867–4886.

[25] Albano G, Pescitelli G, Di Bari L. Chiroptical properties in thin films of π-conjugated systems. Chem Rev 2020, 120, 10145–10243.
[26] Noriega R, Rivnay J, Vandewal K, et al. A general relationship between disorder, aggregation and charge transport in conjugated polymers. Nat Mater 2013, 12, 1038–1044.
[27] Kronemeijer AJ, Pecunia V, Venkateshvaran D, et al. Two-dimensional carrier distribution in top-gate polymer field-effect transistors: Correlation between width of density of localized states and urbach energy. Adv Mater 2014, 26, 728–733.
[28] Cody GD, Tiedje T, Abeles B, Brooks B, Goldstein Y. Disorder and the optical-absorption edge of hydrogenated amorphous silicon. Phys Rev Lett 1981, 47, 1480–1483.
[29] Urbach F. The long-wavelength edge of photographic sensitivity and of the electronic Absorption of Solids. Phys Rev 1953, 92, 1324.
[30] Cho B, Park KS, Baek J, Oh HS, Koo Lee YE, Sung MM. Single-crystal poly(3,4-ethylenedioxythiophene) nanowires with ultrahigh conductivity. Nano Lett 2014, 14, 3321–3327.
[31] Venkateshvaran D, Nikolka M, Sadhanala A, et al. Approaching disorder-free transport in high-mobility conjugated polymers. Nature 2014, 515, 384–388.
[32] Banerjee S, Kumar A. Swift heavy ion irradiation induced modifications in the optical band gap and Urbach's tail in polyaniline nanofibers. Nucl Instruments Methods Phys Res Sect B 2011, 269, 2798–2806.
[33] Bengasi G, Baba K, Back O, Frache G, Heinze K, Boscher ND. Reactivity of Nickel(II) Porphyrins in oCVD processes – polymerisation, intramolecular cyclisation and chlorination. Chem – A Eur J 2019, 25, 8313–8320.
[34] Ram J, Singh RG, Singh F, et al. Ion beam engineering in WO3-PEDOT: PSS hybrid nanocomposite thin films for gas sensing measurement at room temperature. Inorg Chem Commun 2020, 119, 108000.
[35] Ahn S, Jeong SH, Han TH, Lee TW. Conducting polymers as anode buffer materials in organic and perovskite optoelectronics. Adv Opt Mater 2017, 5, 1600512.
[36] Rudd S, Franco-gonzalez JF, Singh SK, et al. Charge transport and structure in semimetallic polymers. J Polym Sci Part B Polym Phys 2018, 56, 97–104.
[37] Zhou H, Yang L, You W. Rational design of high performance conjugated polymers for organic solar cells. Macromolecules 2012, 45, 607–632.
[38] Kivelson S, Heeger AJ. Intrinsic conductivity of conducting polymers. Synth Met 1988, 22, 371–384.
[39] Clark J, Silva C, Friend RH, Spano FC. Role of intermolecular coupling in the photophysics of disordered organic semiconductors : Aggregate emission in regioregular polythiophene. Phys Rev Lett 2007, 98, 206406.
[40] Ostroverkhova O. Organic optoelectronic materials: Mechanisms and applications. Chem Rev 2016, 116, 13279–13412.
[41] Akselrod GM, Deotare PB, Thompson NJ, et al. Visualization of exciton transport in ordered and disordered molecular solids. Nat Commun 2014, 5, 3646.
[42] Sirringhaus H. 25th anniversary article : Organic field-effect transistors : The path beyond amorphous silicon. Adv Mater 2014, 26, 1319–1335.
[43] Hynynen J, Kiefer D, Yu L, et al. Enhanced electrical conductivity of molecularly p - doped Poly ( 3- hexylthiophene) through understanding the correlation with solid- state order. Macromolecules 2017, 50, 8140–8148.
[44] Sirringhaus H, Brown PJ, Friend RH, et al. Two-dimensional charge transport in conjugated polymers. Nature 1999, 401, 685–689.

[45] Zen A, Pflaum J, Hirschmann S, et al. Effect of molecular weight and annealing of Poly ( 3-hexylthiophene) s on the performance of organic field-effect transistors. Adv Funct Mater 2004, 14, 757–764.
[46] Zhang X, Bronstein H, Kronemeijer AJ, et al. Molecular origin of high field-effect mobility in an indacenodithiophene–benzothiadiazole copolymer. Nat Commun 2013, 4, 2238.
[47] Noriega R, Salleo A, Spakowitz AJ. Chain conformations dictate multiscale charge transport phenomena in disordered semiconducting polymers. Proc Natl Acad Sci 2013, 110, 16315–16320.

# 5 Ionic transport

Despite its complexity, the presence of mixed ionic and electronic conduction (MIEC) in conjugated polymers has attracted significant attention [1–5]. The applications for MIEC include energy storage, energy harvesting, environmental remediation, sensing, actuation, corrosion protection, bioelectronics, drug delivery, electrochromics, and electrocatalysis [2, 6–12]. The dynamics of ionic transport control the switching speed of electrochromic windows between their undoped, high-band gap transparent state to their absorbing colored state [13]. The mechanical strain induced by swelling and deswelling of conjugated polymers upon doping and dedoping represents an actuation method for artificial muscles and wearable electronics applications [14]. High ionic mobilities are also essential for high-rate energy storage in electric vehicles and the load leveling of intermittent renewal energy [6, 15]. Additionally, the electrochemical synthesis of conjugated polymers is a well-established method for forming films on electrically conducting substrates [1, 2, 5].

The uptake of ions by conjugated polymers has been extensively explored as a means to enhance electrical conductivity, as was discussed in the earlier section on doping (Section 1.3). The doping process inherently links ionic and electronic transport in conjugated polymers. Since nanoscale order and texture have a profound effect on electrical mobility (Chapter 3), similar effects are anticipated for ionic mobility. However, the development of fundamental structure–property relationships for ionic conduction in conjugated polymers has lagged behind that for electrical charge transport.

The mechanism of ionic transport in conjugated polymers is spatially, temporally, energetically, and chemically complex. Multiple processes underlie the mass transport and chemical reaction of a mobile-charged species with a conjugated macromolecular solid. Additionally, the polymeric matrix reorganizes during charging and discharging.

Some of the processes contributing to ionic transport in conjugated polymers are listed below. Each process has its own dynamics, but may be coupled to rates of other process. Additionally, these rates can depend on the concentration of ions incorporated into the polymer.

- Changes in ion concentration are driven by chemical potential gradients. The gradients result from differences in applied electrical potential and ionic concentration, producing the drift and diffusion of ions, respectively.
- Redox reactions occur between the ions and the polymer, changing the charge state of the backbone.
- New electronic energy states emerge in the DOS diagram for the polymer, such as the introduction of polaronic and bipolaronic states between the HOMO and LUMO bands [1, 2, 5].
- The newly created states are localized and have molecular level representations, such as the chemical structure of a polaron [16], as shown in Fig. 5.1a.

https://doi.org/10.1515/9781501524615-005

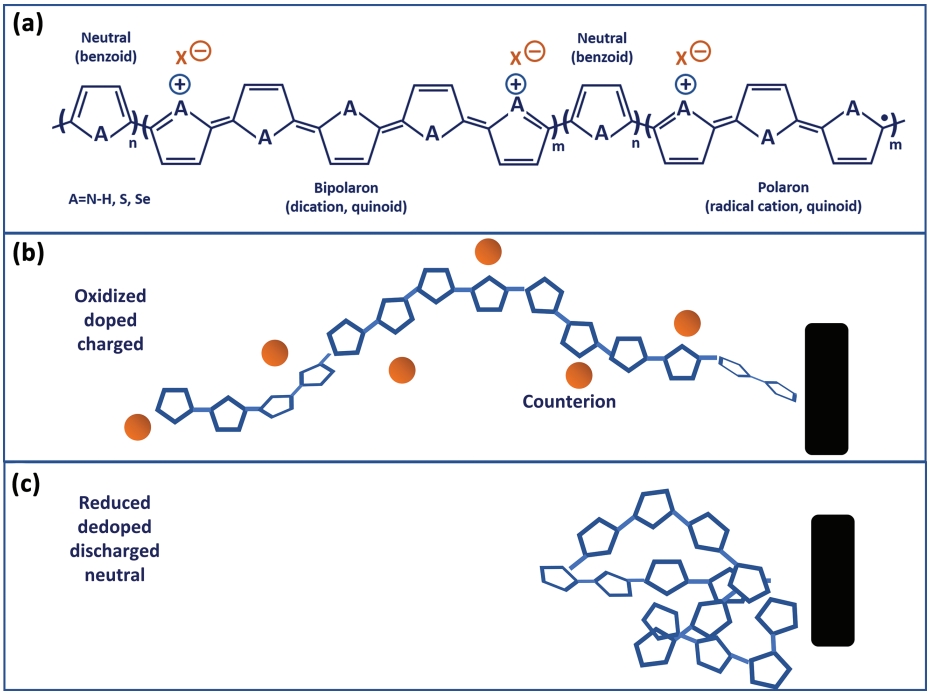


**Fig. 5.1:** (a) The chemical structure of a partially oxidized (doped) generic conjugated chain (Section 5.1), having neutral segments in between localized bonding states corresponding to polaronic and bipolaronic charge carriers. The neutral segments are in the benzoid state, while the oxidized segments display quinoid bonding. Schematics of conjugated polymer chain adjacent to an electrode (black) in the (b) partially oxidized state and in the (c) fully reduced state. In (a) and (b), counterions, shown in orange, are associated with oxidized monomer units.

- Local structural reorganization of the backbone configuration occurs, such as conversion of a benzoid structure in the undoped polymer to a quinoid configuration upon doping (Fig. 5.1a).
- The localized charge carrier states can migrate along the backbone. Intrachain hopping occurs between occupied and unoccupied sites [1, 5]. The migration rate of bipolarons may differ from that of polarons [17].
- One-electron transfer occurs between chains by a hopping mechanism. This interchain transfer is often the rate limiting step, as intrachain charge transport is typically significantly faster [1, 5].
- Electrostatic forces increase as more ions intercalate into the film.
- The overall conformation of the polymer chain becomes more extended in order to minimize electrostatic repulsion between like charges (Fig. 5.1b).
- Redox reactions between chains can form interchain complexes in the solid polymer matrix during charging that relax during discharging [1, 2].

- The electrochemical processes and their dynamics may differ in the order and disorder regions of the conjugated polymer [1, 3, 18].
- The conformation changes in the chains can alter the morphology of the semicrystalline polymer [3, 5, 18].
- In the presence of a solution of an electrolyte and solvent, charge transfer can occur to the interface of the conjugated polymer [3, 19].
- The electrolyte solution can macroscopically swell the conjugated polymer. The swelling results from the intercalation of the redox-active component and solvent molecules into the macromolecular matrix.
- The conjugated polymer can also react with the electrolyte solution.

Changes in polymer morphology or chemical structure which are irreversible represent sources of degradation of the electrochemical performance of the polymer.

The swelling of polymer layers is a complex phenomenon [20]. The simplest case is Type I diffusion, where **Fick's law** is applied. In this case, a gradual concentration profile of the diffusing species exists throughout the thickness of the polymer layer. In contrast, a steep drop in concentration, known as diffusion front, is characteristic of Type II behavior. For a Type II process, the first molecules slowly diffuse into the polymer and create an expanded matrix, allowing the subsequent molecules to follow more quickly. The result is that concentration of the diffusing species is high between the interface and the diffusion front, dropping sharply down to zero between the diffusion front and the substrate. As diffusion proceeds, the position of the diffusion front advances closer to the substrate.

Some of the same processes underlying the electrochemistry of conjugated polymers also occur in related classes of materials. For instance, some inorganic ceramics display a MIEC mechanism [21]. These materials do not have the complexities associated with macromolecular conformational changes. The label of MIEC has also been adopted for conjugated polymers [10, 22, 23]. In contrast, polymer morphology is an important consideration for ion uptake by dielectric polymers. For these organic insulators, the coupling to the electronic energy states is typically unimportant. One example of ion transport in dielectric polymers are the nonporous active layers in the membranes used reverse osmosis for desalinating water [24]. Another example is polymeric ionic selective electrodes [25].

Of course, the size and nature of the ion is also critically important. As introduced in Section 1.3, conjugated polymers can complex with different types of ions, ranging from small monoatomic anions like $Cl^-$, $Br^-$, or $I^-$ to large macromolecular polyanions, such as multiple ionized poly(styrene sulfone) (PSS). As will be discussed further in Section 5.4, molecular ions can have specific interactions with polymeric matrix [17, 26]. Treatment in acids or electrochemical cycling in an electrolyte solution can result in exchange of the counterion species, sometimes referred to as secondary doping [27].

The first section of this chapter discusses the fundamentals of the electrochemistry of conjugated polymers, including their relationship with other MIEC materials. Then, ionic transport is considered from the perspective of the morphology of the polymer–dopant complex. The final section focuses on pseudocapacitance and the importance of nanoscale structures to high-rate energy storage applications.

## 5.1 Redox reactions: doping and dedoping

As introduced in Chapter 1, the doping of p-type conjugated polymers occurs by oxidation. The doping of the neutral polymer can be achieved by chemical reaction with an oxidant. Figure 5.1a shows a partially doped conjugated polymer chain, showing neutral and doped segments. The bonding in these segments corresponds to benzoid and quinoid, respectively. Two types of charge carriers are shown: a polaron (radical cation) and a bipolaron (dication). Electron spin resonance (ESR) spectroscopy detects the spin-1/2 polaron, but not the spin zero bipolaron [2, 5].

The doped p-type polymer is polycationic, where each cationic monomer unit is associated with a negatively charged counterion, thus maintaining charge neutrality. The requirement to maintain charge neutrality, inherently couples the migration rate of an anion during electrochemical doping and dedoping to the mobility of the accompanying electron [28]. Figure 5.1a shows the case of full integer charge transfer (ICT) ) between the monomer and the oxidant. For some molecular counterions, only partial charge transfer occurs, resulting in the formation of a charge transfer complex (CTX) between the host polymer and dopant [5, 29–31].

In Fig. 5.1a, the monomeric unit is a five-member ring representing the generic structure for the unsubstituted conjugated polymers poly(pyrrole) (PPy, A = N-H)), poly(thiophene) (PT, A = S), and poly(selenophene) (PSe, A = Se) [16]. The substituted versions of these polymers also possess the same backbone structure. Poly(3,4-ethylenedioxythiophene) (PEDOT) and poly(3,4-propylenedioxythiophene) (PProDOT) are two examples of 3,4-substituted polythiophenes [32]. Figure 2.1a shows the structure of PEDOT, where a six-membered ring containing two oxygen atoms is backbonded to the thiophene ring of the main polymer chains. The structure of PProDOT is similar to PEDOT, an additional methylene group ($-CH_2-$), creating a seven-membered backbonded ring. As will be discussed in Section 5.4, one of the most studied three-substituted poly(thiophenes) is poly(3-hexyl thiophene) (P3HT).

Other conjugated polymers having low molecular weight monomeric units include poly(*p*-phenylene) and poly(phenylenevinylene). The corresponding chemical formulas are $(-C_6H_4-)_n$ and $(-C_6H_4-CH=CH-)_n$, respectively. Poly(aniline) (PANI) [13, 15] also has a small monomeric repeat unit. The water solubility of PANI makes it one of the most studied conjugated polymers. Fully reduced PANI has the formula $(-C_6H_4-NH-)_n$; it is known as leucoemeraldine and has a yellow color. Fully oxidized PANI has the formula $(-C_6H_4-N-)_n$; it is known as pernigraniline and has a blue

color, corresponding to its smaller bandgap. Emeraldine is the half-oxidized state of PANI, named for its green color. Doping results in polaronic emeraldine, the most electronically conductive form of PANI.

The observation of maximum ionic conductivity at a 50% doping level for PANI is also observed in many other conjugated polymers [1]. High ionic conductance is maintained on a broad plateau around the 50% doping level. Typically, doping levels between 0.1 and 0.5 are utilized [2]. At either very low or very high doping levels, the ionic conductivity is low. Thus, initiating an electrochemical process is slow unless the polymer is already doped. These observations agree with the hypothesis of an ion transporting from an occupied state to an unoccupied one. The corresponding rate will be proportional to the product of the concentrations of the occupied and the unoccupied states.

The doping process can also be driven electrochemically by applying an external electric field to a conjugated polymer film in contact with an electrolyte. In the doped state, the polymer chains often adopt an extended conformation in order to reduce the repulsions between similar charges (Fig. 5.1b). Lowering the magnitude of the applied field causes reduction of the polycationic polymer chain and expulsion of the counterions into the electrolyte. This discharging step results in dedoping. Reduced polymer chains often adopt a compact conformation (Fig. 5.1c).

## 5.2 Ionic drift, diffusion, and mobility

Ionic conduction in MIEC materials is often described by the **Nernst–Planck** drift-diffusion model [5, 33]. This model predicts the ionic flux, $\overrightarrow{N_j}$, which is moles of ions passing across a given area of surface in a fixed time interval and has units of mol/cm$^2$/s. The calculated flux depends both on the electrochemical gradient potential, $\vec{\nabla}\mu_j$, and the convective velocity, $\vec{v}$ according to the equation:

$$\overrightarrow{N_j} = -\frac{D_j c_j}{RT}\vec{\nabla}\mu_j + c_j\vec{v} \tag{5.1}$$

where $D_j$ is the diffusion coefficient of species $j$, $c_j$ is the concentration of species $j$, $R$ is the ideal gas constant, and $T$ is the absolute temperature. The electrochemical driving force results in the concentration gradient of species $j$, as well as the gradient in applied electrostatic potential, $\vec{\nabla}\phi$ as given by

$$\vec{\nabla}\mu_j = RT\vec{\nabla}\ln c_j + z_j F\vec{\nabla}\phi \tag{5.2}$$

where $F$ is the Faraday's constant and $z_j$ is the charge of species $j$. In the absence of convection ($\vec{v} = 0$) and an applied electric field ($\vec{\nabla}\phi = 0$), the Nernst–Planck model reduces to Fick's law of diffusion.

The diffusivity, $D_j$, and mobility, $\mu_j$, of an ion are considered to be related by the **Nernst–Einstein** equation:

$$\mu_j = \frac{F|z_j|D_j}{RT} \tag{5.3}$$

## 5.3 Interfacial charge transfer

The majority of electrochemical applications for conjugated polymers require charge transfer across their interface with an electrolyte. Electrolytes contain a redox-active species, most commonly either in the form of a pure liquid or in a liquid solution with a solvent. However, there is also considerable interest in solid-phase electrolytes.

The rate of interfacial charge transfer for semicrystalline conjugated polymers has been analyzed using the **Marcus–Gerischer** model [5, 19]. Electronic tunneling (i.e., hopping) is assumed to occur between the electrode and the redox-active species in the electrolyte. The calculated tunneling current depends on the effective density of states (DOS) for the ion-intercalated conjugated polymer. The occupancy of the polymer's DOS is changed by sweeping the applied potential. The calculated tunneling current also depends on the DOS and the reorganization energy due to charge transfer (Section 4.5) for redox-active species in the electrolyte.

## 5.4 Electrochemical characterization

**Cyclic voltammetry** is a widely utilized electrochemical characterization method [1, 2, 5, 34, 35]. While the applied voltage increases at a fixed scan rate, ions move from the electrolyte into the polymer film, producing a measurable current. Reversing the voltage sweep causes the migration of ions back out of the film, dedoping the polymer. The electrochemical window is the voltage range over which significant current is observed. Variations in the cyclic voltammogram data often occurs over the first few cycles, known as a conditioning period, after which steady-state behavior is observed.

The scan rate used for cyclic voltammetry determines the duration available for ionic transport to occur. Slow scan rates can provide sufficient time for fully doping and dedoping the polymer. When full doping and dedoping occur reversibly, the peak current is proportional to the scan rate [35]. Thicker films and larger ions require very slow scan rates for complete doping and dedoping. Scan rates that are too high lead to a diffusion control regime, where the peak current becomes proportional to the square root of the scan rate, and shifts in peak position occur as the scan rate changes.

Galvanostatic measurements (i.e., constant current measurements) can be used to determine the fraction of monomer units which are doped [28]. Cyclic voltammetry has been combined with a suite of high-resolution microscopy and spectroscopy methods to examine spatially heterogeneous conjugated polymer electrodes [36].

**Electrochemical impedance spectroscopy (EIS)** is another standard method to investigate electrochemical reaction mechanisms and kinetics at interfaces [37]. The complex impedance is measured as a function of frequency. The resulting impedance spectra are commonly displayed as Nyquist and Bode plots and modeled as an equivalent electrical circuit. The impedance response is interpreted in terms of physical process such as charge transfer, mass transport, surface adsorption, and chemical reactions. A number of conjugated polymers have been characterized by EIS including P3HT [19] and PEDOT [22].

More recently, energy-resolved EIS (ER-EIS) has been used to measure the DOS of organic films [38, 39]. The DOS function, $g(E)$, was introduced in Chapter 1, and for a given band of energy states, often approximated as a Gaussian distribution (eq. (1.1)). The ER-EIS method has broad applicability to conjugated polymers and their blends. The measured DOS functions confirm that the center of both the HOMO and LUMO bands are well represented as Gaussian functions with a standard deviation of $\sigma_{DOS}$. Furthermore, the DOS of the interface and bulk can be differentiated.

The ER-EIS measurements reveal sharper Gaussian bands than observed by photoemission measurements [38]. The $\sigma_{DOS}$ values for the HOMO band of P3HT were 63 and 255 meV by ER-EIS and photoemission, respectively. The higher value determined by photoemission is not consistent with the charge carrier mobility calculated by the Gaussian disorder model (eq. (1.1)). Interfacial charge carrier scattering may be responsible for the broader photoemission value [39].

## 5.5 Polymer morphology and texture

Analogous to the effects of polymer morphology on electronic (Chapter 3) and optical (Chapter 4) properties, the order and orientation of semicrystalline polymers is also anticipated to influence ionic transport. Variations in ion diffusivity are most likely present between the crystalline domains [1, 3] and the amorphous regions which surround them. The role of tie chains, proposed based on electrical conductivity behavior, has not yet received as much attention in the discussion of ionic transport. The texture of crystallites relative to the substrate is anticipated to produce anisotropy in ionic diffusivity. As the dopant level varies, changes in electrostatic forces and the associated changes in polymeric chain conformation will also impact ionic diffusivity.

Counterion size and preferential semicrystalline polymeric texture both impact ionic transport. Figure 5.2a shows the cyclic voltammograms for three PEDOT films obtained using the electrolyte lithium hexafluorophosphate ($LiPF_6$) [28]. The scan

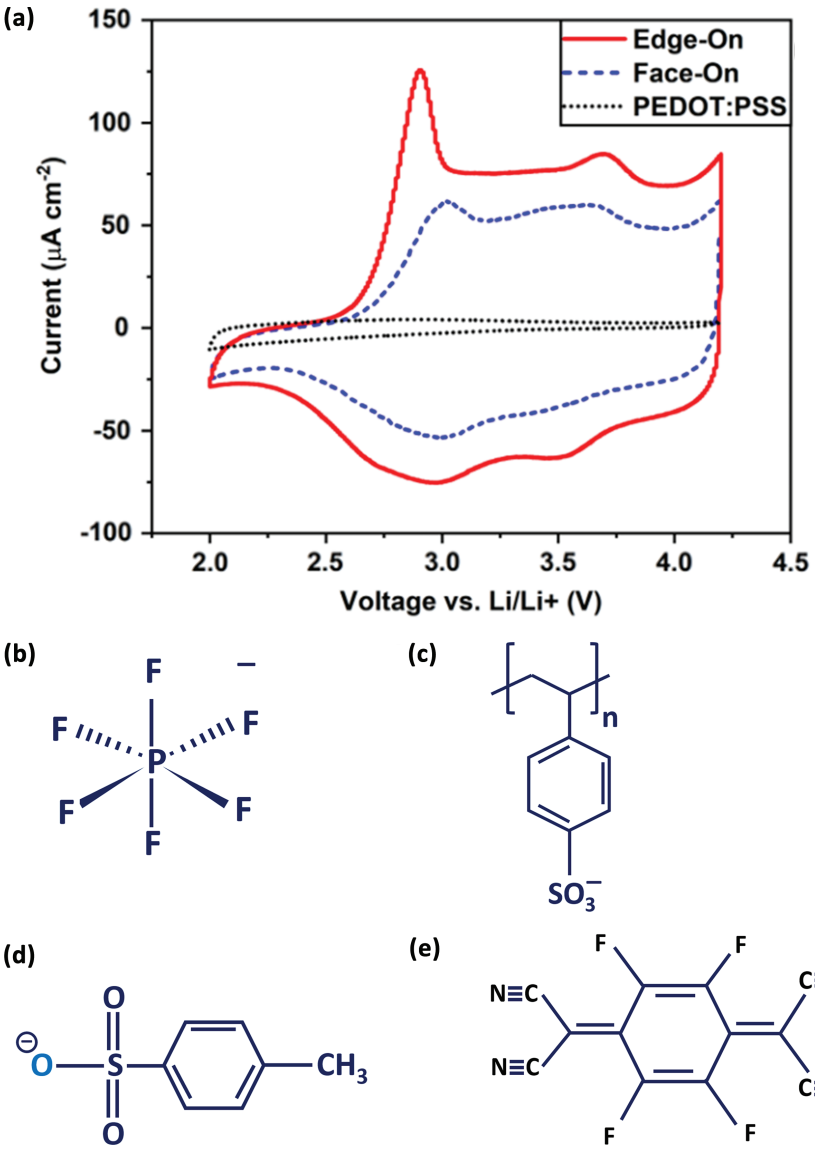


**Fig. 5.2:** (a) Cyclic voltammograms for PEDOT:PSS (black dotted line) and PEDOT: hexafluorophosphate, having edge-on (red solid line) and face-on (blue dashed line) texture with respect to the substrate. Chemical structures of some negatively charged molecular counterions demonstrated as dopants for PEDOT: (b) hexafluorophosphate, (c) tosylate, and (d) poly(styrene sulfone) (PSS). (e) Chemical structure of the molecular dopant 2,3,5,6-tetrafluoro-7,7,8,8-tetracyanoquinodimethane ($F_4TCNQ$), commonly utilized with P3HT and other conjugated polymers having alkyl substituents (Fig. 4.3). (a) Reprinted with permission from P. Moni et al. ACS Appl. Energy Mater. 1, 7093 (2018) copywrite 2018 American Chemical Society.

for the PEDOT:PSS in Fig. 5.2a displays virtually no electrochemical response because PSS is a large macromolecular polyanion, and thus has slow kinetics for exchanging out of the PEDOT matrix. The electrochemical behavior of PEDOT:PSS has been modeled as a two-phase system consisting of PEDOT-rich and PSS-rich domains [40].

Figure 5.2a also shows significant currents for both edge-on and face-on textured PEDOT films. As synthesized, both films contained the monoatomic anion, $Cl^-$. Prior to the cyclic voltammetry measurement shown, multiple voltage sweep cycles were carried out in the $LiPF_6$ electrolyte, resulting in exchange of $Cl^-$ by the molecular ion $PF_6^-$. Thus, the observed currents in Fig. 5.2a for the edge-on and face-on textured PEDOT result from the mobility of the $PF_6^-$ anions. At high-cycling rates, the capacity achievable in both the face-on and the edge-on film was determined to be limited by the mobility of the $PF_6^-$ ion. The largest current is associated with the film having edge-on texture, where the highest doping level reached was 72% of the monomer units. The corresponding value for the face-on textured film was 30%.

The redox reactions of neutral PEDOT to form polarons (radical cations) and bipolarons (dications) are as follows:

$$\mathrm{PEDOT}^0 + \mathrm{PF}_6^- \leftrightarrow \left[\mathrm{PEDOT}^+ \mathrm{PF}_6^-\right] + \mathrm{e}^- \tag{5.4}$$

and

$$\left[\mathrm{PEDOT}^+ \mathrm{PF}_6^-\right] + \mathrm{PF}_6^- \leftrightarrow \left[\mathrm{PEDOT}^+ 2\mathrm{PF}_6^-\right] + \mathrm{e}^- \tag{5.5}$$

Interchain redox reactions in the solid state may also reversible form and relax intermolecular complexes such as σ-dimers [1, 2]. The precise assignment of peaks observed in a cyclovoltammogram, such as shown in Fig. 5.2a, to a specific redox process structure remains a source of debate [2]. In the classical model, low doping levels produce polarons, and higher doping levels result in bipolarons. This model assumes an ideal isolated polymer chain of infinite length. Real polymers experience interchain interactions and are of finite molecular weight. Density functional theory (DFT) calculations suggest that in some cases bipolarons can form a low doping levels, particularly when the polymeric backbone contains larger fused ring structures [17]. The DFT results also suggest that in some cases polarons and bipolarons can coexist at some doping levels [41, 42].

Using an aqueous solution of potassium chloride as the electrolyte and PEDOT:Cl films of differing initial texture produced cyclic voltammograms, where the measured current reflects the mobility of the $Cl^-$ ion [3, 18]. A trade-off was noted between ionic conductivity and electrical conductivity. It is important to consider that the ionic conductivity was measured out-of-plane, while the electrical conductivity is evaluated in-plane. The highest ionic conductivity was observed for the edge-on texture, where the conjugated planes are perpendicular to the substrate (Fig. 2.2b) [3].

Thus, the edge-on texture would be expected to have high out-of-plane conductivity. Indeed, direct measurement of the out-of-plane conductivities for PEDOT confirmed higher values of the edge-on as compared to the face-on textured polymer [43]. Therefore, out-of-plane ionic and electronic conductivity may be correlated, as would be anticipated by the constraint of maintaining charge neutrality.

The first cycle contained an intense oxidation peak at ~118 meV, which was assigned to the irreversible uptake of anions by the ordered domains. This conditioning effect was most pronounced in thinner PEDOT layers, ~20 nm thick. A similar relaxation of the more compact ordered domains was observed in P3HT [44]. In subsequent cycles, successively less uptake of the $Cl^-$ anion occurred, until a new steady-state morphology was achieved. The edge-on texture (Fig. 2.2b) may provide a less tortuous path for the intercalation of the $Cl^-$ into the polymer [3, 18], which would be consistent with the observation of higher $PF_6^-$ content for the edge-on texture (Fig. 5.2a) [28].

The molecular dopant 2,3,5,6-tetrafluoro-7,7,8,8-tetracyanoquinodimethane ($F_4$TCNQ) (Fig. 5.2e) has been utilized in P3HT and related conjugated polymers possessing alkyl side chains [26, 45]. The length and local density of the alkyl side chains can affect the lamellar polymer morphology, as well as introducing steric selectivity to complexing with molecular dopants [26]. In a regioregular P3HT, the interpenetrating alkyl chains are regularly spaced, as shown in Fig. 5.3 [5]. The $F_4$TCNQ segregates into the alkyl side chains, contracting the π–π stacking distance [46] in face-on oriented regioregular P3HT crystallites (Fig. 5.3a). Furthermore, face-on orientation was also adopted by the molecular dopant, with the longest dimension of this molecule aligned parallel to the polymer chains.

Regiorandom P3HT forms when the polymerization does not proceed exclusively through heat-to-tail monomer addition. The result is in variation of the local packing density of the alkyl chains. Upon doping with $F_4$TCNQ, amorphous regiorandom P3HT developed an edge-on crystalline texture [47]. The DOS in the ordered regions of P3HT differ from the DOS in the disordered domains. The result is the coexistence of two types of doping, ICT and CPX (Section 5.1) in semicrystalline P3HT. The ICT mechanism is observed in the crystalline domain at the same time the CPX doping is present in the amorphous region [31].

## 5.6 Pseudocapacitance

Electrochemical energy storage can take two forms: electrical double layers reversible adsorbed to surfaces or Faradic charge storage in pseudocapacitive materials [5, 35]. Increasing storage capacity of electrical double layers requires increasing the surface area for adsorption. Many types of porous carbon materials have been investigated as high surface area electrodes [15] for electrochemical double layer capacitors (EDLC). Adding a pseudocapacitive layer to the carbon electrodes represents a second

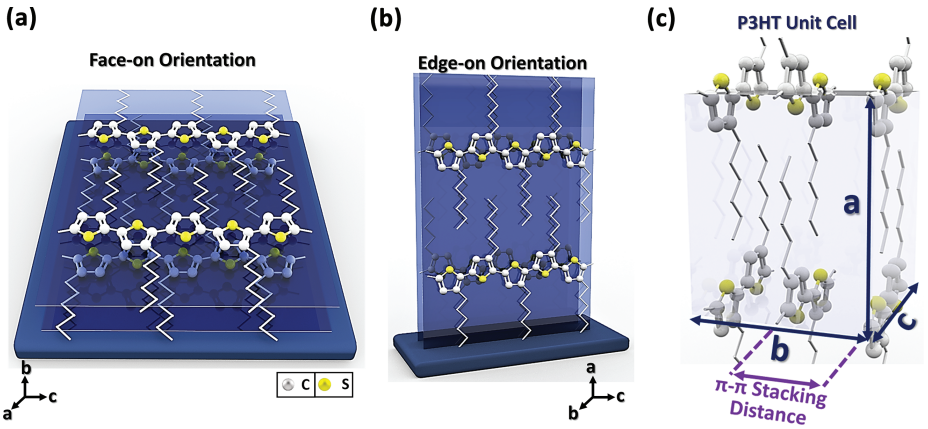


**Fig. 5.3:** For regioregular poly(3-hexyl thiophene) (P3HT), schematics of (a) face-on texture, (b) edge-on texture, and (c) the unit cell. (a–c) Reprinted with permission from Hedari Gharachesheshmeh and Gleason KK, Mater. Today. Adv. 2020, 8, 100086. Copywrite 2020, Elsevier [5].

reservoir for electrochemical charge. The resulting Faradic charge storage results from reversible redox reactions throughout the volume of the pseudocapacitive layer. The increase in total storage capacity is significant, even at layer thicknesses below 10 nm [6].

The reversible doping and dedoping of conjugated polymers is a promising means to achieve pseudocapacitive charge storage with having both high specific energy and high specific power [2, 5, 35]. The maximum theoretically capacitance corresponds to one charge per monomer unit. Thus, the criteria of achieving high specific capacitance, favors polymers having monomer units of low molecular weight, such as PANI, PPy, and poly(thiophene) (Section 5.1). However, there are many additional criteria for the integration of conjugated polymers as pseudocapacitive materials in energy storage devices. These criteria include the width of potential window for electrochemical operation, high thermal and chemical stability, high charge mobility, and high electrical conductivity and can lead the selection of conjugated polymers synthesized from higher molecular weight monomers, such as poly(3-methylthiophene) (P3MT) and PEDOT [6]. Repeated cycles of expansion and contraction upon doping and dedoping (Fig. 5.1b and c) creates mechanical stress that has proven to be a source of instability for conjugated polymers integrated into electrochemical energy storage devices [2, 35].

High surface area remains important for pseudocapacitive charge storage. For a fixed volume of polymer, thinner layers over higher interfacial areas increase the rate of charging and discharging. The ionic diffusion time, $\tau$, increases as the square of layer thickness, $L$, as follows:

$$\tau = \frac{L^2}{D_{\text{ion}}} \tag{5.6}$$

where $D_{ion}$ is the diffusivity of the ion in units of $cm^2/s$. Thus, a 10 nm thick layer will have a million-fold faster rate of discharge as compared to a 10 μm thick layer [48]. Indeed, the nanopatterning of conjugated polymers successfully decreases their electrochromic switching time [49].

Numerous conjugated polymers including PANI, PPy, PEDOT, and P3MT ultrathin (<20 nm thick) layers have been conformally grown over nanostructured electrodes [6, 50]. The ultimate goal is to achieve high-rate energy storage that simultaneous provides 1) the high charge storage capacity of traditional batteries and 2) the high charging and discharging currents associated with supercapacitors. The mechanical flexibility of the conjugated polymers is an additional motivation, enabling both the fabrication of flexible and wearable devices and compatibility with economical roll-to-roll manufacturing. For ultrathin layers, the overall charge storage may have significant contribution from both the electrical double layer and pseudocapacitance mechanisms [18]. The use of ultrathin layers also minimizes complications arising from ionic transport limitations in the solid.

Using a high-surface-area support also maintains a small areal footprint for an energy storage device. Various types of nano- and meso-porous carbons have been used as scaffolds and nanocomposite fillers for conjugated polymer pseudocapacitive layers [15]. In addition to increasing the interfacial area, the porous carbon increases the lateral conductivity required to efficiently transport charge across the macroscopic footprint of the storage device.

Nanostructures in conjugated polymers can be the result of templating and direct-writing processes [1] or be a direct result from the synthesis method [51]. The morphologies achieved include 3D nanoporous structures, 2D nanoplates, and high aspect ratio 1D nanofibers, nanowires, and nanotubes. As anticipated from eq. (5.6), the low characteristic dimensions of nanostructures result in faster charge transfer rates as measured by cyclic voltammetry [1, 35]. Higher specific capacitance has also been observed in nanostructured conjugated polymers [5, 35], perhaps indicating that full doping can be achieved during the scan period. Additionally, the nanostructures can relieve mechanical stress resulting from the volumetric changes due to doping and dedoping, thereby increasing cycling stability.

## References

[1] Heinze J, Frontana-Uribe BA, Ludwigs S. Electrochemistry of conducting polymers-persistent models and new concepts. Chem Rev 2010, 110, 4724–4771.

[2] Ibanez JG, Rincón ME, Gutierrez-Granados S, Chahma M, Jaramillo-Quintero OA, Frontana-Uribe BA. Conducting polymers in the fields of energy, environmental remediation, and chemical-chiral sensors. Chem Rev 2018, 118, 4731–4816.

[3] Heydari Gharahcheshmeh M, Wan CT-C, Gandomi YA, et al. Ultrathin conformal oCVD PEDOT coatings on carbon electrodes enable improved performance of redox flow batteries. Adv Mater Interfaces 2020, 7, 2000855.

[4] Gleason KK. Nanoscale control by chemically vapour-deposited polymers. Nat Rev Phys 2020, 2, 347–364.
[5] Heydari Gharahcheshmeh M, Gleason KK. Texture and nanostructural engineering of conjugated conducting and semiconducting polymers. Mater Today Adv 2020, 8, 100086.
[6] Heydari Gharahcheshmeh M, Gleason KK. Device fabrication based on oxidative chemical vapor deposition (oCVD) synthesis of conducting polymers and related conjugated organic materials. Adv Mater Interfaces 2019, 6, 1801564.
[7] Mirabedin M, Vergnes H, Caussé N, Vahlas C, Caussat B. An out of the box vision over oxidative chemical vapor deposition of PEDOT involving sublimed iron trichloride. Synth Met 2020, 266, 116419.
[8] Simon DT, Gabrielsson EO, Tybrandt K, Berggren M. Organic bioelectronics: Bridging the signaling gap between biology and technology. Chem Rev 2016, 116, 13009–13041.
[9] Ram J, Singh RG, Singh F, et al. Ion beam engineering in WO3-PEDOT: PSS hybrid nanocomposite thin films for gas sensing measurement at room temperature. Inorg Chem Commun 2020, 119, 108000.
[10] Berggren M, Crispin X, Fabiano S, et al. Ion electron–coupled functionality in materials and devices based on conjugated polymers. Adv Mater 2019, 31, 1805813.
[11] Esser B, Dolhem F, Becuwe M, Poizot P, Vlad A, Brandell D. A perspective on organic electrode materials and technologies for next generation batteries. J Power Sources 2021, 482, 228824.
[12] Friedlein JT, McLeod RR, Rivnay J. Device physics of organic electrochemical transistors. Org Electron 2018, 63, 398–414.
[13] Argun AA, Aubert PH, Thompson BC, et al. Multicolored electrochromisin in polymers: Structures and devices. Chem Mater 2004, 16, 4401–4412.
[14] Hu F, Xue Y, Xu J, Lu B. PEDOT-based conducting polymer actuators. Front Robot AI 2019, 6, 114.
[15] Liu P, Yan J, Guang Z, Huang Y, Li X, Huang W. Recent advancements of polyaniline-based nanocomposites for supercapacitors. J Power Sources 2019, 424, 108–130.
[16] Bilger D, Homayounfar SZ, Andrew TL. A critical review of reactive vapor deposition for conjugated polymer synthesis. J Mater Chem C 2019, 7, 7159–7174.
[17] Voss MG, Challa JR, Scholes DT, et al. Driving force and optical signatures of bipolaron formation in chemically doped conjugated polymers. Adv Mater 2021, 33, 2000228.
[18] Arnold SP, Harris JK, Neelamraju B, Rudolph M, Ratcliff EL. Microstructure-dependent electrochemical properties of chemical-vapor deposited poly(3,4-ethylenedioxythiophene) (PEDOT) films. Synth Met 2019, 253, 26–33.
[19] Rudolph M, Ratcliff EL. Normal and inverted regimes of charge transfer controlled by density of states at polymer electrodes. Nat Commun 2017, 8, 1048.
[20] Mari-buye N, Shaughnessy SO, Colominas C, Semino CE, Gleason KK, Borros S. Functionalized Swellable hydrogel layers as a platform for cell studies. Adv Funct Mater 2009, 19, 1276–1286.
[21] Jin X, White RE, Huang K. Simulating charge transport in solid oxide mixed ionic and electronic conductors: Nernst-Planck theory vs Modified Fick's law. J Electrochem Soc 2016, 163, A2702–A2719.
[22] Reynolds JR, Thompson BC, Skotheim TA, et al. Electric transport properties in PEDOT thin films. In: Conjugated Polymers. 2019, 45–128.
[23] Paulsen BD, Tybrandt K, Stavrinidou E, Rivnay J. Organic mixed ionic–electronic conductors. Nat Mater 2020, 19, 13–26.
[24] Kamcev J, Freeman BD. Charged polymer membranes for environmental/energy applications. Annu Rev Chem Biomol Eng 2016, 7, 111–133.

[25] Bobacka J, Ivaska A, Lewenstam A. Potentiometric ion sensors. Chem Rev 2008, 108, 329–351.
[26] Kohno S, Yamashita Y, Kasuya N, et al. Controlled steric selectivity in molecular doping towards closest-packed supramolecular conductors. Commun Mater 2020, 1, 79.
[27] Itoh K, Kato Y, Honma Y, et al. Structural alternation correlated to the conductivity enhancement of PEDOT:PSS films by secondary doping. J Phys Chem C 2019, 123, 13467–13471.
[28] Moni P, Lau J, Mohr AC, et al. Growth temperature and electrochemical performance in vapor-deposited Poly(3,4-ethylenedioxythiophene) thin films for high-rate electrochemical energy storage. ACS Appl Energy Mater 2018, 1, 7093–7105.
[29] Arvind M, Tait CE, Guerrini M, et al. Quantitative analysis of doping-induced polarons and charge-transfer complexes of Poly(3-hexylthiophene) in solution. J Phys Chem B 2020, 124, 7694–7708.
[30] Jacobs IE, Moulé AJ. Controlling molecular doping in organic semiconductors. Adv Mater 2017, 29, 1703063.
[31] Neelamraju B, Watts KE, Pemberton JE, Ratcliff EL. Correlation of coexistent charge transfer states in F 4 TCNQ-doped P3HT with microstructure. J Phys Chem Lett 2018, 9, 6871–6877.
[32] Groenendaal B, Jonas F, Freitag D, Pielartizk H, Reynolds JR. Poly(3,4-ethylenedixoythiophene) and its derivatives: Past, present, and future. Adv Mater 2000, 12, 481–494.
[33] Sokalski T, Lingelfelter P, Lewenstam A. Numerical solution of the coupled Nernst-Planck and Poisson equations for liquid junction and ion selective membrane potentials. J Phys Chem B 2003, 107, 2443–2452.
[34] Elgrishi N, Rountree KJ, McCarthy BD, Rountree ES, Eisenhart TT, Dempsey JL. A practical beginner's Guide to cyclic voltammetry. J Chem Educ 2018, 95, 197–206.
[35] Le TH, Kim Y, Yoon H. Electrical and electrochemical properties of conducting polymers. Polymers (Basel) 2017, 9, 150.
[36] Daviddi E, Chen Z, Beam Massani B, et al. Nanoscale visualization and multiscale electrochemical analysis of conductive polymer electrodes. ACS Nano 2019, 13, 13271–13284.
[37] Hernández HH, Reynoso AMR, González Jct, et al. Electrochemical Impedance Spectroscopy (EIS): A review study of basic aspects of the corrosion mechanism applied to steels. In: IntechOpen. 2020.
[38] Schauer F. Electronic structure spectroscopy of organic semiconductors by energy resolved-electrochemical impedance spectroscopy (ER-EIS). J Appl Phys 2020, 128, 150902.
[39] Bässler H, Kroh D, Schauer F, Nádaždy V, Köhler A. Mapping the density of states distribution of organic semiconductors by employing energy resolved–electrochemical impedance spectroscopy. Adv Funct Mater 2020, 2007738.
[40] Volkov A V., Wijeratne K, Mitraka E, et al. Understanding the capacitance of PEDOT:PSS. Adv Funct Mater 2017, 27, 1700329.
[41] Liang Z, Choi HH, Luo X, et al. N-type charge transport in heavily P-doped polymers. Nat Mater 2021, 20, 518–524.
[42] Pak K, Choi J, Lee C, Im SG. Low-power, flexible nonvolatile organic transistor memory based on an ultrathin bilayer dielectric stack. Adv Electron Mater 2019, 5, 1800799.
[43] Wang X, Zhang X, Sun L, et al. High electrical conductivity and carrier mobility in oCVD PEDOT thin films by engineered crystallization and acid treatment. Sci Adv 2018, 4, eaat5780.
[44] Giridharagopal R, Flagg LQ, Harrison JS, et al. Electrochemical strain microscopy probes morphology-induced variations in ion uptake and performance in organic electrochemical transistors. Nat Mater 2017, 16, 737–742.

[45] Harris JK, Ratcliff EL. Ion diffusion coefficients in poly(3-alkylthiophenes) for energy conversion and biosensing: Role of side-chain length and microstructure. J Mater Chem C 2020, 8, 13319–13327.
[46] Nagamatsu S, Pandey SS. Ordered arrangement of F4TCNQ anions in three-dimensionally oriented P3HT thin films. Sci Rep 2020, 10, 20020.
[47] Yee PY, Scholes DT, Schwartz BJ, Tolbert SH. Dopant-induced ordering of amorphous regions in regiorandom P3HT. J Phys Chem Lett 2019, 10, 4929–4934.
[48] Chen N, Reeja-Jayan B, Lau J, et al. Nanoscale, conformal polysiloxane thin film electrolytes for three-dimensional battery architectures. Mater Horizons 2015, 2, 309–314.
[49] Neo WT, Li X, Chua SJ, Ling Chong KS, Xu J. Enhancing the electrochromic performance of conjugated polymers using thermal nanoimprint lithography. RSC Adv 2017, 7, 49119–49124.
[50] Lv H, Pan Q, Song Y, Liu XX, Liu T. A Review on nano-/microstructured materials constructed by electrochemical technologies for supercapacitors. Nano-Micro Lett 2020, 12, 118.
[51] Li X, Rafie A, Smolin YY, Simotwo S, Kalra V, Lau KKS. Engineering conformal nanoporous polyaniline via oxidative chemical vapor deposition and its potential application in supercapacitors. Chem Eng Sci 2019, 194, 156–164.

# 6 Thermal transport

The thermal transport properties of conjugated polymers, combined with their other attractive characteristics, open up new opportunities in energy harvesting and localized thermal management by efficient heating and cooling [1–6]. The quest for sustainable energy has driven interest in thermoelectrical power generation from relatively low-temperature waste heat. Energy harvesting could also reduce or eliminate the need for charging mobile and wearable devices. For implantable devices, such as pacemakers and defibrillators, energy harvesting could obviate battery replacement surgeries. Biocompatible conjugated polymers have been demonstrated for additional thermal applications requiring implantation or injection into the body [7, 8].

Traditional thermoelectric materials offer high performance but are mechanical, brittle inorganics synthesized from less common elements. In contrast, organic thermoelectric (oTE) materials provide mechanical flexibility, which can be exploited in new classes of devices. Additionally, oTEs are composed of nontoxic earth-abundant elements, as desired for large area applications. Traditional thermoelectrics operate at high temperatures, where the intrinsic thermodynamic efficiency for energy capture is high. Less expensive devices are needed to make lower temperature, lower efficiency energy harvesting economically viable. Lower operating temperatures are desirable for capturing waste heat from sources like electric power plants and also for powering wearable devices based on body temperature. The lower anticipated cost of oTEs may enable economical energy harvesting near room temperature.

This chapter will first explore the mechanisms of thermal conduction of dielectric conjugated polymers and its relationship to polymer morphology and nanostructure. Next, the fundamentals of the thermoelectric characteristics of conjugated polymers and their nanocomposites will be discussed. Selected examples of experimentally achieved thermopower using oTEs will be highlighted and compared to that of inorganics. The final section will discuss applications of conjugated properties emerging as a result of their combination of thermal properties and biocompatibility.

## 6.1 Thermal conductivity

### 6.1.1 Isotropic

Mobile charge carriers are responsible for both electrical conduction and heat transport [1, 2]. Indeed, many familiar electrical conductors also exhibit high thermal transport. For example, copper has an electrical conductivity, $\sigma$, of 596,000 S/cm [9] and thermal

https://doi.org/10.1515/9781501524615-006

conductivity, $\kappa$, of 399 W/mK [10].[1] Inorganic semiconductors typically have $\kappa \sim 100$ W/mK [1, 11]. Traditional polymers, such as poly(ethylene) $(\text{-}CH_2\text{-})_n$, are electrical insulators. The low density of mobile charge carriers in dielectric polymers correlates with low values of isotropic thermal conductivity ($\kappa \sim 0.1$–$0.2$ W/mK) [1].

Diamond is a well-known exception to the correlation between the electrical and thermal conductivity of materials. While diamond is electrically insulating, its thermal conductivity is ~5× that of copper. The high thermal conductivity of diamond is a result of phonons (lattice vibrations) of strong carbon–carbon single bonds (~347 kJ/mol), rather than mobile charge carriers.

In general, the thermal conductivity can be considered to have contributions from both the electrical charge carriers and the lattice phonons:

$$\kappa = \kappa_{\text{electronic}} + \kappa_{\text{lattice}} \tag{6.1}$$

For inorganic semiconductors, the electronic component, $K_{\text{electronic}}$, will increase with charge carrier density as given by the **Wiedermann–Franz** law:,

$$\kappa_{\text{electronic}} = L\sigma T \tag{6.2}$$

where $T$ is absolute temperature and $L$ is the **Lorenz number** [12]. For $L$, theoretical **Sommerfeld value**, $L_0$, is given by

$$L_0 = \left(\frac{\pi^2}{3}\right)\left(\frac{k_B}{e}\right)^2 = 2.44 \times 10^{-8}\ \text{W}\Omega\text{K} \tag{6.3}$$

Calculations for conjugated polymers predict $L < L_0$ at low doping levels and $L \sim L_0$ at high doping levels [12]. Indeed, the predictions of eq. (6.2) agreed with data from a series of PEDOT films doped with tosylate, for which the $\sigma$ values ranged from 200 to 500 S/cm [13]. The contribution of $\kappa_{\text{electronic}}$ to the overall value is generally negligible when $\sigma < \sim 1$ S/cm. Thus, for dielectric polymers, heat transfer by phonons dominates so that $\kappa \sim \kappa_{\text{lattice}}$.

Weak interchain interactions through van der Waals forces have been considered a bottleneck for achieving high isotropic values of thermal conductivity in polymers [14]. Both intermolecular hydrogen bonding and cross-linking through covalent bonds have been explored to improve interchain thermal transport by phonons in dielectric polymers.

The strong carbon–carbon double bonds (~610 kJ/mol) present in the backbone structure of conjugated polymers are expected to enhance phonon transport along the chain axis [15]. Additionally, the strong π–π couplings between conjugated macromolecular chains contribute to the higher isotropic thermal conductivity due to charge carrier transport.

**1** Unless otherwise stated, property values reported in this chapter are from room-temperature measurements.

#### 6.1.1.1 Increasing $\kappa$

Thermal conductive polymers are desired as heat spreading materials in electronics and automotive applications [16]. As compared to traditional metallic and ceramic heat spreading materials, polymers are lighter in weight and easier to form into specific geometric shapes.

For a semicrystalline film of undoped poly(3-hexyl thiophene) (P3HT) [14], $\kappa$ = 2.2 W/mK, a value ~10× that of amorphous P3HT [17]. No chain alignment was induced during synthesis or by post-growth processing. Indeed, a random crystallite orientation was observed by GIWAXS analysis, confirming that polymer chain orientation was not the source of the higher $\kappa$ value. Values of $\kappa \sim 2$ W/mK have also been assumed for PEDOT [6].

#### 6.1.1.2 Lowering $\kappa$

As will be discussed in Section 6.2, low values of thermal conductivity are attractive for thermoelectric applications. Several research groups have reported $\kappa \sim 0.3$ W/mK for PEDOT:Tos [18]. For PEDOT:Cl grown with modest conductivity (~1 to 30 S/cm), thermal transport is expected to be dominated by phonons (i.e., a so-called phonon glass) [2], $\kappa \sim 0.16$ W/mK [19]. The 1D confinement produced by P3HT nanowires having a 5 nm × 15 nm cross-section decreased thermal conductivity [17]. Phonon scattering at the boundaries of this nanostructure resulted in a minimum value of $\kappa \sim 0.055$ W/mK.

### 6.1.2 Anisotropy

In the case of anisotropy, **Fourier's law** of heat conduction can be expressed as [18]

$$\rho c_p \frac{\partial T}{\partial t} = \vec{\nabla} \cdot \left( \vec{k} \cdot \vec{\nabla} T \right) \tag{6.4}$$

where $\vec{k}$ is the thermal conductivity, $\rho$ is the mass density, and $c_p$ is the specific heat. The corresponding isotropic value of $\kappa$ is given by

$$\kappa = \frac{1}{3} \mathrm{Tr} \left( \overleftrightarrow{k} \right) = \frac{\kappa_{xx} + \kappa_{yy} + \kappa_{zz}}{3} \tag{6.5}$$

Additionally, the in-plane value, $\kappa_{xy}$, is equal to

$$\kappa_{xy} = \left( \kappa_{xx}^2 + \kappa_{yy}^2 \right)^{1/2} \tag{6.6}$$

For traditionally dielectric polymers, efficient phonon transport occurs along linear polymer chains. Remarkably, the in-chain direction of ultradrawn poly(ethylene) fibers gave $\kappa = 104$ W/mK, ~25% that of copper [20]. Analysis of poly(acetylene) suggested

that the intrinsic in-chain charge carrier transport due to phonons could exceed that of copper [21].

Structural disorders such as nonlinear chain conformations and entanglements are sources of phonon scattering. A reduction in the mean free path of the phonons lowers thermal conductivity. The thermal conductivity of polymers has been improved to a lesser degree by other alignment methods, including mechanical stretching, nanoscale templating, and surface grafting [14].

The difference between intrachain (Section 2.3) versus interchain coupling (Section 2.4) in conjugated polymers is a source of anisotropy for charge carrier mobility. Hence, anisotropy is also expected to be possible in the thermal conductivity of conjugated polymers. For a given polymer, such as PEDOT, film morphology is highly dependent on the synthesis method (Section 2.5), the corresponding dopant, and any postprocessing.

A high degree of anisotropy can be induced by the lamellar structure of PEDOT:PSS, where the dielectric PSS layers aligned parallel to the substrate are expected to inhibit out-of-plane thermal transport. In a single film of PEDOT:PSS, $\kappa_{xy} = 0.84$ and $\kappa_z = 0.15$ W/mK, giving an anisotropy ratio of 5.6:1 [22]. Anisotropy in $\kappa$ has also been reported in other studies of PEDOT:PSS films, but with lower anisotropy ratios [5, 11].

## 6.2 Thermoelectric properties

In a thermoelectric material, a difference in temperature, $\Delta T$, induces the diffusion of charge carriers, which results in an electrical potential difference $\Delta V$. To maintain the required temperature gradient, thermoelectric materials should be poor conductors of heat while simultaneously providing high electrical conductivity.

Using thermoelectric materials, the **Seebeck effect** allows a difference in temperature to be converted to electrical power, while the **Peltier effect** uses power to achieve cooling and efficient heating [6, 23]. Both of these effects have been exploited for solid-state devices (Fig. 6.1), which use pair of p-type and n-type legs for efficient operation [1, 2]. Devices with only a leg of p-type oTEs have also been reported [4]. For p-type conduction, the cold side becomes positively charged. In contrast, the cold side becomes negatively charged for n-type conduction [1, 24]. For increased output, arrays are fabricated by interconnecting identical devices. Stacking the arrays or rolling up flexible arrays reduces the areal footprint of the module.

The **Seebeck coefficient** quantifies the magnitude of the thermoelectric effect in a solid material and is defined as

$$S = \frac{\Delta V}{\Delta T} \tag{6.7}$$

The value of $S$ is also referred to as the **thermopower** and is typical reported in units of μV/K. Multiple procedures have been reported for measuring $S$ [14, 25].

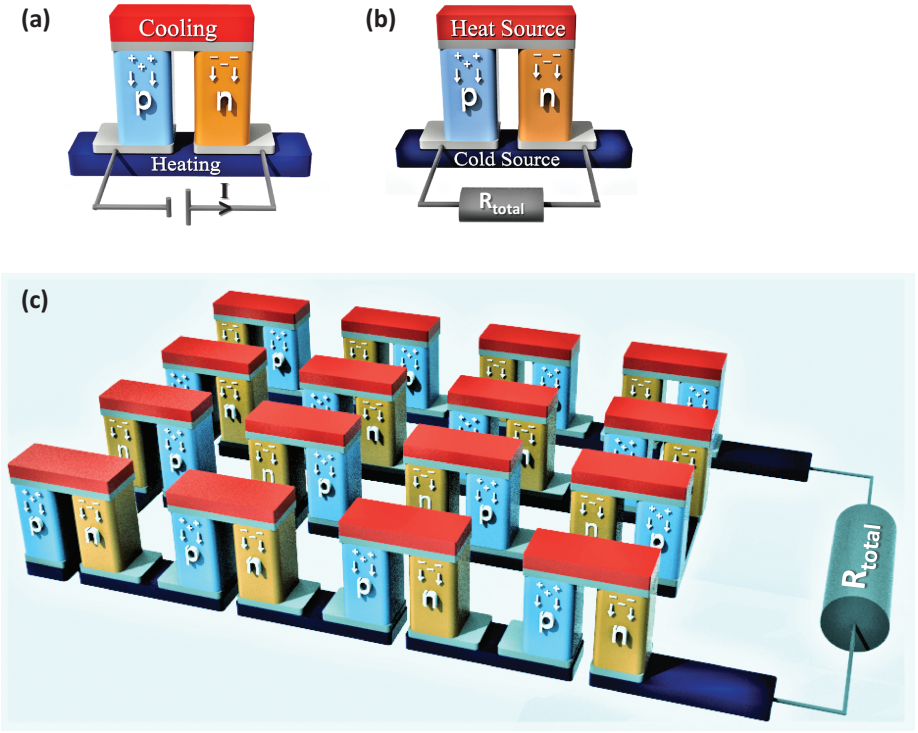


**Fig. 6.1:** Schematics of individual solid-state thermoelectric devices for (a) power generation and (b) localized thermal management (cooling/heating). (c) Arrays of devices increase net output and can be rolled or stacked to produce low-footprint modules.

High electrical conductivity combined with low thermal conductivity leads to high values of $S$.

### 6.2.1 Efficiency

The **Carnot efficiency**, $\eta_c$, is the maximum efficiency for an ideal thermoelectric device and is given by

$$\eta_c = \frac{\Delta T}{T_H} = 1 - \frac{T_C}{T_H} \tag{6.8}$$

where the absolute temperatures are used from both the hot temperature, $T_H$, and the cold temperature, $T_C$. Thus, $\eta_c$ increases for high-temperature operations (i.e., higher values of $T_H$). The ambient surroundings typically provide the cold thermal reservoir, in which case $T_C \sim 300$ K.

The thermal stability of conjugated polymers limits $T_H$ to ~ 500 K [2], corresponding to $\eta_c \sim 0.4$. The Carnot efficiency drops to ~0.03 when $T_H \sim 310$ K, corresponding to human body temperature. No amount of materials optimization can overcome the limits imposed by the second law of thermodynamics.

The thermal properties of real materials further limit the achievable TE efficiency, $\eta_{TE}$, according to the following relationship:

$$\eta_{TE} = \eta_C \left\{ \frac{\sqrt{1+ZT}-1}{\sqrt{1+ZT}+\frac{T_C}{T_H}} \right\} \tag{6.9}$$

The dimensionless thermoelectric figure of merit, $ZT$, is defined as

$$ZT = \frac{S^2 \sigma T}{\kappa} \tag{6.10}$$

where $T$ is the mean operating temperature: $T = (T_H + T_C)/2$. The higher values of $ZT$ increase $\eta_{TE}$, which corresponds to a higher maximum generated electrical power per unit of heat flux.

### 6.2.2 Figures of merit

For inorganic bismuth telluride ($Bi_2Te_3$) and its alloys with antimony, $ZT \sim 1$, while for several types of p-type oTEs $ZT > 0.1$ has been achieved [6, 11]. The nanostructure of inorganic thermoelectrics has been used to control the transport of both electrons and phonons [2, 6]. Using eq. (6.9) for a material with $ZT = 1$, $\eta_{TE} \sim 0.2\eta_C$, and for a material with $ZT = 0.1$, $\eta \sim 0.03\eta_C$. Thus, the modest thermoelectric efficiencies associated with a small $\Delta T$ at low $T_H$ are difficult to overcome by currently available material design strategies.

To determine $ZT$ for an anisotropic material, the same direction of measurement should be used to obtain the values of $S$, $\sigma$, and $\kappa$ [11, 23]. Both $S$ and $\sigma$ are typically measured in plane [2]. However, out-of-plane values for $\kappa$ are measured by both the response to oscillatory heating [19] and time domain thermoreflectance (TDTR) methods [14]. Combining TDTR with measurement of elastic constants allows the determination of in-plane $\kappa$ values [11, 26].

Thermoelectric properties have been reported for numerous conducting polymers including poly(acetylene), poly(thiophene), poly(aniline) (PANI), poly(pyrrole) (PPy), poly(phenylenevinylene), poly(carbazole), and their derivatives [1, 6, 23]. Additionally, conjugated polymers have been combined with a variety of fillers to create nanocomposites for TE applications. Most of the fillers possess either high electrical conductivity such as carbon nanotubes (CNTs), or inorganic thermoelectrics such as $Bi_2Te_3$. Common routes for producing the nanocomposites include polymerization of the monomers in a mixture with the filler, polymerization of the monomer

within a controlled template, and physical mixing [27]. The latter method is commonly used with PANI and PEDOT:PSS.

Since measurements of $\kappa$ have not been routine, the power factor, $S^2\sigma$, which appears in the numerator of eq. (6.10) is an alternate figure of merit used to compare materials instead of $ZT$ [1, 11]. The power factor is also proportional to the power generated fixed device geometry and thermal gradient [28]. Optimization of processing conditions to control polymer morphology and doping levels have resulted in conjugated polymers and polymeric nanocomposites which display room-temperature power factors >100 $\mu W/mK^2$. Selected benchmark values, all in units of $\mu W/mK^2$, are:

- 4800 for $Bi_{0.5}Sb_{1.5}Te_3$ [29];
- 3050 for a multilayer film of PANI, graphene, double-walled CNTs, and PEDOT:PSS [30];
- 1350 for stretched poly(acetylene) doped with iodine [31];
- 800 for solvent-sheared PEDOT:PSS [32];
- 460 for PEDOT:PSS with secondary doping ($ZT \sim 0.42$) [33];
- 324 for PEDOT:Tos at ~25% level of oxidation ($ZT \sim 0.25$) [34];
- 212 for PEDOT:Cl in the face-on orientation and rinsed with HBr acid [35];
- 130 for a PEDOT:PSS/ $Bi_2Te_3$ nanocomposite [36]; and
- 120 for PBTTT(Fig. 4.3) doped with $F_4TCNQ$ [37] (Fig. 5.2e).

For the oTE examples above, nanostructure, polymer chain alignment, or both, are likely significant contributing factors to reach higher power factors. Because both $S$ and $\sigma$ are most commonly measured in the plane of the substrate, reported power factors are typically in-plane values. The anisotropic nature of the power factor has been predicted in lightly doped PEDOT:Tos [12], where the values along the π–π stacking direction and along the chain were 31.5 and 2.09 $\mu W/m\ K^2$, respectively. Significant anisotropy in $S$ has been measured in stretched poly(aniline) and poly(acetylene). [38].

Compilations of oTE results indicate that most frequently $S^2\sigma < 100\ \mu W/m\ K^2$ [6, 11, 39]. For methods compatible with wearable devices, 0.45 $\mu W/m\ K^2$ is benchmark power factor for PEDOT applied to fabric [40].

For a numerous conjugated polymers including PEDOT, poly(thiophene), poly(acetylene), and PANI, along with their CNT composites, $S$ was found to broadly correlate with $\sigma^{-1/4}$ and, correspondingly, the power factor correlates with $\sigma^{1/2}$ [2, 37]. Data from small molecule organic conductors and the inorganic thermoelectric $Bi_2Te_3$ also fit this general correlation.

Because of the challenge of achieving air-stable n-type conjugated polymers, n-type oTEs have been less studied [2, 41]. However, n-type materials are essential for completing standard thermoelectric devices (Fig. 6.1). Loading of n-type inorganic thermoelectric materials into lightly p-type doped conjugated polymers or into dielectric polymers has been pursued for fabricating mechanically flexible hybrid organic/inorganic composite materials [5, 6, 23]. With tellurium nanorod fillers, a power factor of ~70 $\mu W/mK$ was reported [42].

### 6.2.3 Band theory

The migration of charge carriers in response to a temperature gradient is fundamentally related to both charge carrier scattering and changes in the occupation of the electronic density of states (DOS) (Section 1.2). The primary contribution of the Seebeck coefficient is the average entropy per charge carrier weighted by the contribution of the of the charge carrier to electrical conduction [2, 25]. Thus, from the perspective of band theory, where only energetic disorder has to be considered, $S$, can be calculated as

$$S = -\frac{k_B}{e}\int \frac{E - E_F}{k_B T}\frac{\sigma(E)}{\sigma}\mathrm{d}E \tag{6.11}$$

where the lead factor, $k_B/e$, is a value of 86.17 μV/K. The integral is dimensionless. Charge carriers occupying states with energies near $E_F$ provide the most significant contribution to the integral. The energy difference between the Fermi level, $E_F$, and the transport edge, $E_t$, are used in the definition of a dimensionless energy, $\alpha$, as

$$\alpha = \frac{E_F - E_t}{k_B T} \tag{6.12}$$

Combining eq. (6.11) with models for the electronic DOS (Chapter 3) leads to predictions of how thermoelectric performance varies with temperature and doping levels [24, 43–45]. For insulators, eq. (6.11) is often approximated as the **Heikes formula** [44]:

$$S \sim -\frac{k_B}{e}\alpha \tag{6.13}$$

#### 6.2.3.1 Low levels of doping

For very low doping levels in p-type conjugated polymers, the charge carriers are polarons existing in a very narrow band of energy levels [25, 46]. In this case, eq. (6.11) reduces to

$$S \sim -\frac{k_B}{e}\alpha \ln\left(\frac{2N}{n_c}\right) \tag{6.14}$$

where $N$ is DOS and $n_C$ is the density of charge carriers. Equation (6.14) explicitly predicts that $S$ will decrease linearly as the logarithmic carrier concentration increases.

Indeed, the correlation predicted by eq. (6.14) was experimentally observed for the semiconducting polymers IDT-BT and PBTTT (Fig. 4.3) [25]. However, the magnitude of the observed slopes were greater than predicted by eq. (6.6). This difference

was accounted for by assuming a fraction of the charged carriers were localized in trapping states. For PBTTT, at 300 K and $n_c = 10^{19}/cm^3$, $S \sim 700$ μV/K.

#### 6.2.3.2 High levels of doping

For conjugated polymers at higher doping levels, the Kang–Snyder (K–S) model relates $S$ to the carrier density [44]. The K–S model considers that charge carriers in states with $E_F < E < E_t$ are completely localized and do not contribute to electronic or thermal conduction. Recall that such trapping states were also invoked to explain the data at low levels of doping in IDT-BT (Section 6.2.3.1) Carriers in states with $E > E_t$ are assumed to undergo activated transport (i.e., hopping conduction). For a given value of $\alpha$, the non-normalized complete **Fermi–Dirac** integral of index $i$, $F_i(\alpha)$, is defined as

$$F_i(\alpha) = \int_0^\infty \frac{x^i}{1 + e^{x-a}} \mathrm{d}x \tag{6.15}$$

The value of $S$ predicted by the K–S model is given by

$$S = \frac{1}{\sigma}\left(\frac{k_B}{e}\right)\int\left(\frac{E - E_f}{k_B T}\right)\sigma_E\left(-\frac{\partial f}{\partial E}\right)\mathrm{d}E \tag{6.16}$$

The integer $s$ depends on the conjugated polymer system being evaluated. For poly (acetylene), P3HT, and PBTTT, $s = 3$ produced a good correspondence between the data and the model. It was proposed that $s = 3$ corresponds to thermal transport dominated by $\kappa_{electronic}$ (eq. (6.1)) in which the carriers responsible for both electrical and thermal transport are scattered by ionized impurities (dopants).

In contrast, using $s = 1$ corresponds to dominance by the $\kappa_{lattice}$ term of eq. (6.1), so that heat is transported though phonons (acoustic vibrations). For PEDOT, $s = 1$ resulted in good match to previously reported experimental measurements of $S$ and $\sigma$. This is consistent with the earlier discussion of the phonon glass nature of doped PEDOT in Section 6.1.1. The vibration modes in PEDOT responsible for thermal transport have been studied by **Green–Kubo** modal analysis [18].

### 6.2.4 Polymer morphology and tie chains

When adjacent crystallites are aligned (i.e., low-tilt-angle grain boundaries (Fig. 2.3a), quasi-1D transport paths for charge carriers and phonons proceed through alternating ordered and disordered regions (Fig. 6.2).

In conjugated polymers, the electronic and phononic states are coupled because a change in charge state leads to geometric reconfiguration of the polymer backbone. A particular conjugated polymer chain may extend through a number of crystalline regions [41, 47]. Spatial disorder along the chain may result in several

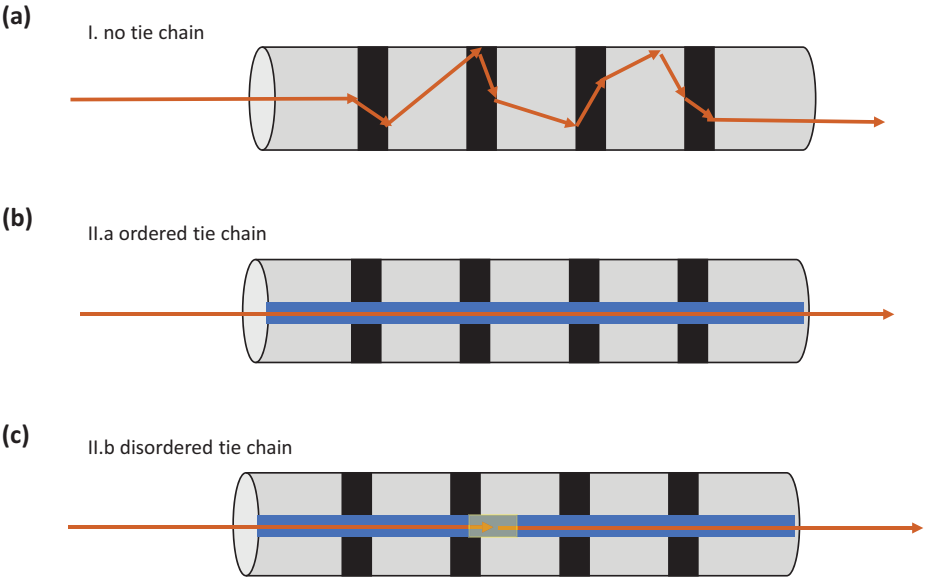


**Fig. 6.2:** Scenarios corresponding quasi-1D conduction, with I. no tie chains; IIa. tie chains with a fully conjugated backbone; and IIb. tie chains having backbone disorder.

regions of conjugation along the chain. In Section 3.6, tie chains were considered with respect to electronic transport. Here, the impact of tie chains on thermal transport is discussed. Figure 6.2 schematically shows three scenarios:

I. **Tie chains absent:** The crystallite size is large compare to the mean free path for transport. The molecular weight is low, so no tie chains are present. In this case, increasing crystallite size will enhance transport (Fig. 6.2a). Transport models should include 1D inhomogeneous spatial disorder [41, 48].
II. **Tie chains present:** The presence of tie chains results in mean free path exceeding the crystallite size. In this case, the crystallite size will have no effect on transport. Increasing molecular weight will increase the density and length of tie chains. The tie chains can either have:
   IIa. a single intrachain conjugation region extending down the entirety of the backbone (Fig. 6.2b), or
   IIb. several regions of intrachain conjugation along a single chain, due to the disorder in the backbone configuration.

The scenarios above can be evaluated against data reported for a systematically produced set of six highly conductive PEDOT films (Tab. 6.1) [35]. As grown by oxidative CVD (oCVD) from the monomer and the $FeCl_3$ oxidant, the films are highly doped and the counterion is $Cl^-$. Post-deposition acid rinsing in HBr exchanges the counterion to $Br^-$. With the exception of substrate temperature, identical processing

conditions were used. Table 6.1 shows that the five films grown at substrate temperatures between 190 and 300 °C have many similarities:

- the mean crystallite sizes determined from the Scherrer equation (eq. (2.2)) fall in the narrow range of 3.3 ± 0.3 nm;
- the crystallites have a preferential face-on orientation with respect the substrate;
- the film thicknesses are on the nanoscale, ≤36 nm thick, with three highest conductivity films 12 ± 2 nm thick; and
- Seebeck coefficients fall within a narrow range (11.2 ± 1.1 μV/K).

**Tab. 6.1:** PEDOT:Br properties resulting from systematic variation in growth temperature [35].

| Growth temperature (°C) | Texture | Film thickness (nm) | Mean crystal dimension (nm) | Electrical conductivity (in-plane) (S/cm) | Seebeck coefficient* (S/μV/K) | Power factor* (μW/mK$^2$) |
|---|---|---|---|---|---|---|
| 300 | Face-on | 10 | 3.2 | 6250 | 11.3 | 212.75 |
| 270 | Face-on | 14 | 3.0 | 4731 | 13.3 | 91.93 |
| 250 | Face-on | 11 | 3.1 | 3512 | 10.6 | 37.62 |
| 220 | Face-on | 31 | 3.6 | 1966 | 11.1 | 6.61 |
| 190 | Face-on | 36 | 3.0 | 955 | 10.0 | 0.75 |
| 150 | Edge-on | 34 | 5.4 | 371 | 11.4 | 0.04 |

The face-on preferential texture combined with the limited film thickness both favor quasi-1D transport. Despite the many similarities listed above, the electrical conductivity of the five films varies from 955 to 6250 S/cm. The corresponding increase in charge carrier mean free path estimated from eq. (3.21) is from ~2.6 to ~16 nm. This range corresponds to ~3 to ~21 monomer units along a chain or ~1 to ~5 nanocrystallites along the quasi-1D conduction path.

Having the mean free path of the charge carriers exceed the crystallite size is consistent with the presence of tie chains. The hypothesis of tie chains is also supported by the observation that crystallite size in not correlated with electrical conductivity (see scenario II). If tie chains are present, they have different effects for the transport of charge and heat, since the variation in $S$ is limited, while the change in $\sigma$ is dramatic. The measurement of molecular weight of insoluble polymers synthesized as ultrathin films and the direct detection of tie chains remain experimental challenges.

The various models used to predict correlations between $S$ and $\sigma$ consider only transport by the charge carriers in the π conjugated orbitals. However, Section 6.1 described that strong phonon transport proceeds along the sigma-bonded backbone. Thus, it is possible that intrachain phonon transport through sigma-bonding is less sensitive to defects in the backbone configuration than intrachain carrier transport through pi-bonding. For this hypothesis, the full length of the chain would remain

effective for phonon transport by the sigma bonds, while the electronic behavior would be correlated with shorter regions of conjugation along the chain (scenario II.b, Fig. 6.2c). Higher conductivity would result from decreasing disorder along the chain.

Table 6.1 contains data for one edge-on preferential oriented PEDOT film, having a thickness and Seebeck coefficient in the same range as the face-on oriented films, consistent with similar thermal transport. The lower electrical conductivity corresponds to a shorter mean free path for the charge carriers of ~1 nm, which is less than the crystallite size. The increased disorder along is hypothesized to correlate with a higher probability of having high-tilt angle grain boundary (Fig. 2.3) in the edge-on orientation. The power factor is also shown in Tab. 6.1. Face-on texture with high interchain charge carrier mobility results in the highest value of 212 $W/mK^2$.

## References

[1] Heydari Gharahcheshmeh M, Gleason KK. Device fabrication based on oxidative chemical vapor deposition (oCVD) synthesis of conducting polymers and related conjugated organic materials. Adv Mater Interfaces 2019, 6, 1801564.
[2] Russ B, Glaudell A, Urban JJ, Chabinyc ML, Segalman RA. Organic thermoelectric materials for energy harvesting and temperature control. Nat Rev Mater 2016, 1, 16050.
[3] Bubnova O, Khan ZU, Wang H, et al. Semi-metallic polymers. Nat Mater 2014, 13, 190–194.
[4] Petsagkourakis I, Kim N, Tybrandt K, Zozoulenko I, Crispin X. Poly(3,4-ethylenedioxythiophene): Chemical synthesis, transport properties, and thermoelectric devices. Adv Electron Mater 2019, 5, 1800918.
[5] Bahk JH, Fang H, Yazawa K, Shakouri A. Flexible thermoelectric materials and device optimization for wearable energy harvesting. J Mater Chem C 2015, 3, 10362–10374.
[6] Yue R, Xu J. Poly(3,4-ethylenedioxythiophene) as promising organic thermoelectric materials: A mini-review. Synth Met 2012, 162, 912–917.
[7] Wang Y, Meng H-M, Song G, Li Z, Zhang X-B. Conjugated-polymer-based nanomaterials for photothermal therapy. ACS Appl Polym Mater 2020, 2, 4258–4272.
[8] Wang Y, Zhang H, Wang Z, Feng L. Photothermal conjugated polymers and their biological applications in imaging and therapy. ACS Appl Polym Mater 2020, 2, 4222–4240.
[9] Matula RA. Electrical resistivity of copper, gold, palladium, and silver. J Phys Chem Ref Data 1979, 8, 1147–1298.
[10] Pawel RW, Ho CY, Liley PE. Thermal conductivity of selected metals. National Standard Reference Data System (NSRDS). US Department of Commerce, 1966.
[11] Kroon R, Mengistie DA, Kiefer D, et al. Thermoelectric plastics: From design to synthesis, processing and structure-property relationships. Chem Soc Rev 2016, 45, 6147–6164.
[12] Shi W, Zhao T, Xi J, Wang D, Shuai Z. Unravelling doping effects on PEDOT at the molecular level: From geometry to thermoelectric transport properties. J Am Chem Soc 2015, 137, 12929–12938.
[13] Weathers A, Khan ZU, Brooke R, et al. Significant electronic thermal transport in the conducting polymer poly(3,4-ethylenedioxythiophene). Adv Mater 2015, 27, 2101–2106.
[14] Xu Y, Wang X, Zhou J, et al. Molecular engineered conjugated polymer with high thermal conductivity. Sci Adv 2018, 4, eaar3031.

[15] Zhang T, Wu X, Luo T. Polymer nanofibers with outstanding thermal conductivity and thermal stability: Fundamental linkage between molecular characteristics and macroscopic thermal properties. J Phys Chem C 2014, 118, 21148–21159.
[16] Grundler M, Derieth T, Heinzel A. Polymer compounds with high thermal conductivity. AIP Conf Proc 2016, 1779, 030015.
[17] Lee YJ, Jeng KS, Chen JT, Sun KW. Exceptionally low thermal conductivity of poly(3-hexylthiophene) single nanowires. RSC Adv 2015, 5, 90847–90851.
[18] Cappai A, Antidormi A, Bosin A, Narducci D, Colombo L, Melis C. Impact of synthetic conditions on the anisotropic thermal conductivity of poly(3,4-ethylenedioxythiophene) (PEDOT): A molecular dynamics investigation. Phys Rev Mater 2020, 4, 035401.
[19] Smith PM, Su L, Gong W, Nakamura N, Reeja-Jayan B, Shen S. Thermal conductivity of poly (3,4-ethylenedioxythiophene) films engineered by oxidative chemical vapor deposition (oCVD). RSC Adv 2018, 8, 19348–19352.
[20] Shen S, Henry A, Tong J, Zheng R, Chen G. Polyethylene nanofibres with very high thermal conductivities. Nat Nanotechnol 2010, 5, 251–255.
[21] Kivelson S, Heeger AJ. Intrinsic conductivity of conducting polymers. Synth Met 1988, 22, 371–384.
[22] Wei Q, Mukaida M, Kirihara K, Ishida T. Experimental studies on the anisotropic thermoelectric properties of conducting polymer films. ACS Macro Lett 2014, 3, 948–952.
[23] Du Y, Shen SZ, Cai K, Casey PS. Research progress on polymer-inorganic thermoelectric nanocomposite materials. Prog Polym Sci 2012, 37, 820–841.
[24] Selvaggi JP. Modeling the Seebeck coefficient for organic materials with the Kubo–Greenwood integral and a Gaussian density of states. J Comput Electron 2019, 18, 473–481.
[25] Venkateshvaran D, Nikolka M, Sadhanala A, et al. Approaching disorder-free transport in high-mobility conjugated polymers. Nature 2014, 515, 384–388.
[26] Bubnova O, Berggren M, Crispin X. Tuning the thermoelectric properties of conducting polymers in an electrochemical transistor. J Am Chem Soc 2012, 134, 16456–16459.
[27] Chen H, Li C. PEDOT: Fundamentals and its nanocomposites for energy storage. Chinese J Polym Sci 2020, 38, 435–448.
[28] Reynolds JR, Thompson BC, Skotheim TA, et al. Electric transport properties in PEDOT thin films. In: Conjugated Polymers. 2019, 45–128.
[29] Poudel B, Hao Q, Ma Y, et al. High-thermoelectric performance of nanostructured bismuth antimony telluride bulk alloys. Science (80-) 2008, 320, 634–638.
[30] Cho C, Song Y, Hsu JH, Yu C, Stevens DL, Grunlan JC. Organic thermoelectric thin films with large p-type and n-type power factor. J Mater Sci 2021, 56, 4291–4304.
[31] Nogami Y, Kaneko H, Ishiguro T, Takahashi A, Tsukamoto J, Hosoito N. On the metallic states in highly conducting iodine-doped polyacetylene. Solid State Commun 1990, 76, 583–586.
[32] Hinckley AC, Andrews SC, Dunham MT, et al. Achieving high thermoelectric performance and metallic transport in solvent-sheared PEDOT:PSS. Adv Electron Mater 2021, 2001190.
[33] Kim GH, Shao L, Zhang K, Pipe KP. Engineered doping of organic semiconductors for enhanced thermoelectric efficiency. Nat Mater 2013, 12, 719–723.
[34] Bubnova O, Khan ZU, Malti A, et al. Optimization of the thermoelectric figure of merit in the conducting polymer poly(3,4-ethylenedioxythiophene). Nat Mater 2011, 10, 429–433.
[35] Wang X, Zhang X, Sun L, et al. High electrical conductivity and carrier mobility in oCVD PEDOT thin films by engineered crystallization and acid treatment. Sci Adv 2018, 4, 1–10.
[36] Zhang B, Sun J, Katz HE, Fang F, Opila RL. Promising thermoelectric properties of commercial PEDOT:PSS materials and their Bi2Te3 powder composites. ACS Appl Mater Interfaces 2010, 2, 3170–3178.

[37] Patel SN, Glaudell AM, Peterson KA, et al. Morphology controls the thermoelectric power factor of a doped semiconducting polymer. Sci Adv 2017, 3, e1700434.
[38] Mateeva N, Niculescu H, Schlenoff J, Testardi LR. Correlation of Seebeck coefficient and electric conductivity in polyaniline and polypyrrole. J Appl Phys 1998, 83, 3111–3117.
[39] Dong J, Portale G. Role of the processing solvent on the electrical conductivity of PEDOT:PSS. Adv Mater Interfaces 2020, 7.
[40] Zhang X, Li TT, Ren HT, et al. Flexible and wearable wristband for harvesting human body heat based on coral-like PEDOT:Tos-coated nanofibrous film. Smart Mater Struct 2021, 30, 015003.
[41] Heydari Gharahcheshmeh M, Gleason KK. Texture and nanostructural engineering of conjugated conducting and semiconducting polymers. Mater Today Adv 2020, 8, 100086.
[42] See KC, Feser JP, Chen CE, Majumdar A, Urban JJ, Segalman RA. Water-processable polymer-nanocrystal hybrids for thermoelectrics. Nano Lett 2010, 10, 4664–4667.
[43] Mendels D, Tessler N. Thermoelectricity in disordered organic semiconductors under the premise of the gaussian disorder model and its variants. J Phys Chem Lett 2014, 5, 3247–3253.
[44] Kang SD. Charge-transport model for conducting polymers. Nat Mater 2017, 16.
[45] Abutaha A, Kumar P, Yildirim E, et al. Correlating charge and thermoelectric transport to paracrystallinity in conducting polymers. Nat Commun 2020, 11, 1–8.
[46] Shi W, Chen J, Xi J, Wang D, Shuai Z. Search for organic thermoelectric materials with high mobility : The derivatives. Chem Mater 2014, 26, 2669–2677.
[47] Phillips PJ. Polymer crystals. Rep Prog Phys 1990, 53, 549–604.
[48] Kaiser AB. Electronic transport properties of conducting polymers and carbon nanotubes. Rep Prog Phys 2001, 64, 1–49.

# 7 Conclusions and future directions

The interplay between scientific understanding and technological targets has driven remarkable achievements in improving the electronic, optical, electrochemical, and thermal properties of conjugated polymers. Additionally, the chemical reactivity, biocompatibility, magnetic properties, and mechanical properties of conjugated polymers are attractive for numerous applications. Several selected interdisciplinary applications will be overviewed in the first section of chapter.

For real-world impact, the conjugated polymer of interest must be stable, cost-effective, scale-up to large areas, and have minimal environmental, health, and safety (EHS) concerns. Methods are needed which produce films economically over large areas. These methods must also achieve the desired nanostructure in micro-scale layers. Some of these challenges will be addressed in the second section of this chapter.

Continued progress is expected with advances in methodologies for synthesis, processing, and characterization. With ever-accelerating computational power, the ability to directly compare theory and experiments is increasing possible. This comparison provides feedback to the computation on the validity of modeling assumptions. Conversely, computation, such as density functional theory (DFT), is challenging long-standing classical hypothesize, such as optical spectra assignments. Often faster progress is made by adopting methods from allied fields. Two such opportunities are discussed in the third and final section of this chapter.

## 7.1 Technological drivers

The physical and chemical properties were highlighted in the preceding chapters. Extremely selective examples and application areas were used to illustrate these concepts. This section provides a high-level technological overviews for several of the many potential application area for conjugated polymers. The selection was made to illustrate increasing need for interdisciplinary approaches.

### 7.1.1 Electrocatalysis

Conjugated polymers have the potential to accelerate the rate of electron transfer at surfaces, thus acting as electrocatalysts [1]. Faster electrochemical reactions underlie multiple technologies desired for sustainable energy. To mitigate climate change, the reduction of carbon dioxide is of particular interest, as is the reduction of oxygen for fuel cell and metal–air battery applications [2]. Redox reactions are also used in flow batteries desired for grid-scale energy storage [3]. For accelerating redox reactions,

https://doi.org/10.1515/9781501524615-007

conjugated polymers represent a metal-free alternative to expensive electrocatalytic metals, such as platinum. Care must be taken to confirm that any metal used in the conjugated polymer synthesis is not responsible for the electrocatalytic activity [4].

The oxygen reduction reaction (ORR) mechanisms using poly(3,4-ethylenedioxythiophene (PEDOT) as the electrocatalyst have been analyzed experimentally [2, 5] and computationally [4]. These studies considered both a four-electron process, producing two water molecules, and a two-electron process, producing hydrogen peroxide as the product. A mixture of the two pathways is consistent with the experimental results obtained using a rotating disk electrode. The experiments also revealed a correlation between electroactivity and electrical conductivity. DFT calculations suggest the catalytic behavior of PEDOT for ORR is influenced by acidity and that dopants are not essential.

Electrocatalysis at the surface of conjugated polymeric electrodes can be an environmentally friendly pathway for organic synthesis [1]. Other redox-mediating agents have been successfully combined into the matrix of conjugated polymers. For example, both biomolecules and inorganic catalysts have been immobilized inside interchain cavities.

### 7.1.2 Spintronics

Spintronic devices transmit, process, and store information through changes in the quantized angular momentum of the charge carriers [6]. Spin is being exploited for quantum computing. A pure spin current can exist even when there is no net flow of charge. Interest in organics for spintronic devices results from the slow spin-lattice relaxation process in materials composed of light atoms, such as carbon. Spin diffusion lengths of ~1000 nm have been reported in organic materials.

Spintronic devices include spin valves, spin organic light-emitting diodes, and spin photovoltaics [7]. Organic spin values have been fabricated using a conjugated polymer spacer between two ferromagnetic electrodes. Spin can be transported between the electrodes through the spacer. Each electrode can be polarized by independent magnetic fields, producing a magnetoresistance (MR) effect. Higher MR responses result from higher spin diffusion lengths in the spacer and smaller inter-electrode spacings. In addition to spin transport in the polymer, and spin injection is also essential for spintronic devices. The injection efficiency of the spin from the electrode to the spacer depends on matching the Fermi energy of the two materials. For example, the lowest unoccupied molecular orbital (LUMO) of n-type conjugated polymers has been matched to the ferromagnetic materials, $La_{2/3}Sr_{1/2}MnO_3$ and Co.

### 7.1.3 Bioelectronics and biosensing

Bioelectronic devices provide an interface to living tissue to monitor, amplify, and stimulate electrochemical responses [8, 9]. Established biomedical uses for implantable electrodes include pacemakers, cochlear implants, and deep-brain stimulation. Bioelectronic devices are also desired to gain fundamental insight into physiological functions. In living tissues, currents are primarily a result of ionic transport. Ion-selective channels in the cell membranes control the local ionic concentrations. Redox reactions enable biochemical processes such as photosynthesis and cellular metabolism. Thus, for bioelectronics, electrodes exhibiting mixed ionic and electronic conductivity (MIEC, Chapter 5) are highly desirable. Indeed, the MIEC electrodes for neural recording in the brain have been fabricated using PEDOT.

Biosensing is enabled by incorporating molecular recognition elements, such as antibodies, enzymes, or DNA/RNA, into the matrix or onto the surface of conjugated polymers [9]. The resulting biosensors enable monitoring of multiple aspects of animal and human physiology. Motivated by agricultural needs, the physiology of actively growing plants, was followed using poly(3,4-propylenedioxythiophene) (PProDOT), where conformal coverage over the mesostructured plant leaves produced high surface area electrodes. Functionalized conjugated polymers have also been proposed as low-cost chemoresistive sensors for rapid monitoring of food safety [10].

### 7.1.4 Photothermal therapy

Biocompatible conjugated polymers are desirable as candidates for photothermal agents [11]. Such agents can selective accumulate in tissues which have been damaged by cancer, bacterial infection, or neurodegenative disease. Laser exposure selectively excites the photothermal agent. Nonradiative relaxation of the photoexcited state releases heat, causing the ablation of the surrounding cells, a process known as photothermal therapy (PTT). Alternatively, the photoacoustic signal associated with the heat release can be used to image vessels, tissues, and tumors. Photothermal conjugated polymers are also of interest as nanocarriers for the targeted delivery of therapeutics and bioimaging contrast agents. For in vivo and clinical applications, photothermal agents must noncytotoxic, avoiding the release of undesirable species, such as metal ions.

Without added photothermal agents, biological tissue is highly transparent to near-infrared (NIR) light, allowing for deep tissue penetration [11]. The laser wavelength is typically at 808, 980, or 1064 nm, which falls either the NIR-I (700–1000 nm) or the NIR-II (1000–1700) spectral regions. The NIR-II exposure achieves deeper penetration into tissues and is less effected autofluorescence background signals. Poly(aniline), poly(pyrrole), poly(thiophene), and poly(dopamine) have all been demonstrated for PTT. However, increased focus has centered on the custom synthesis of donor–acceptor (D–A) conjugated polymers (Section 4.5) for precise

control of the optical bandgap in the NIR-I and NIR-II spectral regions. For example, using the donor bithiophene and the acceptor bis(5-oxothienol[3,2-b]pyrolle-6-ylidene) benzodifurandione resulted in strong NIR-II absorption at ~1,107 nm. The D–A polymers also have photothermal conversion efficiencies, because they tend to quench fluorescence, thus increasing the fraction of photoexcited states which relax through vibrations, corresponding to increased release of heat.

For injection into the body, the D–A polymers must be fabricated into hydrophilic nanoparticles [11]. One successful strategy is the synthesis of block copolymers, where one block is the hydrophobic conjugated polymer and the other block is biocompatible hydrophilic polymer, such as poly(ethylene glycol). Injection of these types of particles has been demonstrated for the imaging of brain vascular and tumor volume in mice.

## 7.2 Stability and scalability

While discovering the remarkable properties of poly(acetylene) sparked the creation of an entirely new field, the focus has shifted to more air-stable materials. Stability is essential for most applications. Realizing most technological goals requires the ability to withstand environmental stresses, including oxygen, UV irradiation, and humidity. These stresses can directly impact the covalent chemical bonds and conformation of the polymer chains and their complexation to the counterion. Stability is also required to enable conjugated polymers to be integrated into multilevel stacks for devices (see, e.g., Fig. 4.4). The deposition and patterning of each layer in the devices require a specific temperature for a given time and exposure to various chemical reactants, either as gas-phase or solution-phase species. Device integration requires that the conjugated polymer be stable against the conditions used in all successive fabrication steps. The chemical design of the polymer backbone and solid–solid interfaces are two potential means of increasing stability of conjugated polymer layers.

Large-area applications require processing methods that scale from the lab-bench prototypes to industrial dimensions of a meter or more. An important consideration is the overall EHS of the process [12]. This criterion motivates the desire to minimize overall materials usage and to utilize nontoxic, environmentally green reagents. Systematic control and process reproducibility are also need for commercialization.

Economic viability places constraints on the number and types of synthetic and post-growth processing steps that can be used. While at the bench scale, solution-based processes are generally cheaper than vacuum processes, this is not necessarily the case at the industrial scale. The cost for automation and control systems often dwarfs that of the core process. In the semiconductor industry, automated spin coaters with atmospheric control cost as much or more than chemical vapor deposition systems. Industrial furnaces for device annealing are also expensive. An interesting analogy is low dielectric constant materials (low k) to replace silicon

dioxide interconnection layers in semiconductor circuits [13]. Motivated by lower cost of ownership, a multitude of spin-on polymeric candidates were proposed to replace CVD silicon dioxide. However, the cost saving was not realized because the specialty polymers were expensive, and both an industrial-scale spin coater and a furnace were required. For CVD, only simple molecular precursor and one piece of equipment was need. Additional, the CVD materials outperformed the spin-on materials. As a result, CVD $SiO_2$ was replaced by CVD Si:O:C:H. Roll-to-roll processing further lowers the cost of vacuum processing. Indeed, the metal barrier coating on the inside of many food packages, such as potato chip bags, is applied by vacuum deposition.

### 7.2.1 Backbone architecture

The polymers discussed in earlier chapters, monomers are connected by one covalent bond to create 1D polymers. Carbon-based polymers can also have monomers linked to one another through two or more bonds, leading to ladder- and spiro-type architectures and multistrand polymers [14]. These new structural topologies result in the entire backbone consisting of fused rings that are conjugated. Examples include poly(acenes), poly(phenanthrene) and graphene nanoribbons. These chemical motifs have the potential to improve physical properties including stability, but are likely to require new synthesis strategies.

A ladder polymer is displayed in Fig. 7.1 [15]. Along the backbone are bisanthrene units comprised of eight fused six-membered rings. In between each pair of bisanthrene is a pentalene bridge, consisting of two fused five-member rings. The polymeric structure was confirmed by noncontact atomic force microscopy. This high-resolution micrograph was obtained on the same gold (111) surface used to synthesize the discrete conjugated polymer chain. Scanning tunneling spectra established the valence band edge at −0.6 eV and the conduction band edge at 0.5 eV and provided spatial maps at these two energies. DFT calculations confirmed both the chemical bonding structure and spatial maps of the electronic states at the VB and CB edges. The DFT was also used to obtain the electronic structure in momentum space and overall density of states as function of energy, which qualitatively agreed with experiment.

### 7.2.2 n-Type conjugated polymers

For many devices, n-type materials are essential. For example, pairs of p-type and n-type legs are utilized for thermoelectric devices (Chapter 6). Additionally, acceptors are required for photovoltaics (Section 4.5). Most commonly, fullerene acceptors have been paired with p-type conjugated polymer as donors. However, to fabricate

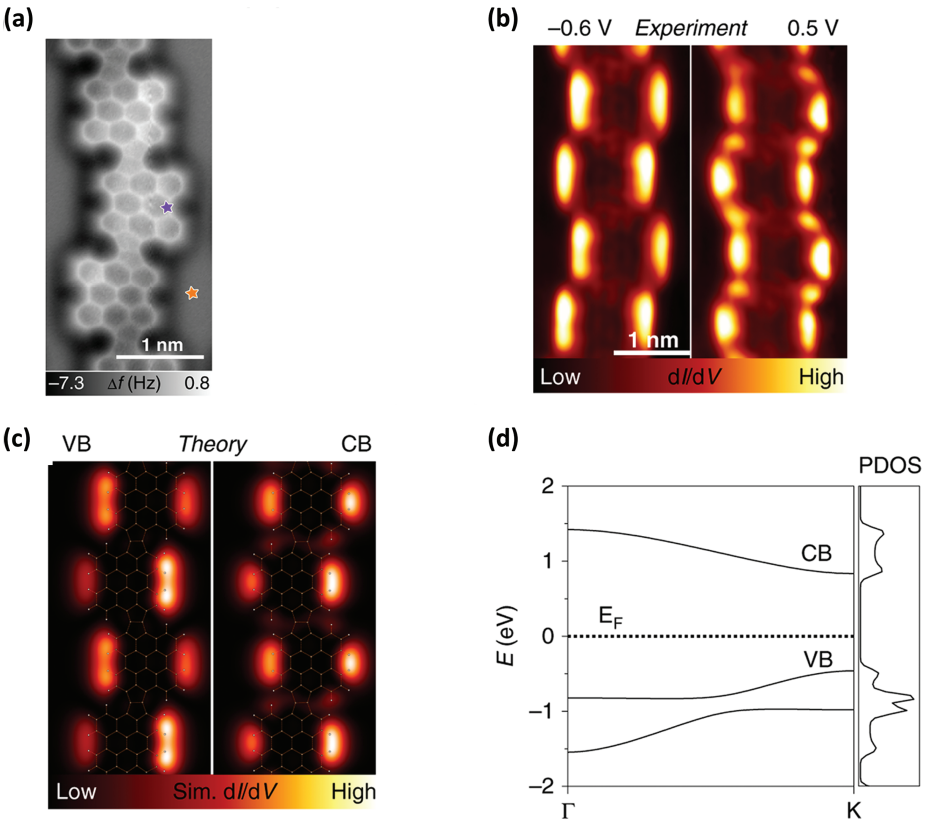


**Fig. 7.1:** For the ladder conjugated bisanthene polymer with pentylene bridges: (a) high-resolution noncontact atomic force micrograph of a single chain, spatial maps of the electronic states at the valence band (−0.6 eV) and conduction band (0.5 eV) edge energies by (b) experiment and (c) theory, (d) calculate electronic structure. (a–d) Reprinted with permission from de la Torre B et al. Nat. Commun.11, 4567 (2020) copywrite 2020 Springer.

all-polymer solar cells, the fullerene is replaced by an n-type conjugated polymer [12]. The design and fabrication of organic energy storage, field-effect transistors, electrochemical transistors, and spintronic devices could also benefit from n-type conjugated polymers [7].

The study and performance of n-type conjugated polymers have lagged that of their p-type counterparts [7]. Air-stable p-type conjugated polymers have highest occupied molecular orbital levels that fall below −4.8 eV, the energy of the trap states resulting from redox reactions with water and oxygen. For air-stable n-type conjugated polymers, the LUMO level must lie below −4.0 eV. Lowering the LUMO level also increases the efficiency of n-type doping. A LUMO level of −4.2 eV was achieved using benzodifurandione-based oligo(*p*-phenylenevinylene) (BDOPV) as a building block. The monomer naphthalene diimide (NDI) is commonly used in synthesizing

n-type conjugated polymers for thermoelectric applications. With n-type molecular doping, the polymerized NDI reached an electronic conductivity, $\sigma$, of ~0.01 S/cm and a power factor of 0.6 μW/mK. These values are far below those p-type conjugated polymers (Table 6.1). A derivative of NDI, benzoimidazobenzophenanthrolines (BBL) is a monomer for synthesizing ladder-type polymers. The ladder architecture reduces backbone torsion, lowering the reorganization energy associated with changes in electronic state (Section 4.5). Upon n-type doping with tetrakis(dimethylamino)ethylene, the BBL-based ladder polymer reached $\sigma = 0.42$ S/cm. The BBL-based polymer has been utilized for both thermoelectrics and organic electrochemical transistors [7], and its n-type charge transport of BBL-based polymer has been modeled by DFT [16].

### 7.2.3 Porous networks

Conjugated 2D and 3D porous networks have been synthesized using multiple methods and a multitude of rigid building blocks [17, 18]. The earliest reports utilized aromatic ring structures interconnected by multiple alkyne struts (-C≡C-). Building blocks with three or more interconnections represent crosslinking sites that can improve stability.

The void structures in porous materials reduce the resistance to mass transport. Thus, porous materials are frequently utilized in applications requiring molecular diffusion. Applications of porous conjugated polymers include adsorption, separation, sensing, and catalysis [17]. Hierarchical pore structures may also facilitate the access of ionic species to redox-active sites, as desired for electrochemical energy storage (Section 5.5). The porosity may help accommodate the mechanical stresses due to density changes upon doping and dedoping. In many cases, the 3D conjugated polymeric networks exhibit high surface area (>1000 $m^2/g$). This high surface area is achieved without requiring the heavy metal atoms utilized in molecular organic framework materials. A favorable factor for large-area applications is that the synthesis of conjugated polymers requires only earth-abundant elements, such as hydrogen, carbon, oxygen, nitrogen, and sulfur.

The optoelectronic properties of porous conjugated polymers are of particular interest for metal-free photocatalysis [18]. Of particular interest is using solar light to induce $H_2$ evolution from water as a clean and renewable energy source. Conjugated polymers with bandgaps between 1.8 and 2.2 eV are desired to achieve good light utilization for photocatalytic water splitting. Porosity increases the density of surface-active catalytic sites.

### 7.2.4 Grafting

Preventing delamination is essential for building up the multilayer stacks of materials utilized in device structures. Avoiding delamination is also critical for achieving successful subtractive lithographic pattering of conjugated polymers. By forming covalent chemical bonds between the substrate and the polymer layer, delamination can be avoided. A variety of methods have been used to achieve interfacial grafting of conjugated polymers [19, 20]. Grafting can also be utilized to orient the polymer backbone perpendicular to the substrate. The backbone orientation will effect charge injection and extraction to the underlying layer.

## 7.3 Opportunities in characterization and computation

### 7.3.1 Tie chains

Tie chains interconnecting crystallites have been proposed to explain high charge carrier and phonon mobilities in semicrystalline conjugated polymers (Chapters 3 and 6). Tie chains exist at the mesoscale, which is challenging for both experimental and computational evaluation. Various specialized experiments have provided insight into tie chains [21]. These experiments support the hypothesis that a critical tie chain fraction can represent a percolation limit for enhanced charge carrier mobility. However, tie chain fractions are not yet routinely measured. The development of such a routine measurement would provide valuable guidance to the designers of molecular structures and processing methods. For example, the relationship between the fraction of conductive tie chains and the texture of the crystallites could be directly explored.

Higher molecular weights will likely increase the occurrence of tie chains [21]. It is important to consider that two polymeric samples can have the same mean molecular weight but differ in their polydispersity index (PDI). The longest chains with be found in the high molecular weight tail of the materials with the larger PDI. These long chains would have a high probability of being tie chains. Conformation also is also essential to forming tie chains that are pathways for high intercrystallite conductivity. However, the traditional means of evaluating a molecular weight distribution, gel permeation chromatography (GPC), can be difficult to apply to conjugated polymers. The GPC method is not compatible with insoluble conjugated polymer and typically requires more material than is present in ultrathin films.

Tie chains have long been considered to impact the mechanical properties of macromolecular solids [21]. For example, the **Huang–Brown** model assumes any chain longer than the intercrystal distance forms a tie chain. Thus, it is interesting that experimental methods to measure the mechanical properties of other types of polymer thin films are increasingly being applied to conjugated polymers [22]. Besides

providing valuable data for developing flexible devices, the mechanical measurements may provide insight into the fraction of tie chains present.

The glass transition temperature, $T_{g,}$ is a property related to the mechanical behavior and chain mobility of amorphous polymers or the amorphous region of semicrystalline polymers. Plastic, rubbery mechanical behavior occurs for when $T_g$ is below the ambient temperature. Conversely, when $T_g$ is higher than the ambient temperature, the polymer behaves as a rigid glass. For semicrystalline conjugated polymers, the utility of measuring and predicting $T_g$ and understanding its relationship to other properties has been less commonly considered [23]. Additionally, synthesizing polymers above their $T_g$ allows an equilibrium morphology to develop, rather than resulting in a kinetically trapped state. Indeed, marked differences in preferential orientation of PEDOT have been observed at growth temperatures above and below its $T_g$ of ~102 °C [24–26]. Increase chain mobility during synthesis will also promote the formation of higher molecular weight polymers, thus increasing the probability of forming tie chains.

### 7.3.2 Order and orientation

The electrical, optical, electrochemical, and thermal properties of conjugated polymers all depend on spatial and energetic disorder. To further advance the understanding of structure–property relationships, routine measurements of disorder, such as the Urbach edge (Section 4.4), and new methods for determine the intrinsic shapes of energy bands (Sections 5.4 and 7.1.4) should be undertaken on series of films displaying systematic variations. The measured metrics of disorder can be used to rigorously test predictions of increasing powerful computational studies. For this comparison, computed metrics of disorder, such as paracrystallinity (Section 2.2), must be related to experimentally determined quantities.

For films of nanoscale thickness and in nanostructure, interfacial effects have yet to be fully explored (Section 2.5.2). The physical dimensions of the material can constrain the orientation of nanocrystals having comparable dimensions. Physical constraints will impact the pairwise orientation distribution function of nearest neighbor nanocrystals and hence the probability of these ordered regions being interconnected by linear conjugated tie chains. For ultrathin polymer films, the interfacial energies with the substrate and at the top interface can influence the equilibrium orientation of the lamella, as has been observed using block copolymers in directed self-assembly nanopatterning processes. Exploiting the supermolecular assembly of conjugated polymers for creating order and orientation (Section 4.3) is an alternative paradigm to thin film fabrication.

## 7.4 Concluding remarks

Conjugated polymers have a rich history based on interdisciplinary research, yet exciting challenges remain for understanding these materials and realizing their full technological impact. A key to unlocking the full potential of semicrystalline conjugating polymers is controlling and exploiting their nanoscale order and orientation.

## References

[1] Ibanez JG, Rincón ME, Gutierrez-Granados S, Chahma M, Jaramillo-Quintero OA, Frontana-Uribe BA. Conducting polymers in the fields of energy, environmental remediation, and chemical-chiral sensors. Chem Rev 2018, 118, 4731–4816.
[2] Kaviani S, Mohammadi Ghaleni M, Tavakoli E, Nejati S. Electroactive and conformal coatings of oxidative chemical vapor deposition polymers for oxygen electroreduction. ACS Appl Polym Mater 2019, 1, 552–560.
[3] Heydari Gharahcheshmeh M, Wan CTC, Ashraf Gandomi Y, et al. Ultrathin conformal oCVD PEDOT coatings on carbon electrodes enable improved performance of redox flow batteries. Adv Mater Interfaces 2020, 7, 2000855.
[4] Singh SK, Crispin X, Zozoulenko IV. Oxygen reduction reaction in conducting polymer PEDOT: Density functional theory study. J Phys Chem C 2017, 121, 12270–12277.
[5] Winther-Jensen B, Winther-Jensen O, Forsyth M, MacFarlane D. High rates of oxygen reduction. Science (80-) 2008, 321, 671–674.
[6] Schott S, Chopra U, Lemaur V, et al. Polaron spin dynamics in high-mobility polymeric semiconductors. Nat Phys 2019, 15, 814–822.
[7] Jia H, Lei T. Emerging research directions for n-type conjugated polymers. J Mater Chem C 2019, 7, 12809–12821.
[8] Cea C, Spyropoulos GD, Jastrzebska-Perfect P, Ferrero JJ, Gelinas JN, Khodagholy D. Enhancement-mode ion-based transistor as a comprehensive interface and real-time processing unit for in vivo electrophysiology. Nat Mater 2020, 19, 679–686.
[9] Zeglio E, Rutz AL, Winkler TE, Malliaras GG, Herland A. Conjugated polymers for assessing and controlling biological functions. Adv Mater 2019, 31, 1806712.
[10] Bhattacharyya D, Senecal K, Marek P, Senecal A, Gleason KK. High surface area flexible chemiresistive biosensor by oxidative chemical vapor deposition. Adv Funct Mater 2011, 21.
[11] Wang Y, Zhang H, Wang Z, Feng L. Photothermal conjugated polymers and their biological applications in imaging and therapy. ACS Appl Polym Mater 2020, 2, 4222–4240.
[12] Lee C, Lee S, Kim G-U, Lee W, Kim JK. Recent advances, design guidelines, and prospects for all-polymer solar cells. Chem Rev 2019, 119, 8028–8086.
[13] Volksen W, Miller RD, Dubois G. Low dielectric constant materials. Chem Rev 2010, 110, 56–110.
[14] Sánchez-Grande A, Urgel JI, Cahlík A, et al. Diradical organic one-dimensional polymers synthesized on a metallic surface. Angew Chemie – Int Ed 2020, 59, 17594–17599.
[15] De La Torre B, Matěj A, Sánchez-Grande A, et al. Tailoring π-conjugation and vibrational modes to steer on-surface synthesis of pentalene-bridged ladder polymers. Nat Commun 2020, 11, 4567.

[16] Ghosh S, Gueskine V, Berggren M, Zozoulenko I V. Electronic structures and optical absorption of N-type conducting polymers at different doping levels. J Phys Chem C 2019, 123, 15467–15476.
[17] Lee JSM, Cooper AI. Advances in conjugated microporous polymers. Chem Rev 2020, 120, 2171–2214.
[18] Zhao C, Chen Z, Shi R, Yang X, Zhang T. Recent advances in conjugated polymers for visible-light-driven water splitting. Adv Mater 2020, 32, 1907296.
[19] Bousquet A, Awada H, Hiorns RC, Dagron-Lartigau C, Billon L. Conjugated-polymer grafting on inorganic and organic substrates: A new trend in organic electronic materials. Prog Polym Sci 2014, 39, 1847–1877.
[20] Ugur A, Katmis F, Li M, et al. Low-dimensional conduction mechanisms in highly conductive and transparent conjugated polymers. Adv Mater 2015, 27, 4604–4610.
[21] Gu K, Loo YL. The polymer physics of multiscale charge transport in conjugated systems. J Polym Sci Part B Polym Phys 2019, 57, 1559–1571.
[22] Root SE, Savagatrup S, Prinz AD, Rodriquez D, Lipomi DJ. Mechanical properties of organic semiconductors for stretchable, highly flexible, and mechanical robust electronics. Chem Rev 2017, 117, 6467–6499.
[23] Xiao M, Sadhanala A, Abdi-Jalebi M, et al. Linking glass-transition behavior to photophysical and charge transport properties of high-mobility conjugated polymers. Adv Funct Mater 2020, 2007359, 7, 2007359.
[24] Moni P, Lau J, Mohr AC, et al. Growth temperature and electrochemical performance in vapor-deposited poly(3,4-ethylenedioxythiophene) thin films for high-rate electrochemical energy storage. ACS Appl Energy Mater 2018, 1, 7093–7105.
[25] Wang X, Zhang X, Sun L, et al. High electrical conductivity and carrier mobility in oCVD PEDOT thin films by engineered crystallization and acid treatment. Sci Adv 2018, 4, eaat5780.
[26] Heydari Gharahcheshmeh M, Tavakoli MM, Gleason EF, Robinson MT, Kong J, Gleason KK. Tuning, optimization, and perovskite solar cell device integration of ultrathin poly(3,4-ethylene dioxythiophene) films via a single-step all-dry process. Sci Adv 2019, 5, eaay0414.

# Index



https://doi.org/10.1515/9781501524615-008